Investigation of Methods for Data Communication and Power Delivery Through Metals

David J. Graham

School of Electrical, Electronic and Computer Engineering

Newcastle University

A thesis submitted for the degree of

Doctor of Philosophy

September 2011

Abstract

The retrieval of data from a sensor, enclosed by a metallic structure, such as a naval vessel, pipeline or nuclear flask is often very challenging. To maintain structural integrity it is not desirable to penetrate the wall of the structure, preventing any hard-wired solution. Furthermore, the conductive nature of the structure prevents the use of radio communications. Applications involving sealed containers also have a requirement for power delivery, as the periodic changing of batteries is not possible.

Ultrasound has previously been identified as an attractive approach but there are two key challenges: efficient/reliable ultrasonic transduction and a method of overcoming the inherent multipath distortion resulting from boundary reflections. Previous studies have utilised piezoelectric contact transducers, however, they are impractical due to their reliance on coupling, i.e. the bond between the transducer and the metal surface, which leads to concerns over long term reliability. A non-contact transducer overcomes this key drawback, thus highlighting the electromagnetic acoustic transducer (EMAT) as a favourable alternative. This thesis presents the design and testing of an EMAT with appropriate characteristics for through-metal data communications.

A low cost, low power data transmission scheme is presented for overcoming acoustic multipath based on pulse position modulation (PPM). Due to the necessary guard time, the data rate is limited to 50kbps. A second solution is presented employing continuous wave, Quadrature phase shift keying (QPSK) modulation, allowing data rates in excess of 1Mbps to be achieved. Equalisation is required to avoid intersymbol interference (ISI) and a decision feedback equaliser (DFE) is shown to be adept at mitigating this effect.

The relatively low efficiency of an EMAT makes it unsuitable for power delivery, consequently, an alternative non-contact approach, utilising inductive coupling, is explored. Power transfer efficiency of $\approx 4\%$ is shown to be achievable through 20mm thick stainless steel.

To my family

Acknowledgements

It is a pleasure to thank the many people who made this thesis possible.

First and foremost I would like to thank my first supervisor, Jeff Neasham, for his support and guidance throughout this project. Without his limitless enthusiasm and patience, I doubt this thesis would ever have come to fruition. Likewise, I would like to thank my second supervisor, Prof. Bayan Sharif for sharing his vast experience in the field of digital communications.

I am indebted to the ICS department of BAE Systems Submarine Solutions, led by Jon Silvie, for partly funding this work and also for making their unique facilities available for field trials. I also gratefully acknowledge the EPSRC for their significant funding contribution.

The hardware prototypes evaluated in this thesis would not have been possible without the assistance of the mechanical, electronic and IT technical staff at Newcastle University. Furthermore, Jack, Chris, Stuart, Alan and Luke always made me feel welcome in the workshop even when my frequent design revisions had earned me the nickname, "can you just...?"

Newcastle University has been far more than just a place of study during my time here which is mainly due to the many friends I have made along the way. Andy and Bear deserve a special mention for always being there from the very beginning, through the highs and lows of both undergraduate and postgraduate life. I would also like to give a mention to Gerry for making sure the Sea Lab never had a dull moment.

Beyond the campus limits I would like to thank my closest friends, Carl, Al, Elaine and Jen, for always reminding me that there is more to life than the university walls.

Finally, I would like to thank my father and sister, the most wonderful people in the world, for their love and encouragement and to whom I dedicate this thesis.

Contents

List of Figures

List of Tables

List of Publications

D. J. Graham, J. A. Neasham, B. S. Sharif, "Investigation of Methods for Data Communication and Power Delivery Through Metals," *Industrial Electronics, IEEE Transactions on*, vol. 58, no. 10, pp. 4972-4980, Oct. 2011.

D. J. Graham, J. A. Neasham, and B. S. Sharif, "High bit rate communication through metallic structures using electromagnetic acoustic transducers," in OCEANS 2009-EUROPE, 2009. OCEANS 09., May 2009, pp. 16.

Nomenclature

Roman Symbols

A_m	Amplitude
$\mathbf{B}$	Magnetic flux density
B_R	Remanence
C	Capacitance
c	Speed of sound
$\mathbf{c}^H$	Stiffness tensor
C_c	Channel capacity
$\mathbf{D}$	Electric displacement field
$\mathbf{d}$	Piezomagnetic strain coefficients
D	Diameter
$d_{\min}$	Minimum Euclidean distance
$\mathbf{E}$	Electric field
$\mathbf{e}$	Converse piezomagnetic stress coefficients
e_n	Error signal
F	Force
f	Frequency
f_b	Data rate
f_c	Centre frequency
f_s	Sampling frequency
G	Shear modulus

$g(t)$	Pulse shape
$\mathbf{H}$	Magnetic field
H_C	Coercivity
I	Current
$\mathbf{J}$	Current density
j	Imaginary unit
k	Coupling coefficient
$k_{1,2}$	Wavenumber
k_L	Input symbol block length
$\mathbf{K}_n(t)$	Kalman gain vector (RLS)
L	Self inductance
$\mathbf{M}$	Magnetization
M	Mutual inductance
M	Modulation order
$n_{1,2}$	Refractive index
N_f	Near field length
n_L	Codeword length
P	Electrical power
$\mathbf{P}_n(t)$	Correlation matrix inverse (RLS)
Q_{Ah}	Battery Capacity
Q_h	Heat
Q	Quality factor
R	Electrical resistance
r	Coding rate
R_L	Load Resistance
$\mathbf{R}$	Autocorrelation matrix
$\mathbf{S}$	Strain tensor

s_n	Information symbol
$S_n(t)$	Symbol set
$\mathbf{T}$	Stress tensor
t	Time
T_c	Chip duration
T_d	Time until primary multipath arrival
T_G	Guard interval
T_m	Multipath duration
T_O	OFDM symbol period
T_p	Data Throughput
T	Symbol duration
T_w	Acoustic transit time
V	Voltage
w_k	Filter coefficient
$\mathbf{w}_n(t)$	Filter coefficients (RLS)
$\mathbf{x}$	Filter input
Y	Young's modulus
Z	Electrical impedance
z	Distance in z-direction
$Z_{1,2}$	Specific acoustic impedance
Z_R	Reflected impedance
z_{wall}	Wall thickness
z_{coat}	Wall coating thickness
Z'	Matching acoustic impedance

Greek Symbols

α	Attenuation coefficient
α_2	Wavenumber real part

α_r	Reflection coefficient
α_t	Transmission coefficient
β_2	Wavenumber imaginary part
γ	Gradient of the magnetostriction curve
Δ	Step-size parameter (LMS)
δ	Electromagnetic skin depth
Δf	Bandwidth
$\delta(t)$	Dirac delta impulse
ϵ	Magnetostriction
$\varepsilon_{\text{bavg}}$	Average energy per bit
ε	Strain
η	Power transfer efficiency
θ	Angle
θ_m	Carrier phase
κ	Conversion constant (hrs→s)
λ	Wavelength
λ_f	Forgetting factor (RLS)
λ_l	Loss factor
μ	Permeability
ν	Poisson's ratio
ρ	Density
σ	Conductivity
Φ	Magnetic flux
ω	Angular frequency

Superscripts

$^{\text{bk}}$	Feedback filter coefficient
$^{\text{fw}}$	Forward filter coefficient

$^{(L)}$ Lorentz force component

$^{(M)}$ Magnetization force component

$^{(MS)}$ Magnetostrictive component

Subscripts

$_0$ Initial or time-independent quantity

$_I$ Incident

$_{\text{opt}}$ Optimal

$_{\parallel}$ Parallel

$_p$ Parallel electrical component

$_{\perp}$ Perpendicular

$_R$ Reflected

$_{\text{RMS}}$ Root Mean Square

$_{rx}$ Relating to receiver side

$_s$ Series electrical component

$_T$ Transmitted

$_t$ Total field

$_{tx}$ Relating to transmitter side

$_x$ Component in x-direction

$_y$ Component in y-direction

$_z$ Component in z-direction

Acronyms

AC Alternating Current

AEF Acoustic Electric Feedthrough

ARQ Automatic Repeat Request

ASK Amplitude Shift Keying

AWGN Additive White Gaussian Noise

BER Bit Error Rate

BP Bandpass

CRC Cyclic Redundancy Check

DFE Decision Feedback Equaliser

DSP Digital Signal Processor

EMAT Electromagnetic Acoustic Transducer

ESR Equivalent Series Resistance

FE Finite Element

FEC Forward Error Correction

FFT Fast Fourier Transform

FIR Finite Impulse Response

FPGA Field Programmable Gate Array

FSE Fractionally Spaced Equaliser

HPRS Hull Penetrator Replacement System

HY80 High yield strength steel (min. 80 ksi)

I/O Input/Output

IPT Inductive Power Transfer

IR Impulse Response

ISI Intersymbol Interference

LCR Inductance, capacitance, resistance

LE Linear Equaliser

LMS Least Mean Square

LP Low Pass

LR-WPAN Low-rate Personal Area Network

MFB Multiple Feedback Bandpass

ML Maximum Likelihood

MSE Mean Square Error

NDE Non-Destructive Evaluation

NDT Non-Destructive Testing

Nd:YAG Neodymium-doped Yttrium Aluminium Garnet

o.d. Outer Diameter

OFDM Orthogonal Frequency Division Multiplexing

PAM Pulse Amplitude Modulation

PAPR Peak to Average Power Ratio

PCB Printed Circuit Board

PN Pseudo-random Number

PPM Pulse Position Modulation

PSK Phase Shift Keying

PWM Pulse Width Modulation

PZT Lead Zirconate Titanate

QAM Quadrature Amplitude Modulation

RF Radio Frequency

RFID Radio Frequency Identification

RISC Reduced Instruction Set Computing

RLS Recursive Least Squares

RMS Root Mean Square

Rx Receive

SHM Structural Health Monitoring

SL Spreading Loss

SNR Signal to Noise Ratio

SPI Serial Peripheral Interface

SPICE Simulation Program with Integrated Circuit Emphasis

SWG Standard Wire Gauge

TL Transmission Loss

Tx Transmit

USART Universal Synchronous Asynchronous Receiver Transmitter

USB Universal Serial Bus

Chapter 1

Introduction

Significant advancements in electronic communications technology have helped shape the modern world. With each advance, information can be shared with increasing speed, reliability and ease, which influences business, industry and even human social interaction. Throughout years of research, engineers have overcome the challenges associated with many different transmission media, including copper wire, optical fibre, air, vacuum and water. This has allowed communication across the globe, to the deepest reaches of the solar system and to the depth of the ocean. Despite these achievements, ever greater demands are placed on performance, which continually presents new challenges.

In an effort to improve safety, efficiency and reduce costs, there is an increasing demand in industry to monitor systems, processes, machines and other hardware in real-time. This drive has been greatly aided by advances in radio frequency (RF) wireless communications, which allows data from remote sensors to be effortlessly conveyed to a control system or datalogger. However, oil, gas, military, chemical processing and civil nuclear sectors make extensive use of metallic structures or 'conductive armours', which RF transmissions cannot penetrate. Examples of these structures include pipelines, ship hulls, chemical vats and containment flasks. In each case, it is highly undesirable to breach the wall of the armour for reasons of structural integrity, preventing a hard-wired solution. Consequently, there is a demand for through metal communications and power delivery as an enabling technology. As a transmission medium for data and power, the metal wall channel is relatively new and novel, with very few published works in the field.

Acoustic waves are known to have excellent propagation characteristics in metals and, for this reason, acoustic techniques are used extensively in the field of non-destructive testing (NDT). A typical 'pulse-echo' ultrasonic inspection system launches an acoustic wave into a material by means of a piezoelectric transducer coupled to the surface, and analyses the reflections. This sort of system demonstrates the ability to readily convey energy through a metal wall and, hence, it is a logical

starting point for a through metal communications and/or power delivery system. In fact, all previous published works have used ultrasonic piezoelectric transducers as the basis of their respective systems. The simplest setup requires two co-axially aligned transducers either side of the metal wall, which is generally referred to as a 'pitch-catch' arrangement.

The key challenge associated with any acoustic approach is multipath distortion. Boundary reflections, which are essential for the operation of an ultrasonic inspection system, are detrimental to a digital communications system and result in intersymbol interference (ISI). This phenomenon is commonly encountered in the underwater acoustic channel and various radio channels. A range of techniques are explored to mitigate the effects of ISI and achieve reliable data communications for the specific case of a metal wall channel. This includes both low power, low throughput approaches and maximum data rate systems.

A significant practical limitation, specific to piezoelectric transducers, relates to coupling, i.e. the physical interface between the transducer and the wall. The transducer requires bonding with a couplant material, typically a gel or resin, to provide a good acoustic transmission path between the piezoelectric and wall. System performance is reliant on the quality of the bond, which is inhibited by corrosion or any coatings applied to the metal, such as paint or enamel, and hence, there are concerns over long term reliability. The practicality of a solution is largely determined by the ease and speed with which it can be deployed and also the likelihood of failure. From this point of view, the coupling issue related to piezoelectric transducers is far from ideal. A non-contact approach overcomes this limitation and therefore is a key theme throughout this work.

Inductive power transfer (IPT) is becoming increasing popular for a variety of short range wireless power transfer applications, but there are no technical papers analysing its applicability to the metal wall channel. The technique transfers energy from a transmitting coil to a receiving coil via the alternating magnetic field linking the two. This mechanism potentially offers an alternative to acoustics for through metal communications and power transfer applications. Understanding and quantifying the losses associated with inductive coupling through a metal wall channel is a key area of investigation.

The overall aim of this thesis is to develop a practical solution for through metal communications and power delivery, and to contrast and compare with previous systems. Due to the collaboration with industrial sponsors, BAE Systems, there is also a requirement to demonstrate any proposed techniques in hardware. The structure of this thesis is outlined in the following paragraphs.

Chapter 2 presents a review of three transduction mechanisms, RF, acoustics and inductive coupling, to assess their applicability for use with a metal wall channel.

Background theory relating to the three schemes is introduced and it is shown, using established theory, why RF communications cannot penetrate a sealed metal structure. The various means of acoustic wave generation are discussed, with special attention given to the electromagnetic acoustic transducer (EMAT) due to its favourable properties for through metal communications applications. Inductive coupling is introduced as a potential alternative to acoustics for power delivery. The chapter concludes with a literature review covering the current state-of-the-art.

Chapter 3 provides an in depth analysis of the EMAT; a non-contact acoustic transducer. The coupling mechanism, i.e. the means of ultrasonic generation, is complex and is explained with the aid of the current theoretical model. A design is presented for both an EMAT transmitter and EMAT receiver, including the physical transducer and supporting electronics. The hardware is novel with respect to the proposed application and is evaluated in terms of its suitability for through metal communications.

Chapter 4 analyses the impulse response of the metal wall channel and proposes burst mode transmission techniques as a method of overcoming the inherent multipath associated with acoustic transmission through metals. The 'Acoustic Gateway Demonstrator System' is presented: a low cost, low power, through metal communications system designed specifically to forward wireless sensor network traffic through the steel bulkheads of a naval vessel and enable ship-wide connectivity. The design incorporates EMATs to allow rapid deployment on a painted surface and pulse position modulation (PPM) to overcome multipath and achieve reliable communications. Field trial results demonstrate the system to offer significant practical advantages over previous systems.

Chapter 5 investigates methods of increasing the throughput of a through metal communications system. Alternative modulation schemes are proposed, which are far more bandwidth efficient than the previously discussed burst mode techniques. Multi-carrier and single carrier schemes are considered, including orthogonal frequency division multiplexing (OFDM) and phase shift keying (PSK). Receiver structures, required by single carrier schemes, are evaluated in terms of their applicability for a metal wall channel. The linear equaliser (LE) and decision feedback equaliser (DFE) are compared using simulation and experimentally captured data packets.

Chapter 6 proposes inductive power transfer as an alternative non-contact approach for through metal power delivery. The technique utilises two inductively coupled coils to transfer energy using a low frequency magnetic field. A combination of analytical modelling, experimentation and finite element simulation demonstrate that optimal performance is achieved with the appropriate selection of load and operating frequency. These optimal values are heavily dependent on the electrical and magnetic properties of the material as well as the physical dimensions. Power

transfer efficiency is calculated for a 20mm-thick stainless steel plate. Low data rate inductive communications are also considered.

Chapter 7 draws together the findings of the preceding chapters and highlights the key contributions of this work to the field of through metal communications and power delivery. Some of the author's thoughts regarding future work are also presented.

Chapter 2

Transduction Mechanisms

In this chapter, consideration is given to a range of transduction mechanisms, which are assessed in terms of their suitability for through metal communications and power delivery. In order to properly evaluate each method, it is important to begin by defining the generalised scenario of interest.

It is assumed that 'the wall' is a conducting barrier, of thickness, z_{wall}, and has infinite dimensions in the x-y plane. The material of the wall is referred to as 'metal' but may include other conducting media, such as carbon fibre. Each side of the wall is assumed to be covered by a non-conductive coating of thickness, z_{coat}, and typically $z_{\text{coat}} \ll z_{\text{wall}}$. This coating is to account for protective or anti-corrosive layers typically applied to metal surfaces in many practical applications. The wall and its coatings separate the air filled regions, 1 and 2, as shown in Fig. 2.1.

A successful solution should allow communication and/or power transfer from region 1 to region 2, without the need for any physical alterations to the the wall or its coatings. This requirement immediately *prevents the use of a hard-wired solution.*

To further aid the assessment of the transducers, consideration should also be given to any further constraints imposed by the requirements of end-user applications, which may be classified into two distinct groups as shown in Fig. 2.2; A, an asymmetrical setup involving sealed containers, whereby power must be provided via an external source to obtain data from within; and B, gateways (data repeaters) to enable wireless communications within large metallic structures (e.g. ships).

This chapter appraises the suitability of radio, inductive and acoustic approaches.

2.1 Radio Frequency Communications

The most common and easily deployable method of wireless electronic communications is radio, so it is logical that a radio frequency solution should be considered.

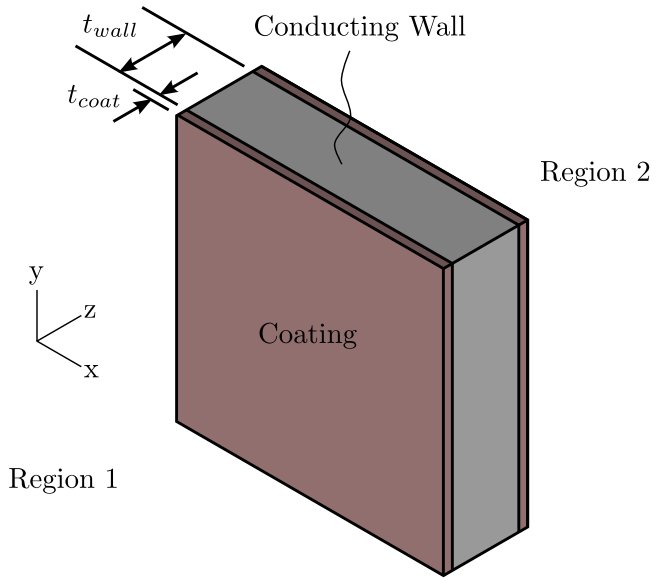

Figure 2.1: Scenario of interest. A coated, conducting wall, separating air-filled regions 1 and 2.

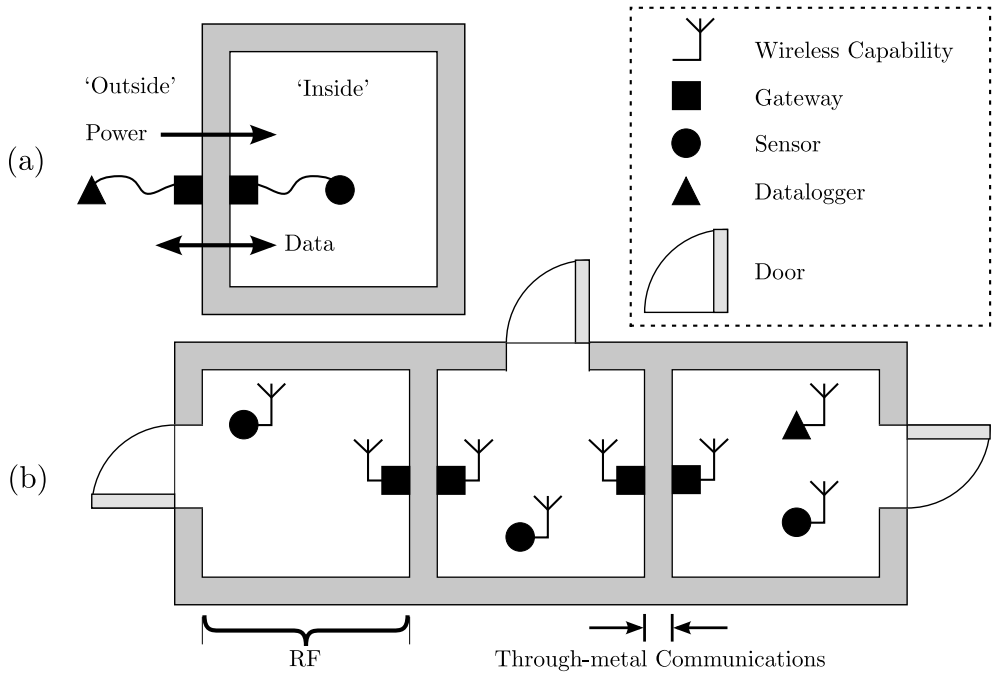

Figure 2.2: Common through metal applications. (a) Scenario A, sealed containers requiring asymmetric communications and power delivery. (b) Scenario B, large structures requiring a data link, possibly to enable wireless networking.

To determine the suitability of radio, it is important to understand the behaviour of an electromagnetic wave when it is incident on a good conductor. The problem has been analysed in many texts on electromagnetic wave theory. This section provides a brief overview using the notation of Lorrain and Corson [1].

The analysis begins by considering a linearly polarized, sinusoidal electromagnetic wave in a dielectric, travelling in the z-direction. The Electric field, $\mathbf{E}$, is described by (2.1) and (2.2), where $\mathbf{E}_m$ is a vector independent of time and the coordinates, k_1 is the wavenumber, ω is angular frequency and λ_1 is the wavelength. An equivalent expression exists for the Magnetic field, $\mathbf{H}$.

$$\mathbf{E} = \mathbf{E}_m e^{j(\omega t - k_1 z)} \tag{2.1}$$

$$k_1 = \frac{2\pi}{\lambda_1} \tag{2.2}$$

When propagating within a conductor, the wave will experience an attenuation and the Electric field takes the form (2.3).

$$\mathbf{E} = \mathbf{E}_m e^{-(\alpha_2 z)} e^{j(\omega t - \beta_2 z)} \tag{2.3}$$

The corresponding wavenumber, k_2, is now complex and may be expressed in terms of two variables, α_2 and β_2 (2.4). In the case of a good conductor, α_2 and β_2 are determined from the electromagnetic skin depth, δ (2.5).

$$k_2 = \beta_2 - j\alpha_2 \tag{2.4}$$

$$\alpha_2 = \beta_2 = \frac{1}{\delta} \tag{2.5}$$

The skin depth of a material is dependent on the frequency of the wave, ω, the conductivity of the material, σ, and the permeability of the medium, μ, as given in (2.6). After propagating a distance equal to one skin depth, the amplitude of the wave is reduced by a factor of e ($\approx 36.79\%$).

$$\delta = \sqrt{\frac{2}{\omega\sigma\mu}} \tag{2.6}$$

If an electromagnetic wave, travelling in a dielectric, is incident on a good conductor, some proportion of the wave will reflect and some will be transmitted into the conductor. If the incident wave may approach from any angle, θ_I, then the expressions

for the incident, $\mathbf{E}_I$, reflected $\mathbf{E}_R$ and transmitted waves, $\mathbf{E}_T$, become, (2.7), (2.8) and (2.9) respectively.

$$\mathbf{E}_I = \mathbf{E}_{Im} \exp j\left(\omega t - k_1 x \sin\theta_I + k_1 z \cos\theta_I\right) \tag{2.7}$$

$$\mathbf{E}_R = \mathbf{E}_{Rm} \exp j\left(\omega t - k_1 x \sin\theta_I - k_1 z \cos\theta_I\right) \tag{2.8}$$

$$\mathbf{E}_T = \mathbf{E}_{Tm} \exp j\left(\omega t - k_1 x \sin\theta_I + k_2 z \cos\theta_T\right) \tag{2.9}$$

The expression for the transmitted wave may be rearranged in terms of the refractive indexes of medium 1 and medium 2, n_1 and n_2 (2.10).

$$\mathbf{E}_T = \mathbf{E}_{Tm} \exp j\left[\omega t - k_1 x \sin\theta_I + k_2 z \sqrt{1 - \left(\frac{n_1}{n_2}\right)^2 \sin^2\theta_I}\right] \tag{2.10}$$

For the case of a transition from a dielectric to a good conductor, the ratio of the refractive indexes becomes (2.11).

$$\frac{n_1}{n_2} = \frac{k_1}{k_2} = \frac{2\pi\delta}{(1-j)\,\lambda} \tag{2.11}$$

$$\left|\frac{n_1}{n_2}\right| = \frac{\sqrt{2}\pi\delta}{\lambda_1} \ll 1 \tag{2.12}$$

Because the magnitude of the ratio of refractive indexes is very small, it can then be shown that the transmitted wave propagates normal to the interface, regardless of the angle of incidence (2.13). This is shown in Fig. 2.3.

$$\mathbf{E}_T \approx \mathbf{E}_{Tm} e^{j\left(\omega t - \frac{z}{\delta}\right) - \frac{z}{\delta}} \tag{2.13}$$

Fresnel's equations can be used to determine the relative amplitudes of the transmitted and reflected waves [2, 3]. For a wave polarised with $\mathbf{E}$ normal to the plane of incidence, the approximations in (2.14) and (2.15) are valid for any angle of incidence.

$$\left(\frac{E_{Rm}}{E_{Im}}\right)_\perp = \frac{\frac{n_1}{n_2}\cos\theta_I - \cos\theta_T}{\frac{n_1}{n_2}\cos\theta_I + \cos\theta_T} \approx -1 \tag{2.14}$$

$$\left(\frac{E_{Tm}}{E_{Im}}\right)_\perp = \frac{2\frac{n_1}{n_2}\cos\theta_I}{\frac{n_1}{n_2}\cos\theta_I + \cos\theta_T} \approx 0 \tag{2.15}$$

For waves polarised with $\mathbf{E}$ parallel to the plane of incidence, the approximations in (2.16) and (2.17) are valid for all angles of incidence with the exception of grazing incidence.

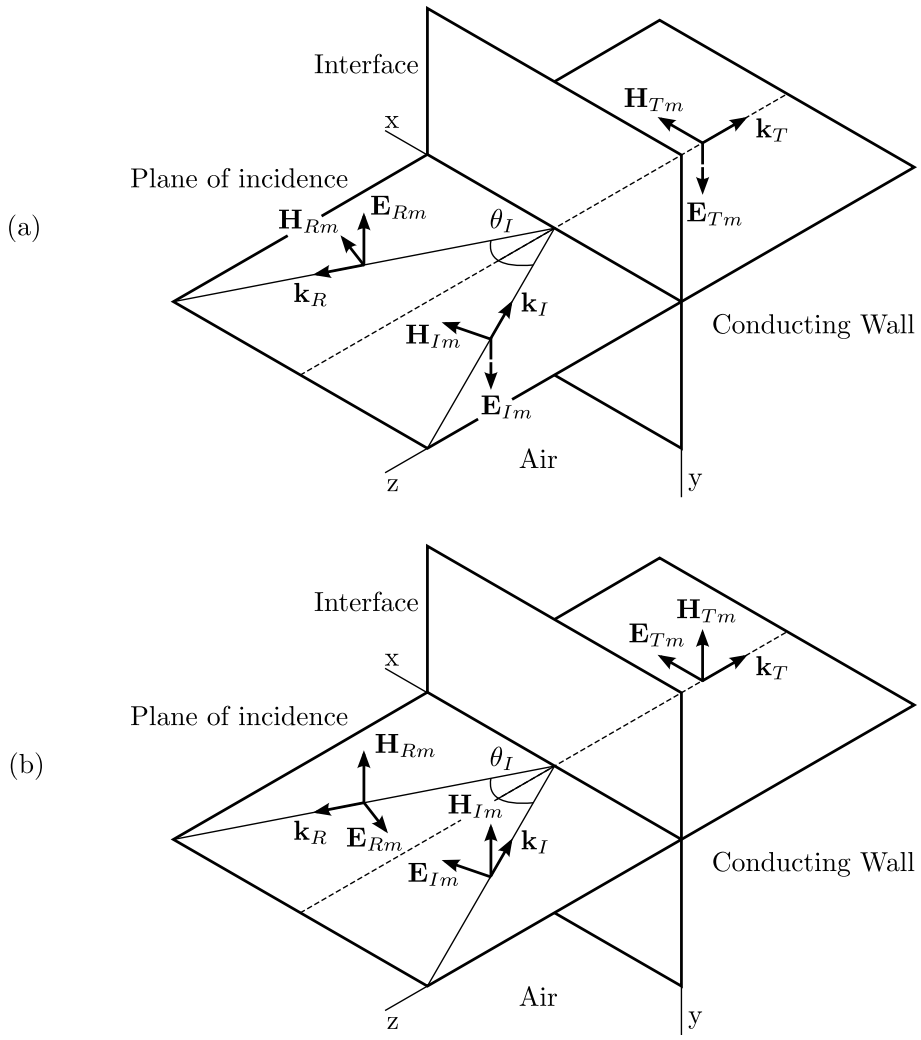

Figure 2.3: An electromagnetic wave incident on a good conductor. (a) **E** vector of the incident wave normal to the plane of incidence. (b) **E** vector of the incident wave parallel to the plane of incidence.

$$\left(\frac{E_{Rm}}{E_{Im}}\right)_{\parallel} = \frac{\frac{n_1}{n_2}\cos\theta_T - \cos\theta_I}{\frac{n_1}{n_2}\cos\theta_T + \cos\theta_I} \approx -1 \tag{2.16}$$

$$\left(\frac{E_{Tm}}{E_{Im}}\right)_{\parallel} = \frac{2\frac{n_1}{n_2}\cos\theta_I}{\cos\theta_I + \frac{n_1}{n_2}\cos\theta_T} \approx 0 \tag{2.17}$$

Fresnel's equations show that normal or parallel polarised waves, incident at almost any angle on a good conductor, will experience almost perfect reflection.

The proportion of the wave propagating into the material will be subject to attenuation due to skin effect, as per (2.6), and will also experience a subsequent boundary loss transitioning back into air at the far side. However, due to the negligible proportion of the wave which transitions into the material after the initial reflection, these losses need not be evaluated for it to be clear that *it is not possible to transmit enough RF power through a conducting wall to establish a viable communications link.*

2.2 Inductive Coupling

Two conductors are referred to as mutual-inductively coupled when a change in current flow, I_1, through one wire induces a voltage, V_2, across the ends of the other wire through electromagnetic induction (2.18). The voltage is determined by the number of turns, N and the rate of change of magnetic flux, Φ. If a load is connected to the secondary conductor, such that a current can flow, energy is transferred. Hence, inductive coupling has the potential to wirelessly transmit data and power through a barrier separating two conductors.

$$V = -N\frac{d\Phi}{dt} \tag{2.18}$$

The mutual inductance, M, is a measure of the degree of coupling between two conductors (2.19).

$$V_2 = -M\frac{dI_1}{dt} \tag{2.19}$$

If I_1 is sinusoidal, (2.19) may be expressed as (2.20) [1].

$$V_2 = -j\omega M I_1 \tag{2.20}$$

The mutual inductance between two circuits is the same irrespective of which is excited with a driving current (2.21).

$$V_1 = -j\omega M I_2 \tag{2.21}$$

The negative relation of (2.21) and (2.20) is due to Lenz's law, whereby an induced current always flows in such a direction as to oppose the motion or change causing it.

Mutual inductance may also be expressed in terms of the circuit self inductances, L_1 and L_2, and the coupling coefficient, k (2.22). With $k = 1$, the mutual inductance is the geometric mean of the self-inductances, that is, all the flux of the primary conductor links the secondary conductor.

$$M = k\sqrt{L_1 L_2} \qquad (k \leq 1) \tag{2.22}$$

Self inductance is the ratio of flux linkage, $N\Phi$, to current (2.23) and may also be expressed as the proportionality between the rate of change of current and induced voltage (2.24).

$$L = \frac{N\Phi}{I} \tag{2.23}$$

$$V_1 = L_1 \frac{dI_1}{dt} \tag{2.24}$$

2.2.1 Eddy Currents

Referring back to Fig. 2.1, consider the case where conductors (coils) are placed in regions 1 and 2, separated by a conducting wall. The flux linking the coils must intersect the wall and hence, there is mutual inductance between the coils and the wall. Free current, $\mathbf{J}$, and displacement currents, $\frac{\partial \mathbf{D}}{\partial t}$ are induced in the bulk conductor by the changing magnetic field, $\mathbf{H}$, according to the Maxwell−Ampere equation (2.25) and are termed eddy currents [4].

$$\mathbf{J} + \frac{\partial \mathbf{D}}{\partial t} = \nabla \times \mathbf{H} \tag{2.25}$$

Eddy currents are desirable in many applications, such as induction heating, eddy current brakes and eddy current inspection. However, for inductive through metal communications or power delivery, eddy currents result in energy loss in the form of heat, Q_h, as described by Joule's first law (2.26), where I is the current, R is the electrical resistance and t is the time.

$$Q_h = I^2 \cdot R \cdot t \tag{2.26}$$

Moon [4] has shown a magnetic field decays exponentially into a conductive material according to the material skin depth (2.27), which is analogous to the decay of electromagnetic waves, as discussed in Section 2.1. The conductor effectively shields the interior from the applied field by the induction of eddy currents, whose own magnetic field oppose the applied field. The resultant eddy current density, J_e, also decays exponentially into the material, relative to the surface density, J_S (2.28).

$$B = B_0 e^{\left(\omega t - \frac{z}{\delta}\right)} e^{-\frac{z}{\delta}} \tag{2.27}$$

$$J_e = J_S \, e^{-\frac{z}{\delta}} \tag{2.28}$$

It is clear that the skin depth of the material will have a direct effect on the performance of any inductive approach. Due to the frequency dependence of skin depth, eddy current losses and the shielding effect can be minimised by operating at low frequencies. The technique will obtain best results with low conductivity, low permeability materials or very thin walls.

2.2.2 Hysteresis Loss

If the conducting wall is ferromagnetic, an applied magnetic field causes magnetic domains within the wall, with orientations closely approximating the direction of the applied field, to grow at the expense of their neighbours, due to the migration of the domain walls [1]. The result is a net magnetization.

Ferromagnetic materials exhibit hysteresis whereby a net magnetization will remain after the removal of the magnetic field. If the applied magnetic field is time-varying and harmonic, energy is lost during each cycle. The energy dissipated per cubic metre of material is equal to the area within the hysteresis loop; a typical example is shown in Fig. 2.4.

Soft magnetic materials are used in the construction of motors and transformers to minimise hysteresis loss [5]. Attractive properties of soft magnetic materials include high permeability and a narrow hysteresis loop. For through metal communications and power applications, the magnetic properties of the wall are outside the control of the system designer. As a result, the applicability of inductive techniques will be limited to wall materials that do not exhibit large hysteresis losses.

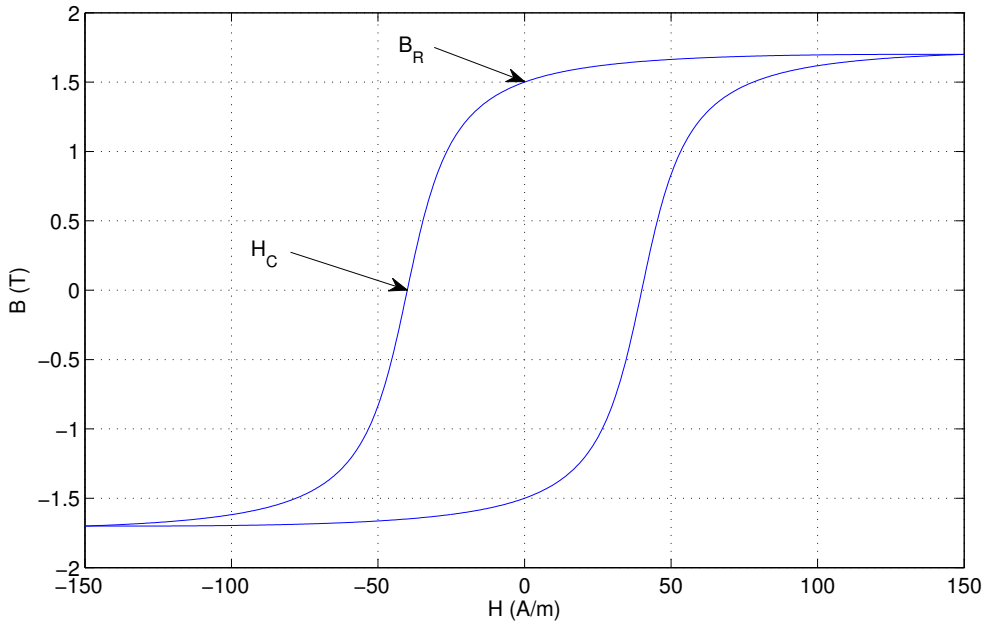

Figure 2.4: A typical hysteresis loop for steel. B_R and H_C denote the remanence and coercivity respectively.

2.3 Acoustic Techniques

The field of 'Acoustics' is the study of all mechanical waves in gases, liquids, and solids. The terms ultrasound, sound and infrasound are used to differentiate between mechanical waves with frequencies above, within and below the human audible range (20Hz - 20kHz) respectively. An 'acoustic wave' may refer to a mechanical wave of any frequency.

Acoustics have long been utilised in the fields of non-destructive testing (NDT), non-destructive evaluation (NDE) and structural health monitoring (SHM) [6–8]. Ultrasonic inspection relies on the excellent propagation characteristics of sound in elastic solids and demonstrates that acoustic energy can be transmitted through a metal wall. Consequently, an acoustic mechanism is an obvious solution for through metal data communications and power transfer. The following subsections explore the fundamentals of sound propagation and the properties of various acoustic transducers.

2.3.1 Sound Propagation Through Metal

In solids, sound waves can propagate in four principal modes: longitudinal waves, shear waves, surface waves or plate waves. As plate (Lamb) waves can only exist in

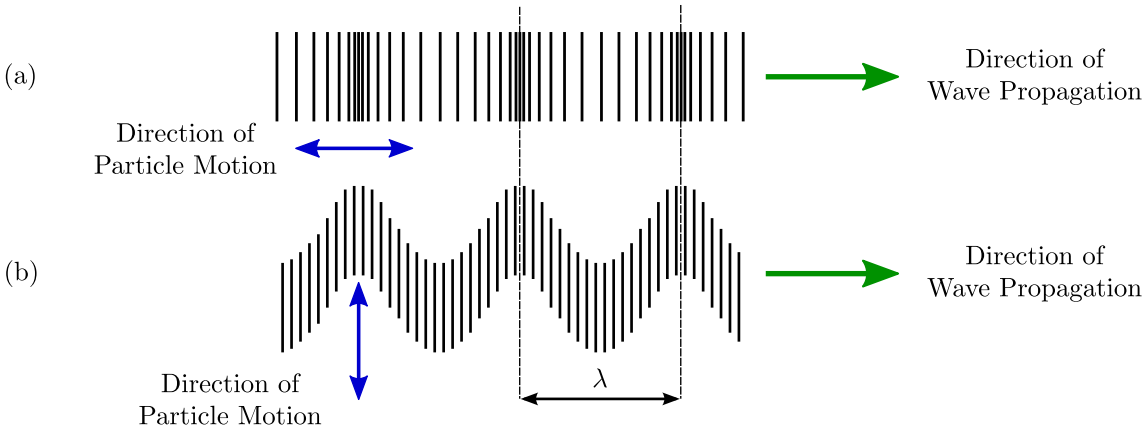

Figure 2.5: Two modes of sound propagation in solids. (a) Longitudinal. (b) Shear.

thin plate and surface (Rayleigh) waves propagate parallel to a surface, neither are suited to transmitting through a metal wall.

Longitudinal waves, also known as compressional or extensional waves, propagate in the same direction as the particle motion. The direction of propagation of a shear wave, also known as transverse wave, is perpendicular to the particle motion, as shown in Fig. 2.5.

The speed of a longitudinal wave propagating along a bar, c_B, is determined from the Young's Modulus, Y, and density of the material, ρ, as given in (2.29). When the orthogonal dimensions of the bar are greater than a few wavelengths, the medium is referred to as bulk material and shear elastic constants influence the speed of propagation. As a result, for a longitudinal wave propagating in bulk material, (2.29) is modified with Poisson's ratio, as given in (2.30) [9]. Poisson's ratio is a measure of the Poisson Effect, which is the tendency of a material under axial compression to expand in the perpendicular directions. Poisson's ratio, ν, is expressed formally in (2.32), where $\varepsilon_{\text{trans}}$ is transverse strain and $\varepsilon_{\text{axial}}$ is axial strain. The wavelength, λ, is defined in (2.33), where c is the wave speed and f is the frequency.

The speed of a shear wave is determined from the shear modulus, G, and the density of the material, ρ, as shown in (2.31). Expressing the shear modulus in terms of Young's Modulus and Poisson's Ratio shows that the longitudinal wave speed is always greater than the shear wave speed, i.e. $c_L > c_S$.

$$c_B = \sqrt{\frac{Y}{\rho}} \tag{2.29}$$

$$c_L = \sqrt{\frac{Y\,(1-\nu)}{\rho\,(1+\nu)\,(1-2\nu)}} \tag{2.30}$$

$$c_S = \sqrt{\frac{G}{\rho}} = \sqrt{\frac{Y}{2\rho\,(1+\nu)}} \tag{2.31}$$

$$\nu = -\frac{d\varepsilon_{\text{trans}}}{d\varepsilon_{\text{axial}}} \tag{2.32}$$

$$\lambda = \frac{c}{f} \tag{2.33}$$

It is worth noting that the speed of sound is not necessarily constant for a given material, as Young's Modulus is temperature dependent.

2.3.1.1 Attenuation

Acoustic attenuation is the decay rate of a wave as it propagates. There are three mechanisms contributing to this decay: spreading loss, scattering and absorption. Spreading loss, SL, in a bulk material, is spherical and is described mathematically in (2.34) as a function of distance, z.

$$\text{SL (dB)} = 20\log_{10} z \tag{2.34}$$

Scattering describes the redirection of the wave, as it propagates, due to non-uniformities in the medium. Absorption is the conversion of acoustic energy to other forms of energy, namely heat.

Scattering and absorption are grouped together to give an attenuation coefficient, α, for a given material. The complete transmission loss, TL, can then be expressed as per (2.35).

$$\text{TL (dB)} = 20\log_{10}(z) + \alpha z. \tag{2.35}$$

The attenuation coefficient is not a fixed value for a given material; it is highly frequency dependent [10]. Furthermore, manufacturing processes, such as cold working, can also have a significant impact on the attenuation coefficient as they change the mechanical properties of the material [11].

2.3.1.2 Reflection

When considering reflection, the thin wall coatings, described in the original problem definition, shall be ignored for simplification. A sound wave propagating within the wall will reflect at the wall boundaries due to an impedance mismatch. The relative amplitude of the reflected wave and incident wave can be expressed by means of a reflection coefficient, α_r. For any two materials, the reflection coefficient can be determined if the characteristic impedances, Z_1 and Z_2, are known (2.36) [12].

$$\alpha_r = \left(\frac{Z_2 - Z_1}{Z_2 + Z_1}\right)^2 \tag{2.36}$$

Minimum reflection is achieved with matched impedance i.e. $Z_2 = Z_1$, and in the case of a severe mismatch, $\alpha_r \to 1$ and reverberation will result.

Reflection can pose a problem when trying to excite sound into a material efficiently using a contact transducer. If the sound source and material are not acoustically matched, a large reflection will occur. This problem can be alleviated by means of a matching layer, constructed from a third material with specific acoustic impedance Z'. If the thickness of the material is equal to an odd number of quarter wavelengths then the transmission coefficient, α_t is given by (2.37) [13].

$$\alpha_t = \frac{4Z_1Z_2}{\left(Z' + \frac{Z_1Z_2}{Z'}\right)^2} \tag{2.37}$$

When $Z' = \sqrt{Z_1Z_2}$, $\alpha_t = 1$, and perfect transmission is achieved [13]. In practice a perfect matching material often does not exist.

2.3.1.3 Multipath Propagation and Intersymbol Interference

Multipath propagation is a phenomenon whereby a signal arrives at a receiver via multiple transmission paths. Each path may have a different length and/or propagation speed, resulting in a primary arrival and subsequent delayed multipath arrivals. This effect is common in many systems, two examples of which are shown in Fig. 2.6, and include RADAR and underwater communications [14]. In RADAR processing, multipath causes 'ghost' objects to appear and careful design and signal processing is required to distinguish which targets are real.

Multipath propagation in a communication channel results in intersymbol interference (ISI), whereby the current symbol is distorted by previous symbols. The presence of ISI in a system introduces errors in the decision device at the receiver output. With careful design, the effects of ISI can be minimised, resulting in the smallest possible error rate.

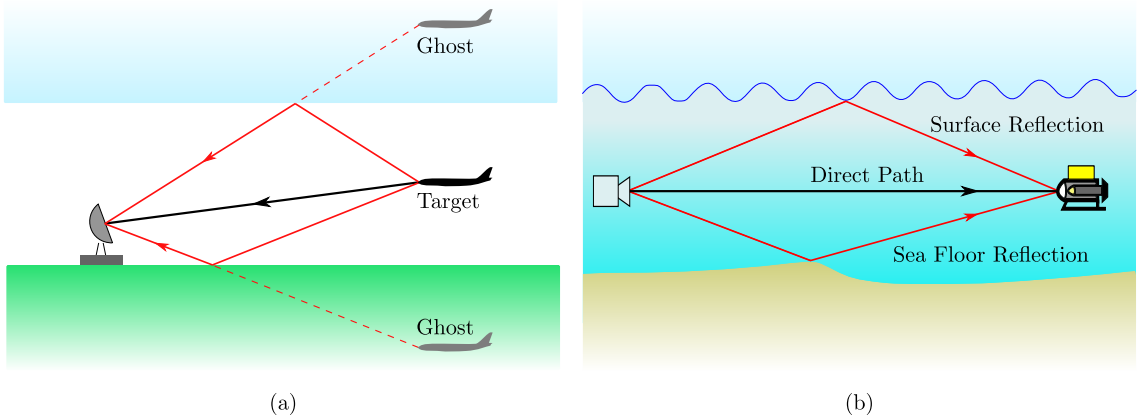

Figure 2.6: Examples of systems which experience multipath propagation. (a) RADAR. (b) Underwater acoustic communications.

2.3.1.4 Generic Impulse Response

For NDT applications, reflections contain information about the internal characteristics of the material. Hence, transducers are often deployed in a 'pulse-echo' mode of operation, whereby a single transducer is used to transmit and receive. The reverberation resulting from wall-air reflections is very useful for accurately measuring properties such as attenuation.

For a through metal communications system, a separate transmitter and receiver is required either side of the wall; this is referred to as 'pitch-catch' operation. Once an acoustic data symbol is sent and received, it continues to reverberate and becomes unwanted 'multipath', which can lead to intersymbol interference.

The mathematical function that describes the output of a dynamic system when excited by a brief input signal is referred to as the impulse response. An impulse response describes the system output as a function of time and can be used to visualise channel multipath.

The generic impulse response for a metal wall channel describes a simplified case but illustrates key features. It is assumed an ultrasonic source is aligned co-axially with a receiver on opposite sides of an uncoated, non-dispersive metal wall with planar surfaces. Under these assumptions, the impulse response can be described as follows [15]: 1. A primary pulse is received after period, T_w, which is determined from the wall thickness, z_{wall}, and speed of propagation; 2. Subsequent received pulses are scaled and shifted copies of the primary pulse, arriving at odd multiples of T_w. The impulse response is described formally in (2.38), where, $\delta(t)$ is the Dirac delta impulse, T_w is the transit time through the wall and α is an attenuation constant relating the amplitude of successive echoes.

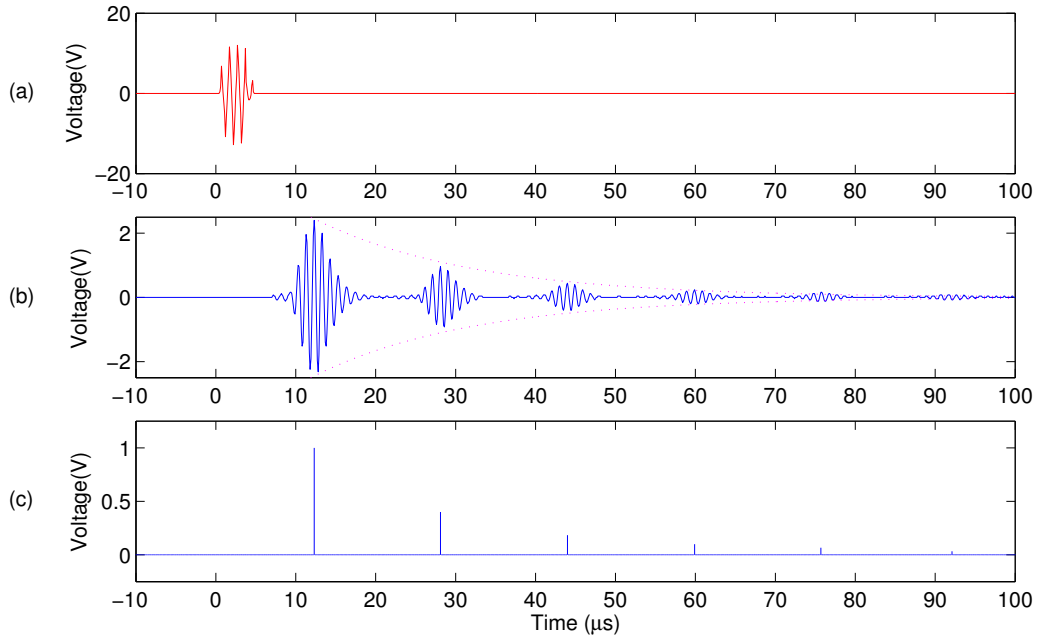

Figure 2.7: The generic impulse response of a metal wall channel. (a) Transmit pulse, (b) impulse response, and (c) simplified channel model.

$$\mathrm{IR}(t) = \sum_{n=0}^{\infty} \delta\left(t - (1+2n)\,T_w\right) \alpha^{1+2n} \qquad (0 < \alpha < 1) \tag{2.38}$$

The generic impulse response of a metal wall channel is shown in Fig. 2.7.

2.3.1.5 Frequency Selective Fading

A consequence of multipath propagation is frequency selective fading [16]. A single frequency continuous wave transmission, when received, becomes the summation of the original signal and any multipath arrivals. The summation can be constructive or destructive depending on the phase relationship. As a result, the frequency response of a multipath channel exhibits peaks and troughs across the spectrum. Frequencies which experience almost complete cancellation are referred to as 'nulls' or 'deep fades'.

2.3.2 Piezoelectric Transducers

The direct piezoelectric effect is the internal generation of electrical charge resulting from an applied mechanical force. This phenomenon is exhibited in a range of solid

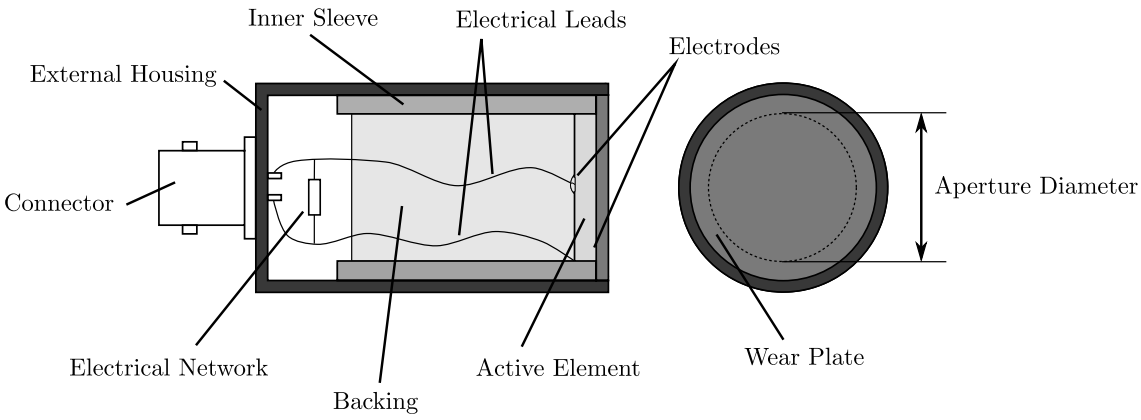

Figure 2.8: Typical construction of an NDT type piezoelectric transducer.

materials but most notably in crystals and ceramics such as Quartz, Barium titanate and Lead zirconate titanate (PZT) [17].

A slice of piezoelectric material is used as the active element in a piezoelectric transducer. It is the direct piezoelectric effect that allows the element to operate as a receiver of acoustic energy; a mechanical oscillation induces an alternating electric potential across the element, which is proportional to the mechanical pressure.

Piezoelectric materials also exhibit the inverse piezoelectric effect, whereby the internal generation of a mechanical force results from an applied electrical field, allowing the transducer to also operate as a transmitter of acoustic energy.

The piezo material can be cut on various axes to produce different modes of vibration. Longitudinal wave mode transducers are by far the most common due to the required use of couplant, as discussed in Section 2.3.2.2. The thickness of the slice determines the resonant frequency and hence, higher frequency transducers require increasingly thin active elements.

The construction of a piezoelectric transducer is shown in Fig. 2.8. A thin conducting layer is deposited onto both sides of the active element to allow electrical connection. Electrical leads and a matching network interface the active element to a standard external connector. Backing material is used for mechanical damping, which reduces the quality factor, Q, of the transducer, increasing bandwidth. The transducer is encased by a rugged external housing and the active face is covered by a wear plate to prevent damage to the active element.

2.3.2.1 Focal length

A plane wavefront emitted from a piston source, such as a piezoelectric disc, is subjected to diffraction effects due to the finite size of the aperture. Constructive

and destructive interference is experienced by the wavefront, resulting in a non-uniform field with local maxima and minima. The position of the last maximum is located at the near field length, N_f, and is dependent on the wavelength, λ, and aperture diameter, D.

$$N_f = \frac{D^2}{4\lambda} \tag{2.39}$$

Beyond the near field distance, the wavefront is considerably more uniform and this region is referred to as the far field. To ensure predictable performance, it is desirable to always operate in the far field region, hence, the thickness of the wall defines the maximum transducer diameter for a through metal communications system.

2.3.2.2 Acoustic Coupling

To generate an ultrasonic wave in a material, piezoelectric transducers require direct physical contact. The acoustic impedance of both the transducer and metal wall are very high, whereas the acoustic impedance of air is very low. As a result, any air-gap will result in total reflection of the incident acoustic wave at the transducer interface; no acoustic energy will be transmitted into the wall. To ensure good contact, a viscous couplant gel is often used in NDT applications. The gel compensates for non-uniformities in the surfaces and provides a much better impedance match than air, improving transmission efficiency. Another option, for a more permanent fit, is to bond the transducer with epoxy resin.

One of the key features of the wall that has major implications on effective coupling is the wall coating. This coating is inherent to each application and is out of the control of the system designer. Specifically, for a piezoelectric solution, the key parameters of the coating are the acoustic impedance and the quality of the bond to the metal. If either of these properties are non-ideal, large reflections will result, as illustrated in Fig. 2.9a, and can ultimately make a contact piezoelectric solution impractical. It is important to reiterate that *any proposed solution should not make any modifications to the wall or its coatings.*

Another issue resulting from coupling is a concern over long term reliability; should any of the bonds degrade or fail, the system will cease to function.

2.3.3 Laser Generation

Ultrasound can be generated with a pulsed laser by means of the thermoelastic effect [18]. The laser heats a small disc of material at the surface of the material with a depth determined by heat diffusion [19]. Compression mode elastic waves

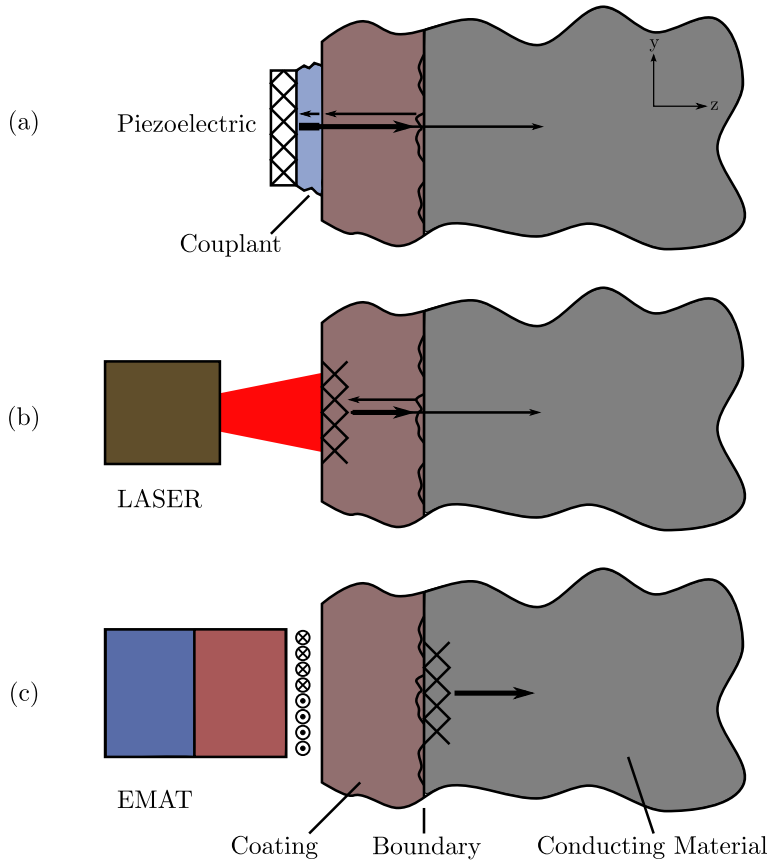

Figure 2.9: A comparison of the acoustic coupling of: (a) piezoelectric transducers, (b) LASER generation, (c) EMATs. The source of the acoustic wave is indicated with a cross hatch and arrows illustrate acoustic propagation and reflection.

are generated from the strains arising from thermoelastic expansion. A Q-switched, neodymium-doped yttrium aluminium garnet (Nd:YAG) laser is typically used to produce the pulse [20, 21].

Although laser generation is a non-contact technique and can operate at very large liftoff distances, it does not overcome all the issues associated with piezoelectrics. Ideally, the laser should be incident directly onto the metal. Laser generation may be ineffectual when inducing sound into an unspecified surface coating. Furthermore, any sound induced in the coating still has to successfully propagate into the metal and hence, suffers from the same impedance matching problems as a piezoelectric transducer, as shown in Fig. 2.9b.

The added complexity, cost and associated safety issues of a laser based system largely outweigh any other advantages it may offer.

2.3.4 Electromagnetic Acoustic Transducer (EMAT)

An electromagnetic acoustic transducer (EMAT) is a non-contact probe with limited applications in NDT such as elevated temperature [22], precise attenuation [23, 24], or other niche measurements [25–27]. There are no reports in previous literature of this type of transducer being used for electronic communications.

2.3.4.1 EMAT Construction and Operation

The construction of an EMAT consists of a permanent magnet and a coil excited at radio frequencies. The transducer generates acoustic waves in a conductive surface via a combination of the Lorentz force, magnetizing force and magnetostriction [28]. The coupling mechanism is covered in depth in Section 3.1.

Receiver operation is possible via a reverse of the generation process. As the acoustic wave is generated electromagnetically, an EMAT only requires to be in close proximity to, and not in direct contact with the conductive surface. The magnitude of the fields induced in the surface and hence, the efficiency, is inversely proportional to the surface-transducer separation (liftoff). Any layer of non-conductive material placed between the transducer and surface can be treated purely as additional liftoff, making the transducer performance predictable. Exciting the wave directly into the wall avoids any problems arising due to poor impedance matching between couplant, coating and wall, as shown in Fig. 2.9c.

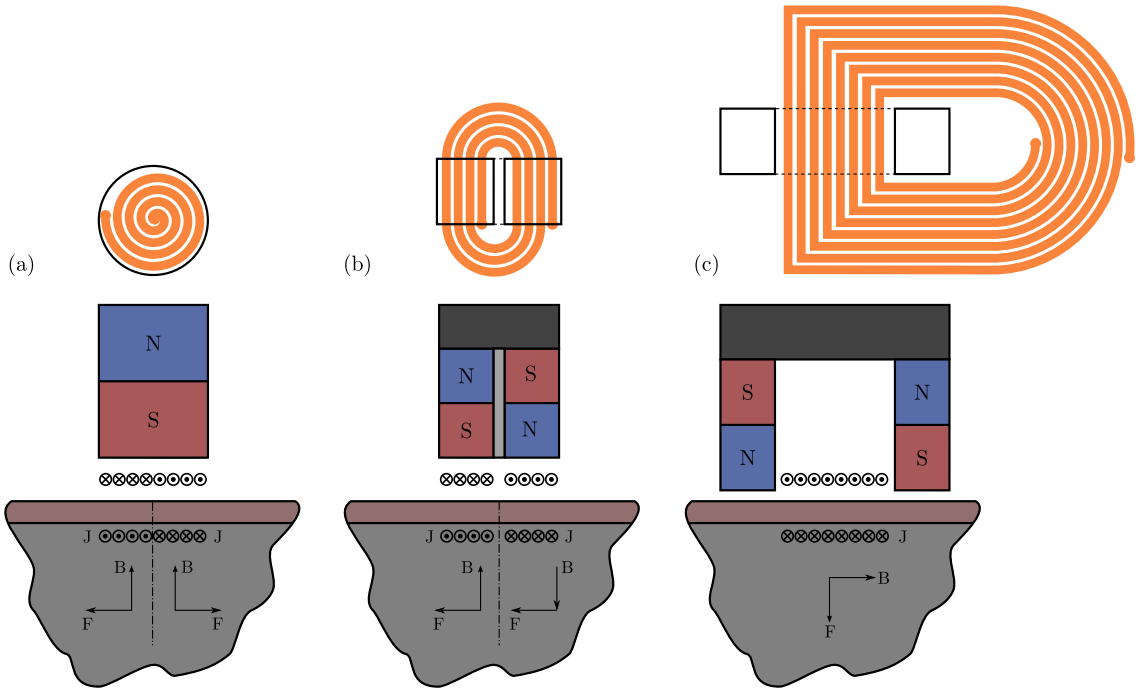

Figure 2.10: EMAT configurations generating normal propagating bulk waves. (a) Radially polarised shear, (b) parallel polarised shear, and (c) longitudinal.

2.3.4.2 EMAT Types

The wave mode generated by an EMAT is determined from the relative orientation of the coil and static magnetic field. Longitudinal, shear and surface waves are all possible which may propagate normal or parallel to the metal surface. A range of configurations, all of which generate normal propagating waves, are shown in Fig. 2.10. J, B and F indicate the directions of the eddy current density, magnetic flux density and Lorentz forces respectively. The direction indicated for the eddy current density and Lorentz force is valid during one half cycle of coil excitation. During the second half, the directions will reverse, generating wave motion.

2.3.4.3 Unique Properties

Although EMATs have been established since the 1960s, they are not widely used due to their relatively low efficiency; on an ideal surface, piezoelectrics will always have greater efficiency [29]. However, consistent performance irrespective of surface condition or coating is more beneficial for the development of a generic through metal communications system, rather than improved performance in idealised conditions. In fact, in some extreme cases, EMATs may be the only means of exciting ultrasound into the wall.

An added benefit when used on a ferrous metal wall is that the permanent magnet also serves as a mechanism for attaching the transducer; no adhesives or couplant allows for rapid deployment and removal. Some EMAT configurations, such as the radially polarised arrangement shown in Fig. 2.10a, can also be self attaching when used with non-ferrous materials. The static magnetic field can be polarised in either direction without affecting transduction. Hence, using opposite polarisations for transmit and receive EMATs causes the transducers to self align and clamp to the wall.

Due to the low efficiency of the transduction process, EMATs are not suitable for power transfer; only data communications.

2.4 Previous Systems

A limited number of studies have been performed on the subject of through metal communications and power transfer, the majority of which have occurred in parallel with the work presented in this thesis, which began in 2007. The following sections summarise and critically assess previous work and competing systems.

2.4.1 Piezoelectric Systems

2.4.1.1 Continuous Wave Power Delivery

Power delivery through a sealed armour using co-axially aligned piezoelectric transducers has been an area of interest for several research groups. Hu *et al.* (2001) (2003) [30, 31] first proposed the technique and presented a simplified theoretical model, which demonstrated efficient power transfer is possible by selecting an appropriate operational frequency and load, for a given wall geometry. Sherrit *et al.* (2006) [32] identified areas of the model in [31], which required further development for better representation of practical applications, namely thermal effects and bonding. Different means of bonding the piezoelectric crystal to an uncoated metal wall were then tested and demonstrated a wide variation in performance, with epoxy resin proving the most practical approach.

Following on from this, a series of prototypes for a 100W system were presented by Bao *et al.* (2007) [33]. 88% efficiency was achieved using 38mm diameter transducers, bonded to a 3.4mm thick titanium wall with epoxy. However, the wall sample used in this test was only marginally larger than the transducer diameter, which is not representative of the generalised metal wall case, which assumes infinite dimensions. The small sample prevents spreading loss and gives an artificially increased efficiency. A second set of prototypes were produced using larger plate samples and

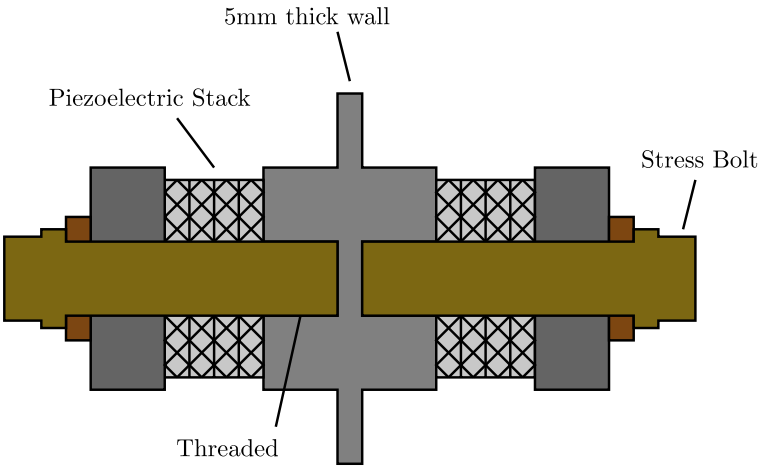

Figure 2.11: A 1kW wireless acoustic electric feed-through.

the best result demonstrated 40% efficiency. Another two prototypes gave ≈ 0% efficiency and this was accounted to inconsistency in the bond line, resulting from fabrication variables, such as surface finish, bond layer thickness and bond cure time and temperature.

Thermal effects were shown to be significant when transmitting at high power levels. Materials with low thermal conductivity, such as 316 stainless steel, are incapable of sufficiently dissipating heat in order to operate the system for prolonged periods.

Sherrit *et al.* (2008) [34] produced a 1kW system which requires no couplant and instead utilises a stress bolt to mechanically fix the device to a specially designed wall, as shown in Fig. 2.11. Efficiencies of 80-90% are quoted for 50.8mm transducers on a 5mm thick, 85mm diameter titanium plate. Modelling of the system on a larger, more realistic, plate demonstrated a 25% energy loss due to surface waves radiating from the active area. To compensate for this, further modification to the wall was proposed in the form of reflector rings, i.e. steel rings attached to the plate which encircle the transducers. The requirement for a metal channel with very specific properties makes the design highly impractical for a general purpose system.

Shoudy *et al.* (2007) [35] demonstrated ultrasonic power transfer on a considerably thicker sample, delivering 0.25W through 57mm of steel using 25.4mm transducers, illustrating the technique is not limited to thin wall channels. The efficiency of the system is not stated, only the output power, but is assumed to be relatively low due to the long transmission path.

Further theoretical modelling of the problem has been performed by Hu *et al.* [36] and Yang *et al.* [37–39]. In [38], it is shown it is possible to localise vibration in a plate in a process called ‘energy trapping’. Theoretically, with the selection of an

appropriate geometry, frequency and electrical load, a large portion of the energy can be confined to the transducer region, minimising unwanted vibration in the wall. This has not been utilised to date in a practical system.

Moss *et al.* (2008-2010) presented the development of an 'Acoustic Electric Feedthrough' (AEF) across several technical documents [40–43]. The final system utilises 10mm piezoelectric transducers bonded to a 1.6mm thick aluminium wall and has an efficiency of 43%.

All of the practical systems demonstrate a strong frequency dependence, with the quoted efficiencies being at a single optimal frequency. This agrees with the prediction of the original model [31]. Power transfer 'nulls' occur due to multipath induced fading as discussed in Section 2.3.1.5.

A consensus across the various systems indicates 40% efficiency is achievable through a large, thin ($<$ 5mm) metal wall. The bond line has been an area of interest of several studies and is shown to be critical to system performance. Eliminating the bond is only possible if the wall is specially designed to allowing mechanical mounting as demonstrated with stress bolts. It should be noted that *in each system, direct contact to a prepared metal surface is assumed, which does not account for a coating layer, which is almost guaranteed to have a detrimental effect on performance.*

2.4.1.2 Load Modulation

Many continuous wave power delivery systems also support data communications. These systems are always asymmetric and seek to minimise the power requirement of the 'inside' electronics shown in Fig. 2.2a. A solution, first proposed by Murphy (2005) [44], is to utilise load modulation. The amplitude of the reflected wave from the 'inside' wall-transducer interface is dependant on the impedance of the transducer as per (2.36). The 'inside' transducer can be switched to an open or short circuit state, to convey digital data to the 'outside' circuit. Saulnier *et al.* (2006) [45], Shoudy *et al.* (2007) [35] and Kluge *et al.* (2008) [46] have all utilised this technique.

The highest data rate is achieved in [35], with 55kbps through 57mm of material. The authors identify intersymbol interference as the prohibitive factor preventing higher data rates.

Murphy [44] proposed a variation, with a dedicated transmitter and receiver on the 'outside', to help improve the system signal to noise ratio. The three transducers are arranged as shown in Fig. 2.12. Saulnier *et al.* (2006) [45] achieved data rates approaching 500bps with this technique. Although the intention is to improve SNR, the effectiveness proves to be limited because the arrangement introduces additional

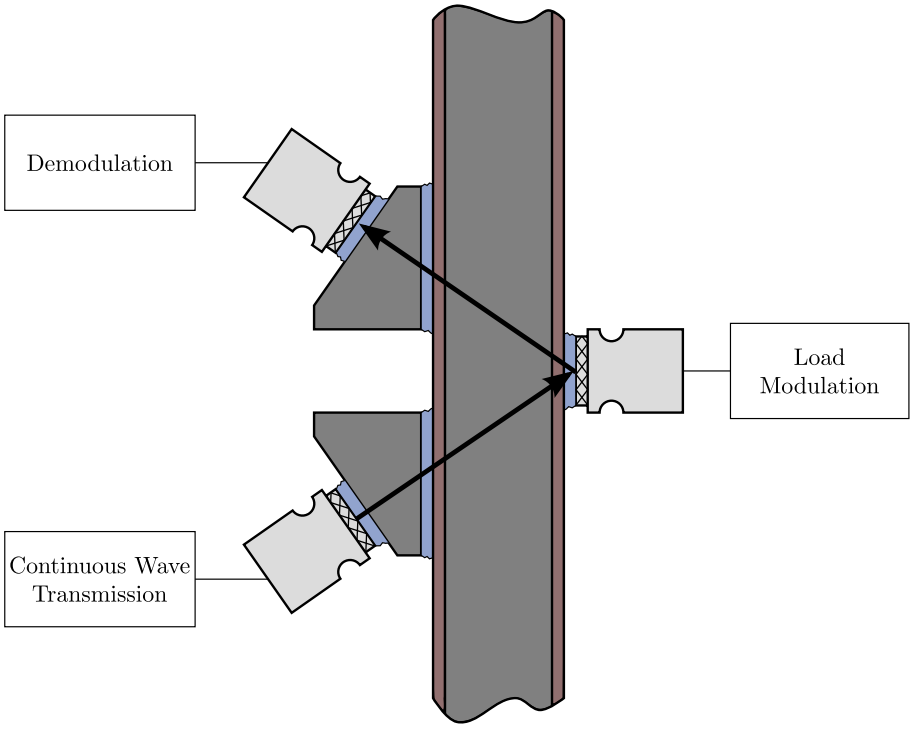

Figure 2.12: A load modulation scheme using a dedicated transmit and receive transducer, and angled wedges.

multipath. A piezoelectric crystal cannot produce an angled beam, so a wedge is required to interface the wall and transducer. This introduces extra bondlines, and additional multipath will result. Furthermore, the physical length of the direct transmission path is increased by a factor of $2/\cos\theta$, resulting in greater transmission losses.

2.4.1.3 Pre-distortion Filter

A high bit rate, half-duplex communications system is presented by Primerano *et al.* (2007) (2009) [15, 47] as a solution for scenario B, shown in Fig. 2.2b. Data is transmitted using pulse amplitude modulation (PAM), and to overcome acoustic multipath, a pre-distortion filter is implemented at the transmitting side, which calculates a cancelling pulse to be transmitted with each primary pulse. The net result is a significant reduction in the amplitude of multipath arrivals.

Filter tuning requires an estimation of two key system parameters: 1. The round trip delay of the acoustic signal, and 2. The rational function relating successive echoes. Estimation is performed on a received signal, which must then be conveyed to the transmitter. One option is to transmit this data, from receiver side to transmitter side, at a low data rate to avoid ISI. A second option is to design the system to

be able to switch transmit and receive circuitry fast enough to allow a pulse-echo training stage. To perform a successful estimation, the response of the channel must closely resemble the standard response for a metal wall multipath channel, as shown in Section 2.3.1.4. As shown later in Section 4.4.7, this response is not guaranteed, which limits the technique as a generalised solution.

Despite the shortcomings, the quoted data rate of 5Mbps is the highest to date reported in a technical paper, however, there is no indication of bit error rate (BER) performance. Tests were performed on a 6.35mm thick sample using 6.8MHz transducers.

2.4.1.4 BAE System

A patent filed by Bagshaw and Kent [48] describes an ultrasonic communications device designed specifically for 36mm submarine bulkheads. A high frequency (15-40MHz) continuous wave carrier is modulated to convey data at rates up to 15Mbps. Multipath is minimised by designing the system parameters for a specific wall geometry. With the appropriate selection of operational frequency, transducer diameter, electrical networks and couplant, the authors claim that reverberation is reduced to a sufficiently low level to enable continuous communication of data through the hull, at a bit rate of at least 1Mbps.

Designing for a specific case naturally makes the design difficult to migrate to a range of different applications. The high data rates are achieved due to the use of very high frequency transducers rather than efficient use of available bandwidth.

2.4.2 Inductive Systems

The magnetic field is used to convey power or data in many applications, such as induction motors, transformers or short range radio frequency identification (RFID) tags.

An inductive system will typically be designed to optimise a specific metric, such as maximum power delivery, alignment sensitivity or minimal coil dimensions. For an air channel, efficiencies up to 82% have been achieved at distances up to 15mm, using an operational frequency of 20kHz [49]. However, there have been no studies presented in technical journals attempting to optimise inductive power transfer through a metal wall channel.

2.4.2.1 HPRS

The hull penetrator replacement system (HPRS) is a system proposed by Jaskolski *et al.* [50] in a patent application for inductively transferring power and/or data through a metal wall. The design utilises two co-axially aligned, magnetically coupled solenoids. Asymmetric coils are claimed to result in improved results with a 33.8mm outer diameter (o.d.) transmitting coil (I = 25.4mm; N = 200 turns; 11.2mm core diameter) and an 11.9mm o.d. receiving coil (I = 15.2mm; N = 200 turns; 11.2mm core diameter), which is approximately a 3:1 ratio. The authors speculate this is due to the shape of the magnetic field.

Performance curves for the system, when tested on 22mm stainless steel and 3mm aluminium plate, demonstrate that signals above 20kHz are attenuated to undetectable levels. This low frequency severely limits the available bandwidth, meaning inductive methods will never be able to match the data rates achievable with an acoustic system, contrary to the author's claims. The power delivery capability of the system is not well defined, with no value given for power transfer efficiency or maximum transfer capability.

2.5 Summary

This chapter has introduced three transduction mechanisms, RF, acoustics and inductive coupling, and assessed each in terms of its suitability for through metal communications and/or power delivery. It has been shown conclusively that RF communications are not practical, primarily due to the extremely high reflection coefficient, but also due to skin effect losses. However, both acoustic and inductive techniques demonstrate attractive properties for the proposed application. A variety of transducers have been introduced for acoustic wave generation, yet a review of existing literature reveals that historically, piezoelectric contact transducers have been the unanimous choice. Piezoelectric transducers require good coupling to the surface and this cannot be achieved in many practical scenarios. EMATs have been identified as a novel non-contact alternative which overcome the coupling limitation and consequently, EMATs will be a key theme throughout this work. Regardless of the generation mechanism, the main challenges associated with acoustic techniques have been identified as multipath and ISI. Inductive techniques have not been explored previously in the context of through metal communications and power transfer but will be inherently limited by the properties of the metal wall. The relative merits of piezoelectric transducers, EMATs and inductive coupling are highlighted in Table 2.1 and previous/competing research is summarised in Table 2.2.

Table 2.1: Transducer comparison.

	Inductive	EMAT	Piezo
Mechanism	Magnetic	Acoustic	Acoustic
Multipath	**No**	Yes	Yes
Power Transfer	**Yes**	No	**Yes**
Coupling Reliance	**No**	**No**	Yes
Materials	Large δ	**Any**	**Any**

Table 2.2: Chronological summary of publications documenting through-metal communications and/or power transfer systems.

1st Author	Year	Bit Rate	Power Transfer		Thickness	Material	Comment
			Max.	Efficiency	(mm)		
Communications Systems							
Saulnier	2006	435bps	N/A	N/A	152.4	Steel	Very low data rate
Primerano	2007	1Mbps	N/A	N/A	6.35	Steel	Pre-distortion filter
Shoudy	2007	55kbps	0.25W	?	57	Steel	Reflected load modulation
Kluge	2008	1kbps	30mW	?	7	Aluminium	
Primerano	2009	5Mbps	N/A	N/A	6.35	Steel	High frequency transducers
Graham	2009	1Mbps	N/A	N/A	<80	HY-80 Steel	EMATs
Power Transfer Only							
Bao	2007	N/A	100W	40%	3.4	Titanium	Thermally limited
Sherrit	2008	N/A	1kW	80%	5	Titanium	Special fixing required
Moss	2010	N/A	3W	40%	1.6	Aluminium	Very Thin Wall

Chapter 3

EMAT Design

This chapter presents an in depth analysis of the Electromagnetic Acoustic Transducer (EMAT). An EMAT is a non-contact ultrasonic transducer consisting of a coil, to induce electromagnetic fields in the surface of a conductive material, and at least one magnet to provide a biasing magnetic field [28, 51]. The field orientation determines the direction of propagation and mode of the generated elastic waves [52]. Unique properties of the transducer were introduced in Section 2.3.4; the key advantage being *the ability to induce sound, directly into a conductive surface, through both an air gap and non-conductive surface coating.* This unique property is highly desirable for a practical through metal communications system, yet the EMAT has not previously been considered for this application.

In the following sections, the coupling mechanism is analysed to explain the acoustic wave generation mechanism of an EMAT, with the aid of the current theoretical model. Consideration is given to the circuitry required for driving an EMAT and also for receiving signals. Finally, the performance of an EMAT prototype is experimentally characterised with varying amounts of transducer-wall separation (liftoff).

3.1 EMAT coupling mechanism

The processes by which an electromagnetic acoustic transducer generates mechanical waves in a conductive material are known collectively as the coupling mechanism. Previous studies have shown there to be three contributing mechanisms [28, 53–55]:

i. Lorentz force

ii. Magnetization force

iii. Magnetostriction

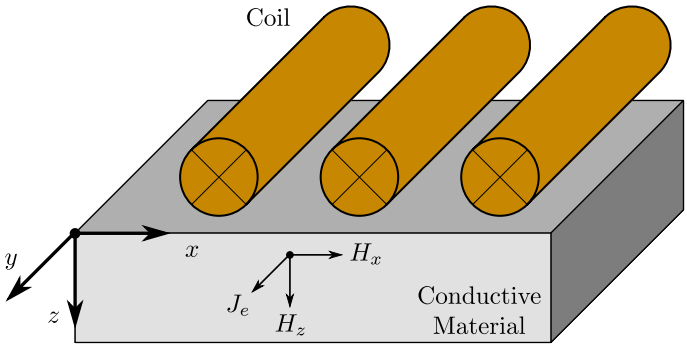

Figure 3.1: A section of a unidirectional coil, with N turns per unit length, above a conductive material.

When a material is non-ferromagnetic, the Lorentz force mechanism completely describes the interaction between the electromagnetic and elastic fields. However, when a material is ferromagnetic, all three mechanisms contribute.

3.1.1 Model

Modelling the EMAT coupling mechanism is a complex problem, as it requires interdisciplinary understanding of the interaction between electromagnetic and acoustic fields. Sections 3.1.2, 3.1.3 and 3.1.4 provide an overview of the most recent work in the field and rely heavily on the work of Hirao and Ogi [28, 53].

To simplify the complexity of the analysis, several approximations are necessary.

i. The electromagnetic fields are two dimensional variables in the x-z plane shown in Fig. 3.1.

ii. Magnetostriction results in no volume change (i.e. the material is an isovolume).

iii. Quantities with a subscript 0, e.g. H_{0z}, are time independent. Time-dependent variables, e.g. H_x, oscillate with the factor $e^{j\omega t}$, but this term is omitted.

The coil shown in Fig. 3.1, generates a dynamic magnetic field when excited with a current. The initial stage of the analysis is to quantify the behaviour of this dynamic field within the material. It was originally shown by Thompson [54] that the dominant component, H_x, decays exponentially in the material depending on the skin depth, δ, where, N is the number of turns per unit length and I is the excitation current (3.1). Skin depth is a function of angular frequency, ω, conductivity, σ, and permeability, μ (3.2).

Table 3.1: Direction of Lorentz force due the orientation of the static magnetic field.

J	**B**	$\mathbf{f}^{(L)}$
$+y \odot$	$+z \downarrow$	$+x \rightarrow$
$+y \odot$	$+x \rightarrow$	$-z \uparrow$

$$H_x = \frac{NI}{2} e^{-\frac{z}{\delta}} e^{-j\frac{z}{\delta}} \tag{3.1}$$

$$\delta = \sqrt{\frac{2}{\omega\sigma\mu}} \tag{3.2}$$

The orientation of the coil, relative to the surface, means it is possible to determine the relative amplitudes of the rate of change of the field components in the x and z directions (3.3) [28].

$$\left|\frac{\partial H_x}{\partial z}\right| \gg \left|\frac{\partial H_x}{\partial x}\right| \approx \left|\frac{\partial H_z}{\partial z}\right| \gg \left|\frac{\partial H_z}{\partial x}\right| \tag{3.3}$$

3.1.2 Lorentz force

A point charge will experience a force due to the presence of an electromagnetic field. The strength and direction of the force is described by the Lorentz force law. For an eddy current density, $\mathbf{J}_e$, this force is described by (3.4).

$$\mathbf{f}^{(L)} = \mathbf{J}_e \times \mathbf{B}_0 \tag{3.4}$$

The Maxwell−Ampere equation can be used to determine the free current, $\mathbf{J}_f$, and displacement current $\frac{\partial \mathbf{D}}{\partial t}$ associated with a given magnetic field, $\mathbf{H}$.

$$\mathbf{J}_f + \frac{\partial \mathbf{D}}{\partial t} = \nabla \times \mathbf{H} \tag{3.5}$$

For the configuration shown in Fig. 3.1, $\mathbf{J}_e$ only has a component in the y-direction. Due to the low megahertz operating frequencies typically used with EMATs, the displacement current term, $\frac{\partial \mathbf{D}}{\partial t}$, can be ignored, which simplifies the Maxwell−Ampere equation to (3.6).

$$\mathbf{J}_f = \mathbf{J}_e = J_y = \frac{\partial H_x}{\partial z} - \frac{\partial H_z}{\partial x} \tag{3.6}$$

The second term is negligible due to (3.3) and hence, the Lorentz forces can be expressed as (3.7) . Table 3.1 shows the direction of the Lorentz force for two

different orientations of the static magnetic field. The force, $f_x^{(L)}$, will generate a shear wave and requires a static magnetic field oriented perpendicular to the conductive surface. Conversely, $f_z^{(L)}$, will generate a longitudinal wave and requires a static magnetic field parallel to the surface.

$$\begin{cases} f_x^{(L)} = B_{0z}\dfrac{\partial H_x}{\partial z} \\ f_z^{(L)} = -B_{0x}\dfrac{\partial H_x}{\partial z} \end{cases} \tag{3.7}$$

For non-ferromagnetic materials, the Lorentz force is the sole EMAT generation mechanism. However, when a material is ferromagnetic, additional forces arise which must also be considered.

3.1.3 Magnetization force

A magnetized body will tend to rotate to align the magnetization with an applied field, giving rise to the magnetization force described in (3.8), which may be expanded as shown in (3.9) [4].

$$\mathbf{f}^{(M)} = \mathbf{M} \cdot \nabla \mathbf{H} \tag{3.8}$$

$$\begin{cases} f_x^{(M)} = M_{0x}\dfrac{\partial H_x}{\partial x} + M_{0z}\dfrac{\partial H_z}{\partial x} \\ f_z^{(M)} = M_{0x}\dfrac{\partial H_x}{\partial z} + M_{0z}\dfrac{\partial H_z}{\partial z} \end{cases} \tag{3.9}$$

The second force terms in (3.9) are insignificant, relative to the first terms, due to (3.3). If the Lorentz forces are combined with magnetization forces (3.10) (3.11), the negative sign of $f_z^{(L)}$ becomes significant; $f_z^{(M)}$ and $f_z^{(L)}$ act in opposite directions and partially cancel, making Lorentz and magnetization mechanisms ineffective at generating longitudinal-mode waves in ferromagnetic materials.

$$f_x^{(M)} + f_x^{(L)} = B_{0z}\frac{\partial H_x}{\partial z} + M_{0x}\frac{\partial H_x}{\partial x} \tag{3.10}$$

$$f_z^{(M)} + f_z^{(L)} = (M_{0x} - B_{0x})\frac{\partial H_x}{\partial z} = -\mu_0 H_{0x}\frac{\partial H_x}{\partial z} \tag{3.11}$$

3.1.4 Magnetostriction

Magnetostriction is the change in the physical dimensions of a magnetic material due to a change in magnetization. In the presence of a magnetic field, randomly

oriented magnetic domains align along the total magnetic field, resulting in mechanical strains. When the magnetic field is time-varying, these strains generate acoustic waves [56].

To analyse magnetostrictive effects it is assumed the coupling between magnetic and elastic fields takes a similar form to that of piezoelectric crystal (3.12) [28].

$$\mathbf{T} = \mathbf{c}^H\mathbf{S} - \mathbf{e}^{(\mathrm{MS})}\mathbf{H} \tag{3.12}$$

$$\mathbf{e}^{(\mathrm{MS})} = \mathbf{c}^H\mathbf{d} = \frac{\partial \mathbf{T}^{(\mathrm{MS})}}{\partial \mathbf{H}} \tag{3.13}$$

$$\mathbf{d} = \frac{\partial \mathbf{S}}{\partial \mathbf{H}} \tag{3.14}$$

where,
$\mathbf{T}$ is the stress tensor
$\mathbf{c}^H$ is the stiffness tensor
$\mathbf{S}$ is the strain tensor
$\mathbf{e}^{(\mathrm{MS})}$ are converse piezomagnetic stress coefficients
$\mathbf{H}$ is the magnetic field
$\mathbf{d}$ are piezomagnetic strain coefficients

If the dynamic field oscillates at high frequency, the strain cannot respond simultaneously, resulting in the magnetostriction stress, $\mathbf{T}^{(\mathrm{MS})}$ (3.15), which may be expanded as shown in (3.16).

$$\mathbf{T}^{(\mathrm{MS})} = -\mathbf{e}^{(\mathrm{MS})}\mathbf{H} \tag{3.15}$$

$$\begin{bmatrix} T_1^{(\mathrm{MS})} \\ T_2^{(\mathrm{MS})} \\ \vdots \\ T_6^{(\mathrm{MS})} \end{bmatrix} = \begin{bmatrix} c_{11} & c_{12} & \cdots & c_{16} \\ c_{21} & c_{22} & \cdots & c_{26} \\ \vdots & \vdots & \ddots & \vdots \\ c_{61} & \cdots & \cdots & c_{66} \end{bmatrix} \begin{bmatrix} d_{1x} & d_{1y} & d_{1z} \\ d_{2x} & d_{2y} & d_{2z} \\ \vdots & \ddots & \vdots \\ d_{6x} & d_{6y} & d_{6z} \end{bmatrix} \begin{bmatrix} H_x \\ H_y \\ H_z \end{bmatrix} \tag{3.16}$$

To simplify (3.16), Voigt notation has been used, which arises due to symmetry of the stress tensor (3.17).

$$\begin{aligned}\mathbf{T} &= \begin{bmatrix} T_{xx}^{(\mathrm{MS})} & T_{yy}^{(\mathrm{MS})} & T_{zz}^{(\mathrm{MS})} & T_{yz}^{(\mathrm{MS})} & T_{xz}^{(\mathrm{MS})} & T_{xy}^{(\mathrm{MS})} \end{bmatrix}^{\mathbf{T}} \\ &= \begin{bmatrix} T_{1}^{(\mathrm{MS})} & T_{2}^{(\mathrm{MS})} & T_{3}^{(\mathrm{MS})} & T_{4}^{(\mathrm{MS})} & T_{5}^{(\mathrm{MS})} & T_{6}^{(\mathrm{MS})} \end{bmatrix}^{\mathbf{T}} \end{aligned} \tag{3.17}$$

$$\text{where,} \quad T_{ij} = T_{ji} \qquad (i, j = x, y, z \,\text{and}\, i \neq j)$$

The magnetostrictive forces are obtained from the divergence of the stress tensor (3.18).

$$\nabla \cdot \mathbf{T}^{(\mathrm{MS})} = \begin{cases} f_x^{(\mathrm{MS})} = \dfrac{\partial T_1^{(\mathrm{MS})}}{\partial x} + \dfrac{\partial T_6^{(\mathrm{MS})}}{\partial y} + \dfrac{\partial T_5^{(\mathrm{MS})}}{\partial z} \\ f_y^{(\mathrm{MS})} = \dfrac{\partial T_6^{(\mathrm{MS})}}{\partial x} + \dfrac{\partial T_2^{(\mathrm{MS})}}{\partial y} + \dfrac{\partial T_4^{(\mathrm{MS})}}{\partial z} \\ f_z^{(\mathrm{MS})} = \dfrac{\partial T_5^{(\mathrm{MS})}}{\partial x} + \dfrac{\partial T_4^{(\mathrm{MS})}}{\partial y} + \dfrac{\partial T_3^{(\mathrm{MS})}}{\partial z} \end{cases} \tag{3.18}$$

To determine the magnetostrictive forces, the elements of the stress tensor must be evaluated from (3.16). The elastic stiffness coefficients are a property of the material, whilst the piezomagnetic strain coefficients, $\mathbf{d}$, are unknown. Hence, knowledge of the piezomagnetic strain coefficients, $\mathbf{d}$, allows for the evaluation of the magnetostriction forces.

3.1.4.1 Piezomagnetic Strain Coefficient Calculation

For this analysis, the medium is assumed to be isotropic cubic (e.g. iron) hence the elastic stiffness coefficients, $\mathbf{c}$, take the form given in (3.19). It is also assumed that the bias field is normal to the surface i.e. $\mathbf{H}_0 = (0, 0, H_{0z})$.

$$\mathbf{c} = \begin{bmatrix} c_{11} & c_{12} & c_{12} & 0 & 0 & 0 \\ c_{12} & c_{11} & c_{12} & 0 & 0 & 0 \\ c_{12} & c_{12} & c_{11} & 0 & 0 & 0 \\ 0 & 0 & 0 & c_{44} & 0 & 0 \\ 0 & 0 & 0 & 0 & c_{44} & 0 \\ 0 & 0 & 0 & 0 & 0 & c_{44} \end{bmatrix} \tag{3.19}$$

The static field, H_{0z}, produces static positive magnetostriction $\epsilon\,(H_{0z})$. Assuming the strain acts upon an infinitesimal isovolume element, then this also produces magnetostriction perpendicular to the field which can be approximated as $-\frac{1}{2}\epsilon\,(H_{0z})$ as shown in Fig. 3.2. The static strain field, $\mathbf{S}^0$, resulting from $\mathbf{H}_0$ is given in (3.20) [28].

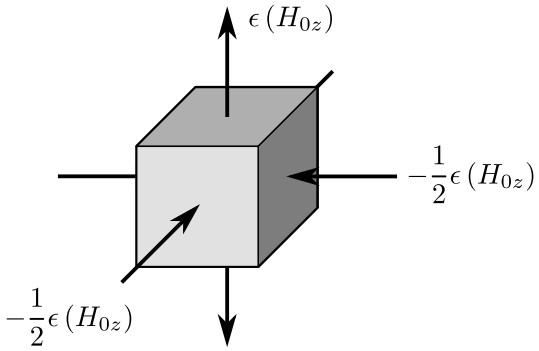

Figure 3.2: Strain on an infinitesimal isovolume element due to the static field H_{0z}.

$$S_3^0 = \epsilon\,(H_{0z})\,, \qquad S_1^0 = S_2^0 = -\frac{1}{2}\epsilon\,(H_{0z}) \qquad S_4^0 = S_5^0 = S_6^0 = 0 \tag{3.20}$$

The dynamic field component, H_z, disturbs the static field, resulting in dynamic strain, $\mathbf{S}$. If $H_z \ll H_{0z}$ then the dynamic strain components can be approximated to (3.21) [28].

$$S_3 = \left(\frac{\partial S_3}{\partial H_z}\right) H_z, \qquad S_1 = S_2 = -\frac{1}{2}\left(\frac{\partial S_3}{\partial H_z}\right) H_z, \qquad S_4 = S_5 = S_6 = 0 \tag{3.21}$$

The first of the piezomagnetic strain coefficients can now be determined, which relate strain to the dynamic field component, H_z, and this is equivalent to the gradient of the magnetostriction curve, γ. A magnetostriction curve is a plot of mechanical strain against magnetic field and can be obtained experimentally for any given material. A complete magnetostriction curve demonstrates that most materials exhibit highly non-linear behaviour. However, because an EMAT superimposes a small dynamic field on a much larger static field there is only a small oscillation of the magnetic field around the operation point, such that a linear assumption is locally valid. An in-depth discussion, as well several magnetostriction curve examples are given by Ribichini *et al.* [56]. Hence, the piezomagnetic strain coefficients relating to the z-component of the dynamic magnetic field may be expressed as given in (3.22) [28].

$$d_{3z} = \left(\frac{\partial S_3}{\partial H_z}\right) \equiv \gamma, \qquad d_{1z} = d_{2z} = -\frac{1}{2}\gamma, \qquad d_{4z} = d_{5z} = d_{6z} = 0 \tag{3.22}$$

Calculation of the piezomagnetic strain components due to the x-component of the dynamic field, H_x, is considerably more complex. The dynamic component H_x

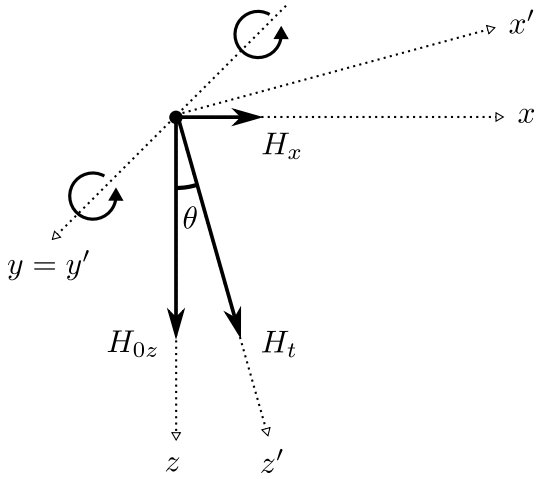

Figure 3.3: The dynamic component, H_x, superimposes with the static field, H_{0z}, producing a resultant total field, H_t.

produces a resultant field, H_t, which is rotated by an angle, θ, about the y axis. The resultant field now lies on the z' axis resulting in the magnetostriction, $\epsilon\left(H_t\right)$, and the perpendicular magnetostriction is in the x' direction and y direction, as shown in Fig. 3.3. This results in the inclined strain field, $\mathbf{S}'$ given in (3.23) [28].

$$S_3^{'} = \epsilon\left(H_t\right) \equiv \epsilon_t, \qquad S_1^{'} = S_2^{'} = -\frac{1}{2}\epsilon\left(H_t\right) = -\frac{1}{2}\epsilon_t \tag{3.23}$$

The inclined coordinate system must be converted back to the original coordinate system to determine the piezomagnetic strain coefficients, which are relative to the original x and z axes. This is achieved using the rotational matrix coordinate transform given in (3.24).

$$\begin{bmatrix} S_1 \\ S_3 \\ S_5 \end{bmatrix} = \begin{bmatrix} \cos^2\theta & \sin^2\theta & 2\sin\theta\cos\theta \\ \sin^2\theta & \cos^2\theta & -2\sin\theta\cos\theta \\ -\sin\theta\cos\theta & \sin\theta\cos\theta & \cos^2\theta - \sin^2\theta \end{bmatrix} \begin{bmatrix} S_1^{'} \\ S_3^{'} \\ S_5^{'} \end{bmatrix} \tag{3.24}$$

Transforming (3.23) using (3.24) produces the strain elements given in (3.25). There are no shearing deformations in the $x^{'}, y^{'}, z^{'}$ coordinate system, hence, $S_5^{'} = 0$. Also S_2 remains unchanged as this is in the direction of the axis of rotation (y direction).

$$\begin{cases} S_1 = S_1^{'}\cos^2\theta + S_3^{'}\sin^2\theta \\ S_2 = S_2^{'} \\ S_3 = S_3^{'}\cos^2\theta + S_1^{'}\sin^2\theta \\ S_5 = \left(S_3^{'} - S_1^{'}\right)\sin 2\theta \end{cases} \tag{3.25}$$

The piezomagnetic strain coefficients describing the strain field due to dynamic field component H_x can be calculated by evaluating (3.14), i.e. differentiating each of the strain components with respect to H_x. The calculation can be performed using the product rule and the identities given in (3.26). The calculated piezomagnetic strain coefficients are given in (3.27) [28].

$$\begin{aligned}\theta =& \tan^{-1}\left(\frac{H_x}{H_{0z}}\right)\\ \frac{\partial\theta}{\partial H_x} =& \frac{1}{H_{0z}\left(\frac{H_x^2}{H_{0z}^2}+1\right)} = \frac{\cos^2\theta}{H_{0z}}\\ \frac{\partial\epsilon_t}{\partial H_x} =& \gamma\sin\theta\end{aligned} \tag{3.26}$$

$$\begin{cases} d_{1x} = \dfrac{\partial S_1}{\partial H_x} = \dfrac{\partial}{\partial H_x}\left(-\dfrac{1}{2}\epsilon_t\cos^2\theta + \epsilon_t\sin^2\theta\right) \\ \qquad = \dfrac{3\epsilon_t}{H_{0z}}\cos^3\theta\sin\theta + \gamma\sin\theta\left(-\dfrac{1}{2}\cos^2\theta + \sin^2\theta\right) \\ d_{2x} = \dfrac{\partial S_2}{\partial H_x} = \dfrac{\partial}{\partial H_x}\left(-\dfrac{1}{2}\epsilon_t\right) \\ \qquad = -\dfrac{\gamma}{2}\sin\theta \\ d_{3x} = \dfrac{\partial S_3}{\partial H_x} = \dfrac{\partial}{\partial H_x}\left(\epsilon_t\cos^2\theta + -\dfrac{1}{2}\epsilon_t\sin^2\theta\right) \\ \qquad = -\dfrac{3\epsilon_t}{H_{0z}}\cos^3\theta\sin\theta + \gamma\sin\theta\left(-\dfrac{1}{2}\sin^2\theta + \cos^2\theta\right) \\ d_{5x} = \dfrac{\partial S_5}{\partial H_x} = \dfrac{\partial}{\partial H_x}\left(\dfrac{3}{2}\epsilon_t\sin 2\theta\right) \\ \qquad = \dfrac{3\gamma}{2}\sin 2\theta\sin\theta + \dfrac{3\epsilon_t}{H_{0z}}\cos^2\theta\cos 2\theta \end{cases} \tag{3.27}$$

Coefficients for the dynamic component, H_y, can be calculated using the same methodology, where H_y produces a total field rotated about the x axis (3.28).

$$\left\{ d_{1y} = d_{2x},\, d_{2y} = d_{1x},\, d_{3y} = d_{3x},\, d_{4y} = d_{5x},\, d_{5y} = 0,\, d_{6y} = 0 \right. \tag{3.28}$$

It is a fair assumption that the static field, H_{0z}, is much greater than any component of the dynamic field, hence, it is clear that the angle of inclination will be small. In which case, the coefficients can be further approximated (3.29).

$$\lim_{\theta\to 0}\left\{ d_{4y} = d_{5x} = \frac{3\epsilon_t}{H_{0z}}, d_{1z} = d_{2z} = -\frac{\gamma}{2}, d_{3z} = \gamma, \text{otherwise} = 0 \right. \tag{3.29}$$

The complete set of piezomagnetic strain coefficients may now be expressed in vector form. Similarily, the converse piezomagnetic stress coefficients, $\mathbf{e}$, may be evaluated from (3.13) and (3.19). Both $\mathbf{d}$ and $\mathbf{e}$ are given in (3.30) [28].

$$\therefore \quad \mathbf{d} = \begin{bmatrix} 0 & 0 & -\frac{\gamma}{2} \\ 0 & 0 & -\frac{\gamma}{2} \\ 0 & 0 & \gamma \\ 0 & \frac{3\epsilon_t}{H_{0z}} & 0 \\ \frac{3\epsilon_t}{H_{0z}} & 0 & 0 \\ 0 & 0 & 0 \end{bmatrix}, \qquad \mathbf{e} = \begin{bmatrix} 0 & 0 & \frac{\gamma}{2}(c_{12}-c_{11}) \\ 0 & 0 & \frac{\gamma}{2}(c_{12}-c_{11}) \\ 0 & 0 & \gamma\,(c_{11}-c_{12}) \\ 0 & \frac{3\epsilon_t c_{44}}{H_{0z}} & 0 \\ \frac{3\epsilon_t c_{44}}{H_{0z}} & 0 & 0 \\ 0 & 0 & 0 \end{bmatrix} \tag{3.30}$$

Finally, the two dimensional magnetostrictive forces, $f_x^{(\mathrm{MS})}$ and $f_z^{(\mathrm{MS})}$, can be determined using the definition of the forces (3.18), the definition of the stress components (3.16), the definition of the converse piezomagnetic strain components (3.13) and the calculated coefficients (3.30). The expressions describing the forces are given in (3.31).

$$\begin{cases} f_x^{(\mathrm{MS})} = \dfrac{\partial T_1^{(\mathrm{MS})}}{\partial x} + \dfrac{\partial T_5^{(\mathrm{MS})}}{\partial z} = -\dfrac{3\epsilon_t c_{44}}{H_{0z}}\dfrac{\partial H_x}{\partial z} + \dfrac{\gamma}{2}\left(c_{11}-c_{12}\right)\dfrac{\partial H_z}{\partial x} \\ f_z^{(\mathrm{MS})} = \dfrac{\partial T_5^{(\mathrm{MS})}}{\partial x} + \dfrac{\partial T_3^{(\mathrm{MS})}}{\partial z} = -\dfrac{3\epsilon_t c_{44}}{H_{0z}}\dfrac{\partial H_x}{\partial x} - \gamma\left(c_{11}-c_{12}\right)\dfrac{\partial H_z}{\partial z} \end{cases} \tag{3.31}$$

Using (3.3) it is immediately obvious that $f_x^{(\mathrm{MS})} \gg f_z^{(\mathrm{MS})}$, hence, the magnetostrictive forces resulting from a normal bias field produce shear waves far more efficiently than longitudinal waves. Furthermore, it is now possible to compare the magnitude of the shear forces generated by Lorentz and magnetostrictive mechanisms (3.32). Again, using (3.3) it is possible to ignore the second term of $f_x^{(\mathrm{MS})}$.

$$\begin{aligned} \frac{f_x^{(\mathrm{MS})}}{f_x^{(\mathrm{L})}} &= \frac{-\frac{3\epsilon_t c_{44}}{H_{0z}}\frac{\partial H_x}{\partial z}}{B_{0z}\frac{\partial H_x}{\partial z}} \\ &= -\frac{3\epsilon_t c_{44} B_{0z}}{H_{0z}} \end{aligned} \tag{3.32}$$

Using values for a typical steel [28], $H_{0z} = 5 \times 10^3$ A/m, $c_{44} = 80$ GPa, $B_{0z} = 1$T, $\epsilon_t = 2 \times 10^{-6}$ then the magnitude of the magnetostrictive force can be shown to be 100 times greater than that of the Lorentz force (3.33).

$$\left| \frac{f_x^{(\mathrm{MS})}}{f_x^{(\mathrm{L})}} \right| \approx 100 \tag{3.33}$$

3.2 EMAT Configuration

The analytic model of the coupling mechanism presented in the previous section helps identify key points useful in the design of practical transducers:

i. The Lorentz force is the sole mechanism for non-ferromagnetic materials.

ii. For ferromagnetic materials such as steel, magnetostrictive forces are dominant.

iii. Magnetostrictive forces generate shear waves far more efficiently than longitudinal waves.

On the basis of these findings, it is apparent that for effective operation on both ferromagnetic and non-ferromagnetic materials, the EMAT should be of shear wave type. The selected EMAT configuration generates radially polarised shear waves and is shown in Fig. 3.4. The transducer consists of a single cylindrical magnet and a pancake coil. Fig. 3.4 shows the magnet dimensions, which determines the approximate dimensions of the complete transducer. A magnet with a smaller axial dimension may be used to minimise the profile of the transducer but will reduce the magnetic field strength and resultant efficiency.

Neodymium-Iron-Boron (NdFeB) permanent magnets are preferred to electromagnets for reasons of power efficiency and provide a higher flux density than any other permanent magnet type at room temperature [57]. For high temperature applications ($> 150°$C), Samarium Cobalt (SmCo) magnets are preferred and can be used at temperatures in excess of 300°C [58].

3.3 Coil Design

The operational centre frequency of an EMAT is set by capacitively tuning the coil. Selecting the centre frequency for a through metal communications system is a trade off; higher frequencies offer greater bandwidth, but at the expense of greater transmission losses. Due to the low efficiency already associated with the transduction process, lower frequencies are preferred to maximise the system signal to noise ratio. However, lower frequencies limit the minimum wall thickness before intrasymbol interference occurs due to multipath propagation. Intrasymbol interference is avoided if (3.34) is satisfied; if it is assumed that most practical applications will involve steel structures with a wall thickness, $z_{\text{wall}} > 5$mm, and a shear wave velocity, $c_s \approx 3200\text{ms}^{-1}$, the bandwidth requirement of the system is 320kHz. As shown later, EMAT coils have a low quality factor, Q, typically 2-3 at minimum

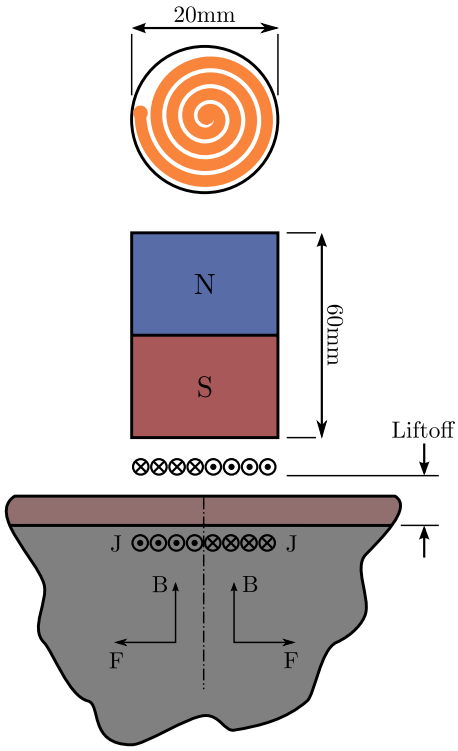

Figure 3.4: Radially-polarised shear wave EMAT configuration showing approximate transducer dimensions. Note: Coil not to scale.

liftoff, hence from (3.35), a centre frequency, f_c, of the order of 1MHz is required. A centre frequency of 1.04166MHz was ultimately selected for practical reasons. As shown later in Section 5.6, this is the closest frequency to 1MHz achievable with the selected transmitter hardware for high bit rate transmissions.

$$\frac{1}{\Delta f} < \frac{2z_{\text{wall}}}{c_s} \tag{3.34}$$

$$\Delta f = \frac{f_c}{Q} \tag{3.35}$$

To maximise the efficiency of the system, individual consideration must be given to the electrical properties of the EMAT coils for transmitting and receiving. The desired coil properties are contrasting and hence, a significant performance gain can be achieved by optimising the Tx and Rx EMATs accordingly.

The coil equivalent circuits are shown in Fig. 3.5. In order to deliver maximum power to the transmit coil, its impedance should be low to match the low output impedance of a power amplifier. By series tuning, the circuit will experience an impedance minimum at the desired resonant frequency, f_c, as per (3.36), where L is the coil inductance and C is the tuning capacitance.

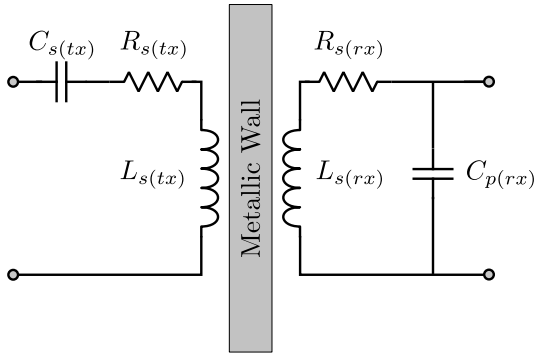

Figure 3.5: Coil equivalent circuits.

$$f_c = \frac{1}{2\pi\sqrt{LC}} \tag{3.36}$$

From (3.35), it can be seen that in order to maximise bandwidth, Δf, it is important that the Q factor of the coil is kept relatively low. For a series tuned circuit, the Q factor is determined from (3.37), where R_s, L_s and C_s are the series resistance, inductance and capacitance respectively.

$$Q = \frac{1}{R_s}\sqrt{\frac{L_s}{C_s}} \tag{3.37}$$

Due to the size constraint imposed by the available magnets (20mm diameter), the transmitter design resulted in an 18mm diameter printed circuit board (PCB) coil with 19 turns. In proximity to an HY80 steel sample, the properties of the coil are $L_s = 1.25\mu$H and $R_s = 3.3\Omega$ at a 1.04166MHz test frequency. From these values, the Tx coil has a theoretical bandwidth of approximately 420 kHz.

Generating maximum voltage across the receive coil requires high impedance, which implies parallel tuning and many turns. The Q factor for a parallel tuned circuit is determined from (3.38), however, the values of R_s and L_s must first be transformed to their parallel equivalents as per (3.39) and (3.40).

$$Q = R_p\sqrt{\frac{C_p}{L_p}} \tag{3.38}$$

$$R_p = \frac{{R_s}^2 + (\omega L_s)^2}{R_s} \tag{3.39}$$

$$L_p = \frac{{R_s}^2 + (\omega L_s)^2}{\omega^2 L_s} \tag{3.40}$$

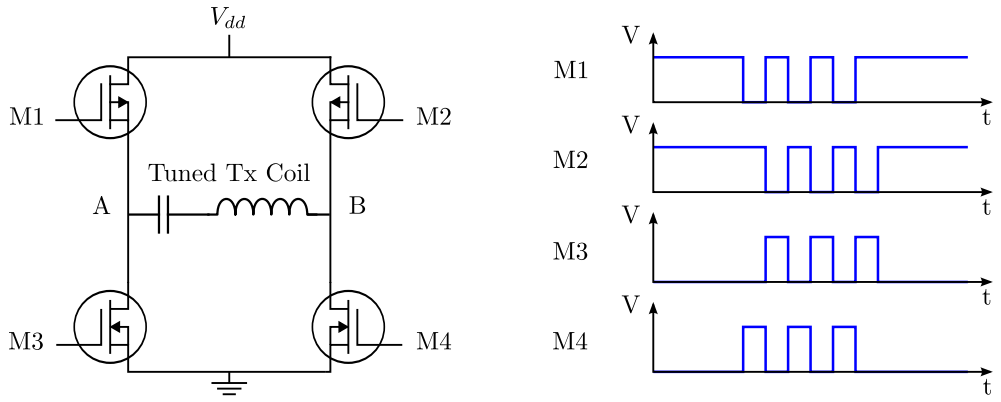

Figure 3.6: H-Bridge topology and accompanying control signals for a 3 cycle pulse, assuming p-type high side MOSFETs. Points A and B are the measurement points used to observe the transmit waveform in Section 5.6.

Based on these equations, an 18mm receive coil was produced from SWG 40 enamelled wire with 300 turns. The properties of which, are $L_s = 157\mu$H and $R_s = 490\Omega$, at a 1.04166MHz test frequency. The resultant theoretical bandwidth is therefore 490kHz.

3.4 Supporting Electronics

3.4.1 Transmit Circuitry

A simple, low cost and versatile power amplifier is the class-D amplifier, which can be realised with an H-Bridge arrangement of MOSFETs, as shown in Fig. 3.6. Control signals can be generated from any low cost microcontroller or field programmable gate array (FPGA). To achieve the high switching speeds required for ultrasonic transducers, a MOSFET gate driver is necessary on each of the control signal lines [59]. The disadvantage of a class-D amplifier is that it is non-linear and hence cannot generate accurate amplitude modulated signals. The design of a linear class-A amplifier for an EMAT transmitter would be more complex, particularly with regard component specification. Furthermore, the inherent inefficiency of a class-A design is far from ideal for a transducer which is known to already suffer from relatively low efficiency. Consequently, a linear amplifier is not considered in this thesis.

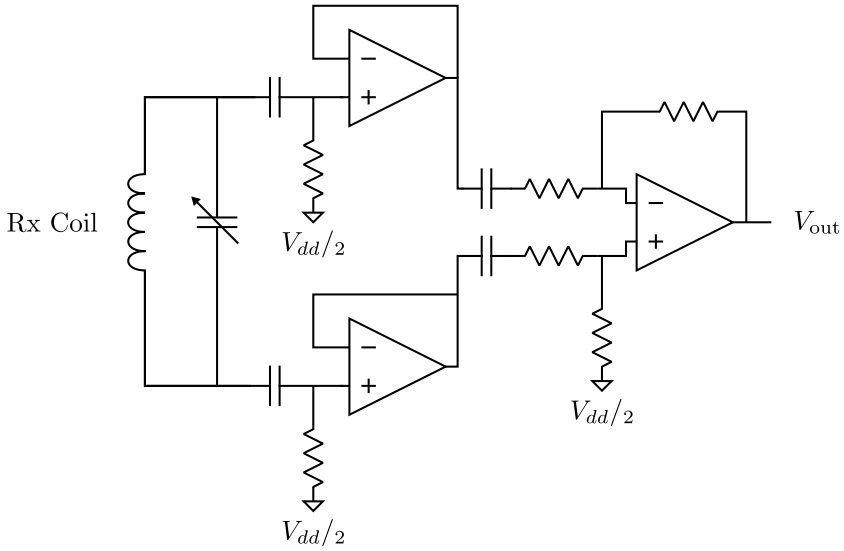

Figure 3.7: Instrumentation amplifier topology.

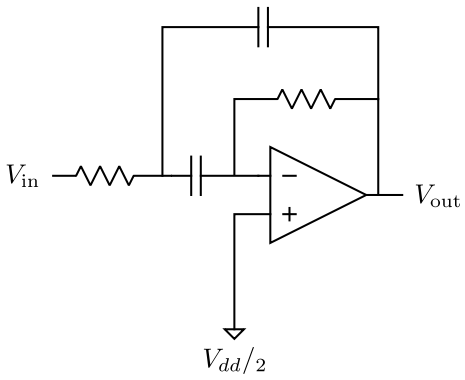

Figure 3.8: Multiple feedback bandpass (MFB) filter topology.

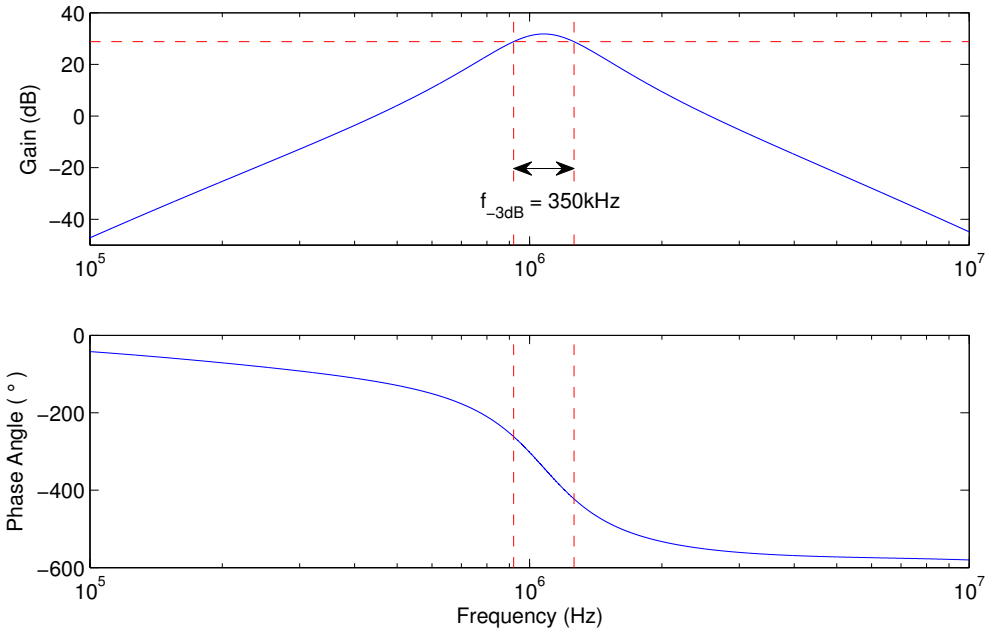

Figure 3.9: Frequency response of the EMAT pre-amplifier circuit.

3.4.2 Receive Circuitry

As stated previously, the relative transduction efficiency of an EMAT is low and SNR is at a premium, hence, the design of the analogue pre-amplifier circuitry is very important for any EMAT based system. A gain of 30-40dB is required, depending on the specifics of the application, whilst maintaining system bandwidth and filter stability.

For the first stage of the receiver, the instrumentation amplifier topology offers excellent characteristics including, low noise, very high common-mode rejection ratio and very high input impedance. Signal conditioning can then be performed by successive single ended gain/filtering stages. These topologies are shown in Fig. 3.7 and Fig. 3.8.

Early experimentation highlighted stability problems and oscillation with cascaded single pole bandpass topologies at the required gain level. However, the multiple feedback bandpass (MFB) filter was found to have excellent stability, although at the expense of a small amount of bandwidth. The filter response is shown in Fig. 3.9 demonstrating a gain of 32dB with a centre frequency of 1.050MHz and 350kHz of bandwidth. Ideally, the pre-amplifier should be designed with 400kHz of bandwidth to better match the transducers, hence, this is an obvious area for improvement, but careful design is required to maintain stability. High bandwidth, low noise operational amplifiers are essential to the design.

3.5 Liftoff Performance

EMATs are non-contact transducers and can operate with varying amounts of liftoff [60]. However, it is important to appreciate that the performance and properties of the transducer do not remain constant. The following section serves to quantify the performance penalty associated with liftoff.

Using an Agilent E4980A LCR bridge, the electrical properties of the transmit and receive EMAT coils were measured on an HY80 steel plate, with liftoff ranging from 0.8mm to 10.4mm, and the results are shown in Fig. 3.10. For practical implementation, 0.8mm represents the smallest possible wall-coil liftoff after accounting for surface coating and transducer packaging.

At small liftoff, the eddy current density in the metal is at its maximum. The magnetic field generated by the eddy currents opposes the generating field according to Lenz's law and lowers the coil inductance. Similarly, the AC resistance increases, due to proximity effect. The overall outcome is a lower Q factor at small liftoff and significantly increased bandwidth.

With a nominal liftoff of 0.8mm, the bandwidth of the transmit and receive coils are reasonably well matched. At larger standoffs, the bandwidth of the transmit coil tails off faster than that of the receive coil and, beyond 1.6mm, the transmit coil becomes the bandwidth bottleneck of the system, rather than the receiver preamplifier.

A second test was performed to measure the variation in signal to noise ratio with liftoff. A 6 cycle pulse was transmitted through an HY80 steel plate and the received signal strength was recorded with liftoff ranging from 0.8mm to 7.2mm. The results are presented in Fig. 3.11, demonstrating a 3.7dB loss per millimetre of liftoff. Small deviations from the line of best fit are due to unavoidable slight variations in transducer alignment during the experimental procedure.

3.6 Directivity

The transmit and receive transducers require near co-axial alignment for successful operation. When performing 'blind' installation, i.e. the wall prevents alignment by eye or mechanical means, perfect alignment cannot be guaranteed. The system beam pattern describes the directivity of the system, and determines the performance penalty associated with misalignment.

The system beam pattern was determined experimentally on a 25.4mm HY80 steel plate. This thickness represents the focal length of a 1MHz, 18mm transducer with a wave propagation speed of 3200ms^{-1} from (2.39). The position of the transmitter

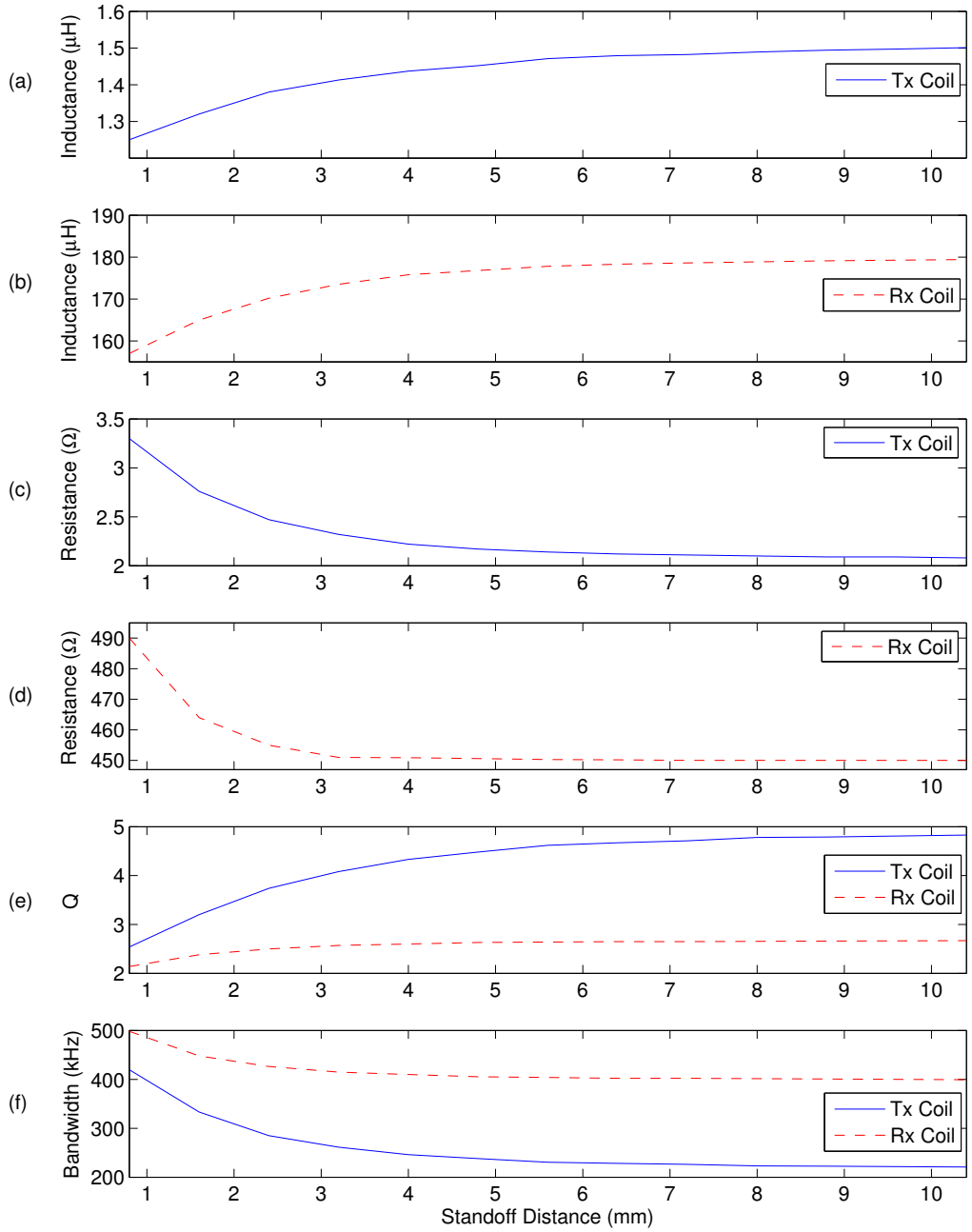

Figure 3.10: Tx and Rx EMAT coil properties at various liftoff distances, obtained through experimental measurement. (a) Tx coil inductance. (b) Rx coil inductance. (c) Tx coil resistance. (d) Rx coil resistance. (e) Q factor. (f) Bandwidth.

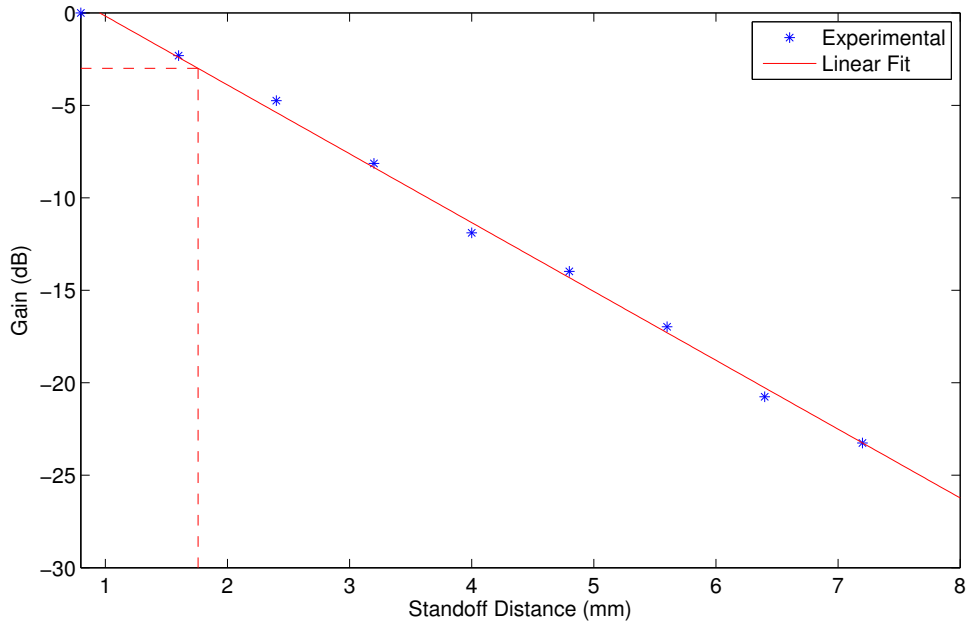

Figure 3.11: Variation in system signal to noise ratio due to receive EMAT liftoff.

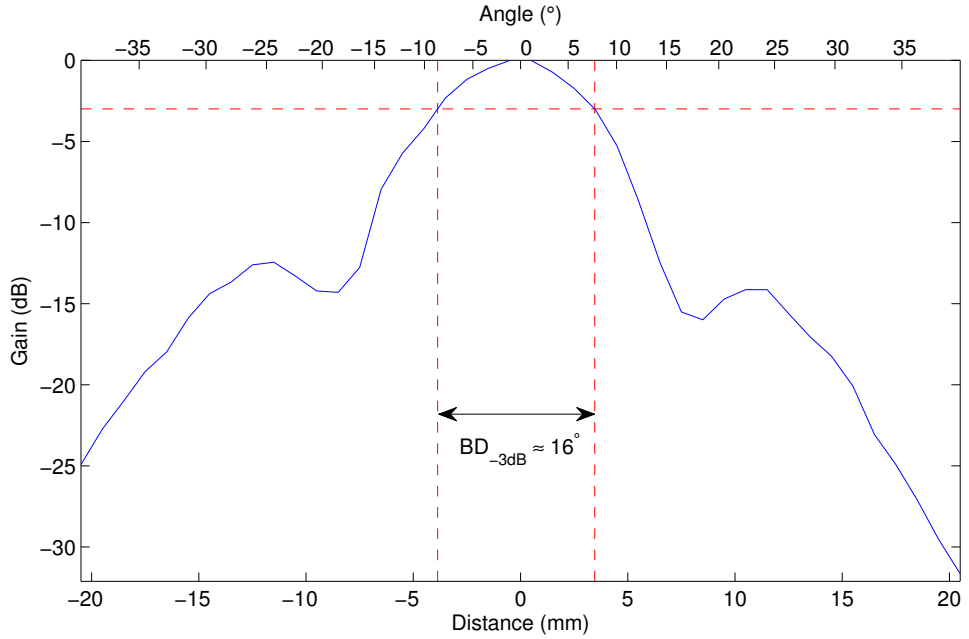

Figure 3.12: EMAT beam pattern determined from the corresponding change in received acoustic power due to a varying degree of transducer misalignment.

is moved in 1mm steps and the amplitude of the received signal is recorded. The result is shown in Fig. 3.12, demonstrating a 3dB beamwidth $\approx 16°$. For a 25.4mm wall, this translates to a 7mm diameter target area in which the central axis of one EMAT must be placed, relative to the central axis of the other. In practice, alignment to within a few millimetres is easily achievable.

A slight asymmetry in the beam pattern is to be expected due to the natural asymmetry of a spiral coil. By strict definition, the obtained plot is not a true beam pattern as the distance from transmitter to receiver cannot be kept constant. Signals can only be transmitted and received at the surface of the material and hence, the distance between the transducer centres increases with offset. However, for the purpose of through metal communications, it is a more accurate performance metric.

3.7 Summary

This chapter has provided an overview of the three EMAT generation mechanisms; Lorentz force, magnetising force and magnetostriction. It has been shown that the Lorentz force is the sole mechanism for non-ferrous materials and that magnetostrictive forces are dominant for ferrous materials. Designs for an EMAT transmitter and receiver have been presented based around the radially polarised shear wave configuration. The resulting system is inherently broadband but has relatively low SNR. Experimentation has been performed to characterise EMAT performance and it has been demonstrated that acoustic wave generation is possible with many millimetres of liftoff, an ideal property for reliable transmission through surface coatings, such as paint.

Chapter 4

Burst Mode Transmission

In this chapter, the design and testing of a complete acoustic through metal communications system is discussed. For sensor applications, with low to moderate data output, the key design metric is not raw throughput, but rather minimal power and hardware requirements. These constraints prevent the use of complex modulation schemes or receiver structures to overcome the inherent multipath in a metal wall channel. Burst mode modulation schemes are presented, which are multipath tolerant, whilst not requiring high speed computation or specialist hardware.

A demonstrator system is presented which was designed as a solution for scenario B; enabling data communications between metallic walled compartments, such as those formed by the internal bulkheads of a naval vessel. To add further constraint to the design, it was assumed the system is for temporary/retro fit and should act as an enabling technology for a wireless sensor network. This intended application helps provide a basis of understanding for many of the choices made during the design of the demonstrator system. However, it should be noted that the fundamental principal of operation of the communication mechanism could be applied to any problem involving a metal wall channel.

Other aspects of an acoustic communications system are also discussed, including the acoustic protocol, the system algorithm and means of minimising power consumption. Finally, results are presented from field testing at BAE Systems, Barrow-in-Furness.

4.1 Channel Impulse Response

In order to design a system to overcome or tolerate multipath, it is important to have knowledge of the multipath delay spread. As discussed in Section 2.3.1.4, this can be visualised from the channel impulse response (IR) and key parameters, such as significant multipath duration, can be determined.

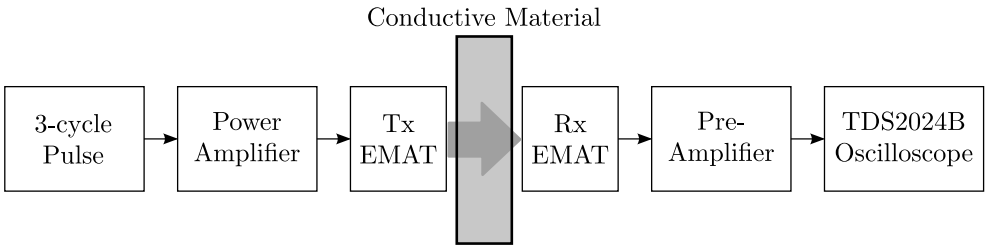

Figure 4.1: Experimental setup to determine the channel impulse response of an EMAT based system.

4.1.1 IR Setup

The impulse response can be obtained experimentally using the setup shown in Fig. 4.1. Transmit and receive EMATs are aligned co-axially on a block of conductive material. A 3-cycle, logic level pulse is generated on a microcontroller and amplified to drive the Tx EMAT. The direct path acoustic pulse and subsequent multipath arrivals are received on an Rx EMAT, amplified, and the result is captured on a digital oscilloscope. An analogous setup can be used to determine the impulse response with piezoelectric transducers.

4.1.2 Test Blocks

The large faces of the metallic blocks used for laboratory testing are machined flat and are uncoated. Machining the faces serves to minimise scattering and produce a worst case multipath scenario. Polystyrene sheet or similar material is used to apply a controlled thickness liftoff to simulate a surface coating. A standard 0.8mm is used for most tests, which is an appropriate thickness to allow for most practical coatings.

For the purpose of this thesis, it is assumed that the metallic wall, for which the system is intended, has infinite dimensions in the x-y plane. In other words, no additional multipath should originate from side wall reflections. For practical tests, this implies using very large test blocks, which are difficult to source, store and to manoeuvre. An attractive alternative is to use smaller, 150mm $\times$ 150mm test blocks, and modify them to minimise the amplitude of any side wall reflection. If a surface is rough or textured, it will cause an acoustic wave to scatter upon reflection. To be effective, the textured features should be larger than the acoustic wavelength. For a shear wave propagating in steel, this translates to features >3mm. The texture shown in Fig. 4.2 is applied to the four side-walls of the test blocks. The pattern

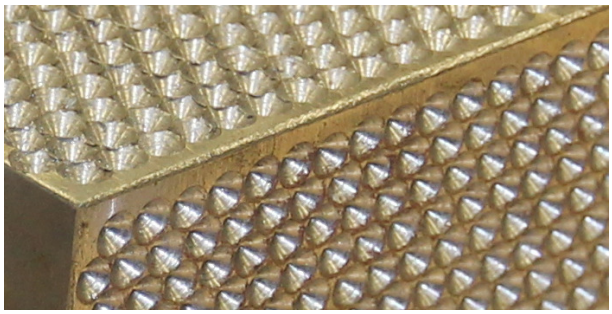

Figure 4.2: Anechoic pattern drilled into the side walls of metallic test blocks with the purpose of minimising unrealistic multipath emanating from side wall reflections.

consists of a repeating conical pattern formed by a drill point, with 4mm between hole centres.

4.1.3 IR Results and Discussion

The channel impulse response of 12.7mm and 25.4mm thick HY80 steel plates are shown in Fig. 4.3, for both EMATs and piezoelectric transducers. Each response exhibits the key features of the generic impulse response introduced in Section 2.3.1.4. Ultrasound excited in the wall reflects at the wall-air (EMAT) or wall-couplant (Piezo) boundaries due to an impedance mismatch, resulting in reverberations. The primary arrival is received after a time, T_w, determined by the thickness of the material and the speed of sound, and subsequent smaller reflections arrive after intervals of $2T_w$. It should be noted that the transmit power is not kept constant during each test and instead, it is adjusted such that primary arrival is approximately 4V peak to peak. This approach allows for direct comparison of the multipath response in each test.

The amplitude decay of the multipath is contrasting for piezoelectric transducers and EMATs on a common test block due to differing boundary and transmission losses. The significant multipath duration associated with piezoelectrics is far shorter than that of an EMAT based system. Boundary losses are different for piezoelectrics and EMATs, due to their contrasting contact and non-contact natures. The reflection coefficients can be calculated from (2.36). Assuming that the acoustic impedances of air, steel and couplant are $430\,\mathrm{kgm^{-2}s^{-1}}$, $4.7 \times 10^7\,\mathrm{kgm^{-2}s^{-1}}$ and $2.5 \times 10^6\,\mathrm{kgm^{-2}s^{-1}}$ [15] respectively, a steel-couplant boundary has a reflection coefficient of 0.88, whereas a steel-air boundary has a reflection coefficient of 0.9999. However, for the special case of a shear wave EMAT with a steel-air interface, the reflection coefficient is 1 as a shear wave cannot propagate in a fluid [61].

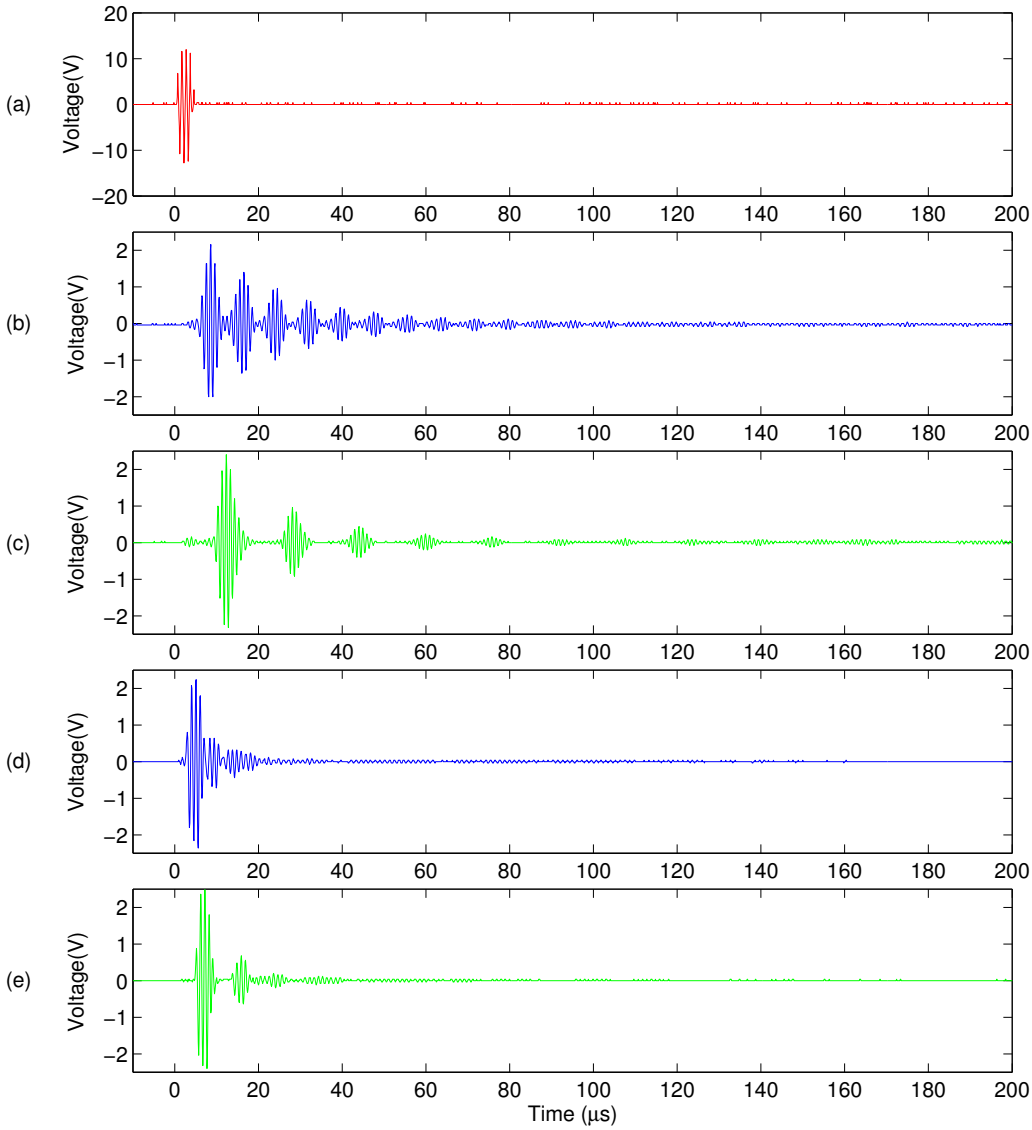

Figure 4.3: Channel impulse response comparison. (a) 3-cycle transmit pulse. (b) EMAT on 12.7mm HY80. (c) EMAT on 25.4mm HY80. (d) Piezoelectric on 12.7mm HY80. (e) Piezoelectric on 25.4mm HY80.

Transmission loss is a function of distance, hence, the velocity of the wave determines the magnitude of loss in a unit time period. As longitudinal waves travel at almost twice the speed of shear waves in metals, the rate of loss associated with piezoelectrics is twice that of EMATs. The combination of a higher reflection coefficient and slower propagation speed results in a considerably longer multipath delay spread with EMATs, as can be seen by comparing Fig. 4.3b and d, or c and e.

As the wall thickness reduces, the frequency of reflections increases, which can be seen by comparing Fig. 4.3b and c, or d and e. The boundary loss associated with piezoelectric transducers means the multipath duration also decreases (Fig. 4.3d and e), however, this is not the case for EMATs (Fig. 4.3b and c). For a smooth faced wall, total reflection occurs at the boundary, hence, multipath duration remains constant. For thicker walls, the multipath becomes increasingly sparse (Fig. 4.3c).

With the aid of signal averaging, a small signal can be seen between the expected multipath arrivals in Fig. 4.3c. This may be a result of the EMAT also generating a very small amplitude longitudinal wave component. This is possible due to the curvature of the magnetic field at the EMAT coil extremities. The longitudinal wave amplitude is significantly smaller than the shear wave amplitude and will decay significantly faster, such that it may be ignored.

For a fairer comparison between piezoelectrics and EMATs it could be argued that a common wave mode should be used for both transducers. However, shear wave piezoelectric transducers require bonding to a surface due to the inefficiency associated with transmission through a viscous couplant [62]. This makes shear wave piezos highly impractical when it is desirable to perform experiments on a succession of test blocks with the same transducer. Conversely, longitudinal wave generation using EMATs is highly inefficient. Hence, the results presented represent a comparison of the best available piezoelectric transducer and the best available EMAT.

4.1.3.1 Cross-talk

A small signal can be seen arriving before the primary acoustic arrival in Fig. 4.3c. In fact, it is present in all four impulse response results but it is difficult to distinguish when the time of flight of the primary acoustic arrival is less than the pulse width. As this erroneous signal occurs almost simultaneously in time with the transmit pulse, it is clearly not acoustic in nature; it must be electromagnetic.

Cross-talk can result from non-idealities in the experimental setup. The use of plate material, rather than a complete sealed enclosure results in an air path between transmitter and receiver. Furthermore, ground loops can result from improper grounding of transducer casings, circuitry or equipment. Ensuring a good common ground between equipment and the metal plate is typically good enough to reduce

cross-talk to minimal levels. Cross-talk is only a concern during experimental testing as an electromagnetic path cannot exist in a practical application.

4.1.3.2 Time Variability

For most common applications, it is fair to assume that a metal wall channel is quasi-static, as the impulse response can change over time, however, the rate of change should be sufficiently slow, such that the channel may be considered static over the duration of a data packet transmission. The most likely source of variation is a change in temperature or mechanical stress, which has a direct influence on the speed of sound in metal, which subsequently determines the position and separation of the direct and multipath arrivals.

Nowacki and Kasprzyk [63] have demonstrated a $> 2\%$ reduction in the velocity of a transverse wave in some steels from $20°C - 94°C$, and a $> 6\%$ reduction from $20°C - 400°C$. It is fair to assume given the limited number of metals tested that this does not represent a worst case. Temperature variation could become important for oil and gas or chemical processing applications.

Drescher-Krasicka and Willis [64] and Landa and Plesek [65] have studied acoustic propagation for the purpose of measuring stress within solids. It has been shown that the variation is typically $< 1\%$ even when materials are stressed until they yield.

Other processes, such as corrosion, may also slowly alter the impulse response but any ageing of the material will take place over a very large time period and will not be considered within the scope of this work.

4.1.4 Guard Interval

Burst mode transmission is a mode of operation where time diversity is employed to achieve reliable communications in a multipath channel. The technique has previously been applied to the underwater acoustic channel, where strong multipath originates from sea floor and surface reflections [66, 67].

Due to the quasi-static nature of the multipath in a metal wall channel, it is possible to apply time diversity to prevent or minimise ISI. Time diversity is inherently simple to implement and hence, provides the basis for a low cost, low power, low complexity solution.

The general principal of burst mode operation is to introduce a guard interval after each symbol transmission where no transmissions shall occur, the duration of which, can be determined from the channel impulse response. A symbol may be conveyed

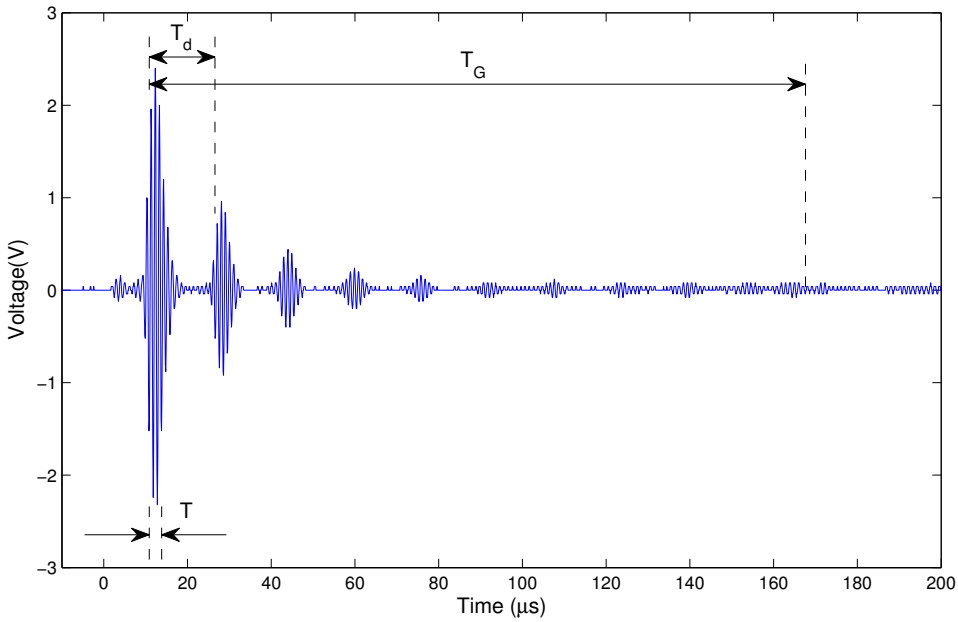

Figure 4.4: Key impulse response parameters for implementing burst mode transmission. T denotes the symbol duration, T_d denotes the duration until the start of the first multipath arrival and T_G denotes the duration until the start of the last multipath arrival.

using any modulation scheme but due to the nature of the multipath response or hardware requirements, some schemes become more favourable.

Each data symbol consists of a pulse, followed by a guard interval. Information may be conveyed by modulating the pulse amplitude (pulse amplitude modulation/PAM), duration (pulse width modulation/PWM), or position (pulse position modulation/PPM).

Pulse amplitude modulation is very simple to implement with two signalling levels, on or off. However, binary signalling limits the system to 1-bit per symbol, which ultimately limits the maximum data throughput. Increasing the modulation order requires a means of outputting intermediate amplitude level pulses, which requires additional hardware in the form of a linear power amplifier to drive the transmit transducer.

Pulse width modulation is the least attractive of the aforementioned modulation schemes as the same level of performance cannot be maintained across a range of wall thicknesses. The minimum available pulse width is limited by the bandwidth, Δf, of the system, which was shown to be 350kHz in Section 3.4.2. Hence, 3 cycles are required at 1MHz to reach maximum amplitude (4.1).

$$T = \frac{1}{\Delta f} \tag{4.1}$$

The pulse width determines the symbol time, T, which is indicated on Fig. 4.4. The maximum pulse width is limited by the duration until the first reflection, T_d ,which is determined from the thickness of the wall and speed of propagation. Hence, as the wall thickness reduces, a smaller range of pulse widths are available for encoding data, whereas ideally, the solution should be insensitive to wall thickness.

Pulse position modulation uses constant amplitude and constant pulse width, requiring only timers to encode and decode data, making it a preferred scheme for a low cost implementation.

4.2 Pulse Position Modulation

Pulse position modulation (PPM) is a digital pulse code modulation scheme whereby, n bits are encoded into a single pulse occupying one of $\mathrm{M} = 2^n$ time slots, where M is referred to as the modulation order. PPM is often utilised in optical communications, as it is a very attractive technique for both the optical fibre and ideal photon counting channels [68, 69].

Fig. 4.5a shows M-PPM graphically, for the case $\mathrm{M} = 4$, where T_c is the chip duration and P_t is the average transmit power of the scheme. Each time frame consists of 1 'on' chip and M-1 'off' chips.

A derivative of PPM is Differential-PPM (DPPM), which has improved average-power efficiency and no requirement for symbol synchronisation. DPPM symbols remove the redundant 'off' chips following the 'on' chip as shown in Fig. 4.5b.

The M-DPPM symbol set, $S_n(t)$, $0 \leq n \leq \mathrm{M} - 1$, is expressed formally in (4.2), where P_c is the peak transmit power. A comparison of the bit mappings of the two schemes is shown in Table 4.1.

$$S_n(t) = \begin{cases} 0 & t < nT_c \\ P_c & nT_c \leq t \leq (n+1)\,T_c \end{cases} \tag{4.2}$$

A complication introduced by DPPM is that the symbol duration is no longer constant and as a result, nor is the data rate. The mean data rate, $\overline{f_b}$, is only achieved if a packet contains an equal number of each symbol (4.3). The upper bound, f_{bu}, is achieved if a packet consists solely of the shortest symbol (4.4), and the lower bound, f_{bl}, results from a packet consisting solely of the longest symbol (4.5).

Table 4.1: Example source bit mappings for 4-PPM and 4-DPPM.

Source Bits	Corresponding 4-PPM chips	Corresponding 4-DPPM chips	Reverse 4-DPPM chips
00	1000	1	0001
01	0100	01	001
10	0010	001	01
11	0001	0001	1

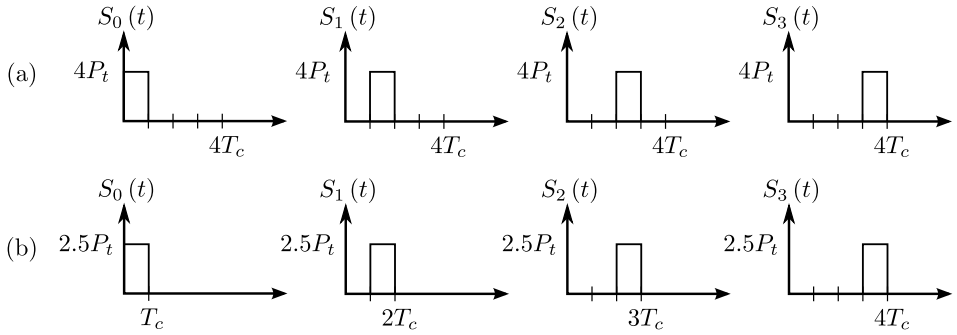

Figure 4.5: 'On' and 'off' chips for the symbol set comprising: (a) 4-PPM, (b) 4-DPPM. T_c is the chip duration and P_t is the average transmit power of the scheme.

$$\overline{f_b} = \frac{2\log_2 \mathrm{M}}{(\mathrm{M}+1)\,T_c} \tag{4.3}$$

$$f_{bu} = \frac{(\mathrm{M}+1)\,\overline{f_b}}{2} \tag{4.4}$$

$$f_{bl} = \frac{(\mathrm{M}+1)\,\overline{f_b}}{2\mathrm{M}} \tag{4.5}$$

An attractive solution to maximise throughput, proposed by Shiu and Khan [69], exploits the fact that bit mappings may be assigned arbitrarily. The data packet to be sent can be analysed and it can be determined if this will result in a packet longer than the mean length. In which case, the mappings may be inverted to give the 'reverse' mapping, an example of which is shown in Table 4.1. An extra flag bit is then required to indicate to the receiver which mappings to use to decode the packet. Using this methodology, the mean data rate becomes the guaranteed worst case throughput. Alternative methods, such as randomisation with a pseudo-random number sequence (PN code), could also be employed to achieve a near consistent data rate.

Introducing a guard period, T_G, to encompass the multipath response of the channel has a direct influence on the achievable data rate. The mean, upper and lower

bounds become (4.6), (4.7) and (4.8) respectively.

$$\overline{f_b} = \frac{2\log_2 \mathrm{M}}{(\mathrm{M}+1)\,T_c + 2T_G} \tag{4.6}$$

$$f_{bu} = \frac{\log_2 \mathrm{M}}{T_c + T_G} \tag{4.7}$$

$$f_{bl} = \frac{\log_2 \mathrm{M}}{\mathrm{M}T_c + T_G} \tag{4.8}$$

4.3 Multi-symbol Burst Mode Transmission

Pulsed modulation schemes, as introduced previously, transmit a single symbol per burst before a guard interval allows the multipath to decay. For thicker walls, the time period until the first multipath arrival, T_d, is considerably larger than a symbol period, T (Fig. 4.4). In this situation, n symbols may be transmitted in a single burst up to the limit of (4.9).

$$nT \leq T_d \tag{4.9}$$

For bursts consisting of multiple symbols, it is preferable to transmit using a continuous wave scheme such as phase shift keying (PSK). The data rate of the scheme, f_{bm}, can be calculated using (4.10).

$$f_{bm} = \frac{nT}{T_G + nT} B \log_2 \mathrm{M} \tag{4.10}$$

If the symbol period, T, is equivalent to the chip period, T_c, as in the pulse position scheme, and $n = 1$, then it can be shown that the bit rate of the system is equal to the upper data rate limit of the DPPM system, f_{bu}. This is an intuitive result as a single symbol burst is equivalent to shortest DPPM symbol. Consequently, multi-symbol burst mode transmission will always achieve a greater throughput than an equivalent PPM system under identical channel conditions. The trade-off is the increased hardware requirements associated with modulating and demodulating PSK bursts.

Maximum throughput is achieved when the channel exhibits a single stationary multipath and the data rate becomes (4.11). Hence, an EMAT based system with $\Delta f = 350\text{kHz}$ can achieve upto 350kbps using QPSK.

$$f_{bm} = \frac{1}{2} B \log_2 \mathrm{M} \qquad (nT = T_d = T_G) \tag{4.11}$$

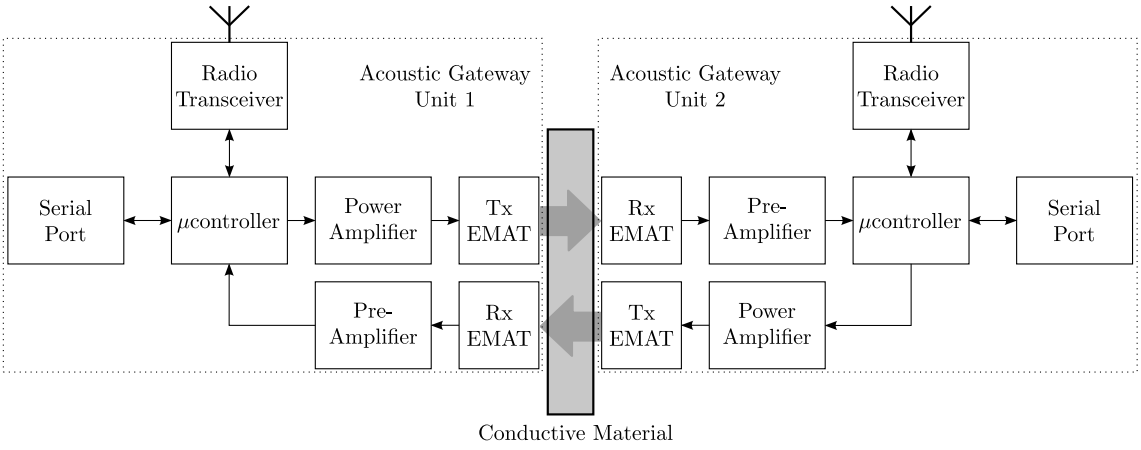

Figure 4.6: System level diagram of the acoustic gateway demonstrator.

4.4 Acoustic Gateway Demonstrator System

A demonstrator system was a key requirement of the project sponsors, BAE Systems, to allow any proposed techniques to be evaluated in real world situations. A system level diagram is shown in Fig. 4.6, highlighting the key elements of the demonstrator system, coined the 'acoustic gateway'.

Each gateway consists of two units, which must be reasonably well aligned, either side of a metal wall. A data packet may be input into either side of the gateway via the RS-232 serial port or an IEEE 802.15.4 radio transceiver. The microcontroller encodes the data into an acoustic data packet which is then transmitted via the Tx EMAT. The acoustic transmission is received via the Rx EMAT, on the other side of the wall, and, after analogue detection, it is decoded by the microcontroller. The packet is then output via the serial port or the radio transceiver.

4.4.1 Hardware Construction

An external view of the acoustic gateway is shown in Fig. 4.7 indicating key features. A gateway unit is housed in a die cast aluminium enclosure, which has a wall footprint measuring approximately 150mm×150mm, with a depth approx 75mm. The top side of a unit has three connectors, one for observing acoustic transmissions, one for observing the acoustic receiver output and one for the serial port interface. Also located on this face are the RF antenna and mode select switch, which is used in conjunction with the acoustic signal monitoring connections to install the device. The only notable feature of the front face is a multi-way selector switch to increase the acoustic transmit power for thicker walls. On the back face, the transmit coil

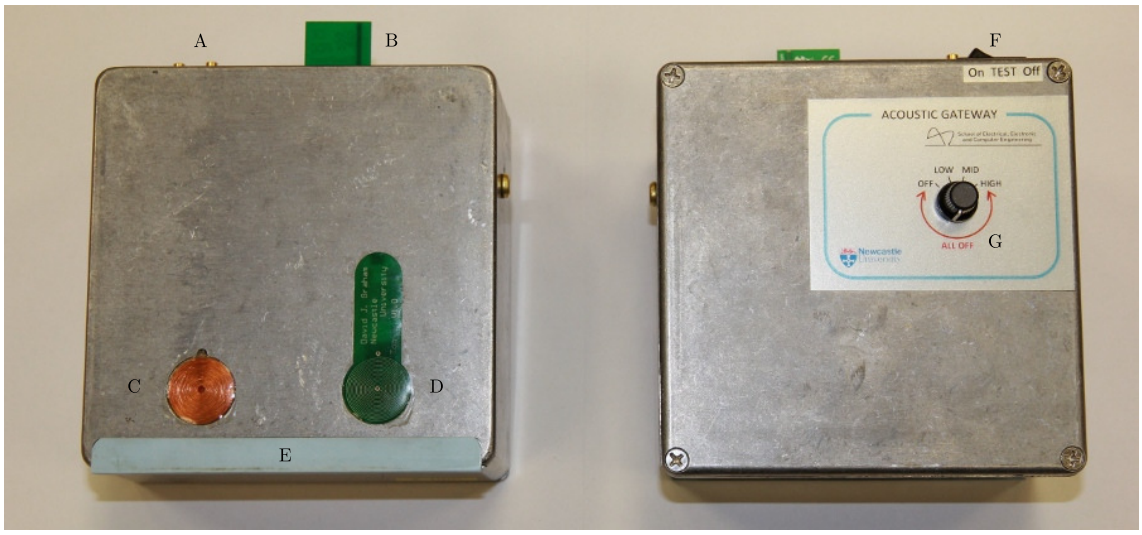

Figure 4.7: External view of Acoustic Gateway Demonstrator illustrating key features. A. Signal monitoring and serial port connectors, B. RF Antenna, C. receive EMAT coil, D. transmit EMAT coil, E. wear strip, F. operational mode selector switch, G. transmit power selector.

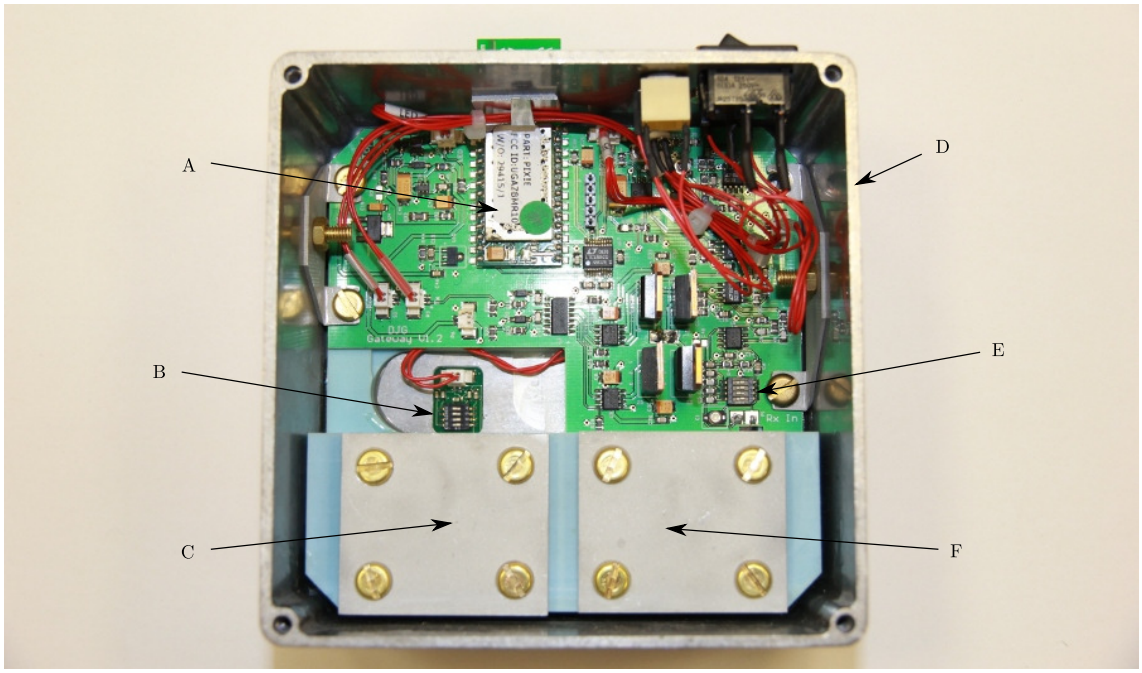

Figure 4.8: Internal view of Acoustic Gateway Demonstrator illustrating key features. A. PIXIE RF module, B. transmit coil tuning, C. transmit EMAT magnet retaining cap, D. die cast aluminium enclosure, E. receive coil tuning, F. receive EMAT magnet retaining cap.

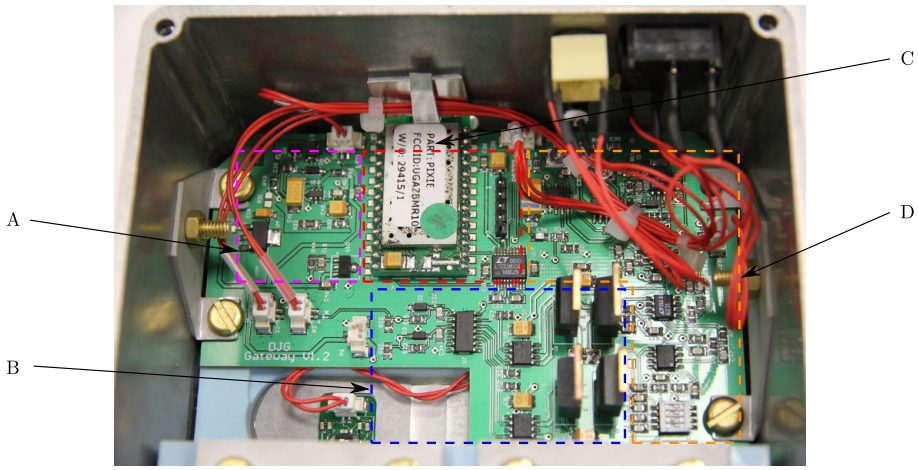

Figure 4.9: Acoustic Gateway Demonstrator circuitry. A. Power regulation, B. transmit circuitry, C. control circuitry, D. receive circuitry.

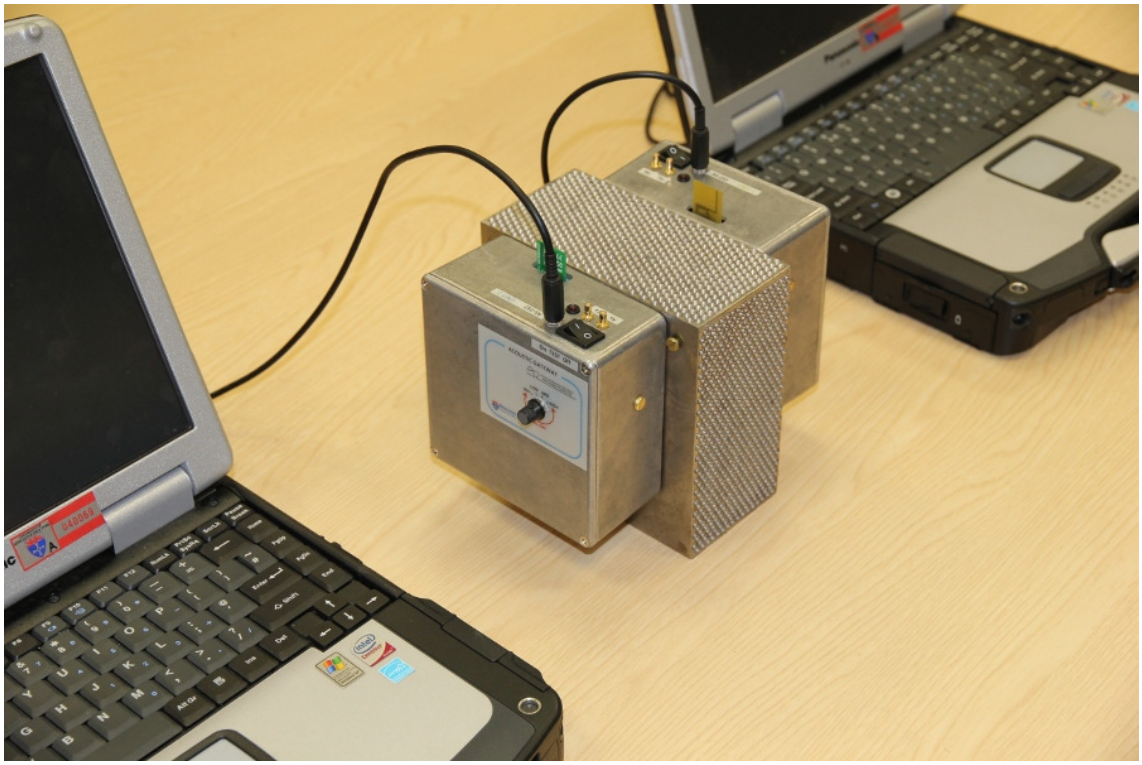

Figure 4.10: Acoustic Gateway Demonstrator, deployed on a 76.2mm thick test block, with end devices connected via the serial ports.

and receive EMAT coils are clearly visible. Due to the contrasting electrical requirements of the coils, a PCB coil is appropriate for transmitting and the receive coil is wound from enamelled wire. Both coils are potted into place with epoxy resin to prevent damage. A wear strip is located on the bottom edge and is used when positioning a unit on a ferrous wall.

The internal construction of an acoustic gateway unit is shown in Fig. 4.8. The EMAT permanent magnets are located under the retaining caps, visible at the bottom of the picture. A switched capacitor bank is included for each EMAT coil such that correct tuning can be achieved on different materials.

Fig. 4.9 outlines the control board layout and Fig. 4.10 demonstrates the gateway deployed on a 76.2mm test block.

4.4.2 Gateway Algorithm

The software control algorithm for the acoustic gateway is shown in Fig. 4.11. On power-up, there are two modes of operation: location and normal.

Location mode sets the device to transmit a single acoustic pulse at regular 10ms intervals. The partner unit may then be scanned across the other side of the wall and when the pulse is detected, the units are roughly aligned. Fine tuning, based on the amplitude of the received pulse, can then achieve near perfect alignment.

Normal operation is the gateway's data forwarding mode, the first stage of which, is to *listen* for incoming data. External interrupts are enabled for the RF transceiver, RS-232 serial port and acoustic link and the microcontroller can then enter a low power sleep state. Upon reception of data, the microcontroller wakes and determines the source of the interrupt. External interrupts are now disabled until the data forwarding cycle has completed.

The second stage is to *receive* the incoming data packet. For the case of RF or serial data packets, this is trivial. The integrity of received data is verified with a Cyclic Redundancy Check (CRC) and then it is built into an acoustic data packet as described in Section 4.4.3. Alternatively, data may be received via the acoustic communication link as described in Section 4.4.4. In which case, the acoustic transmission overhead is removed from the data packet and again, the data is verified with a CRC.

The third and final stage is to *transmit* the data. If data were received via serial or RF, the transmission will be via the acoustic link, as described in Section 4.4.4. Data received on the acoustic link is transmitted via the RF or serial interface and this will be specified in the control field of the acoustic packet.

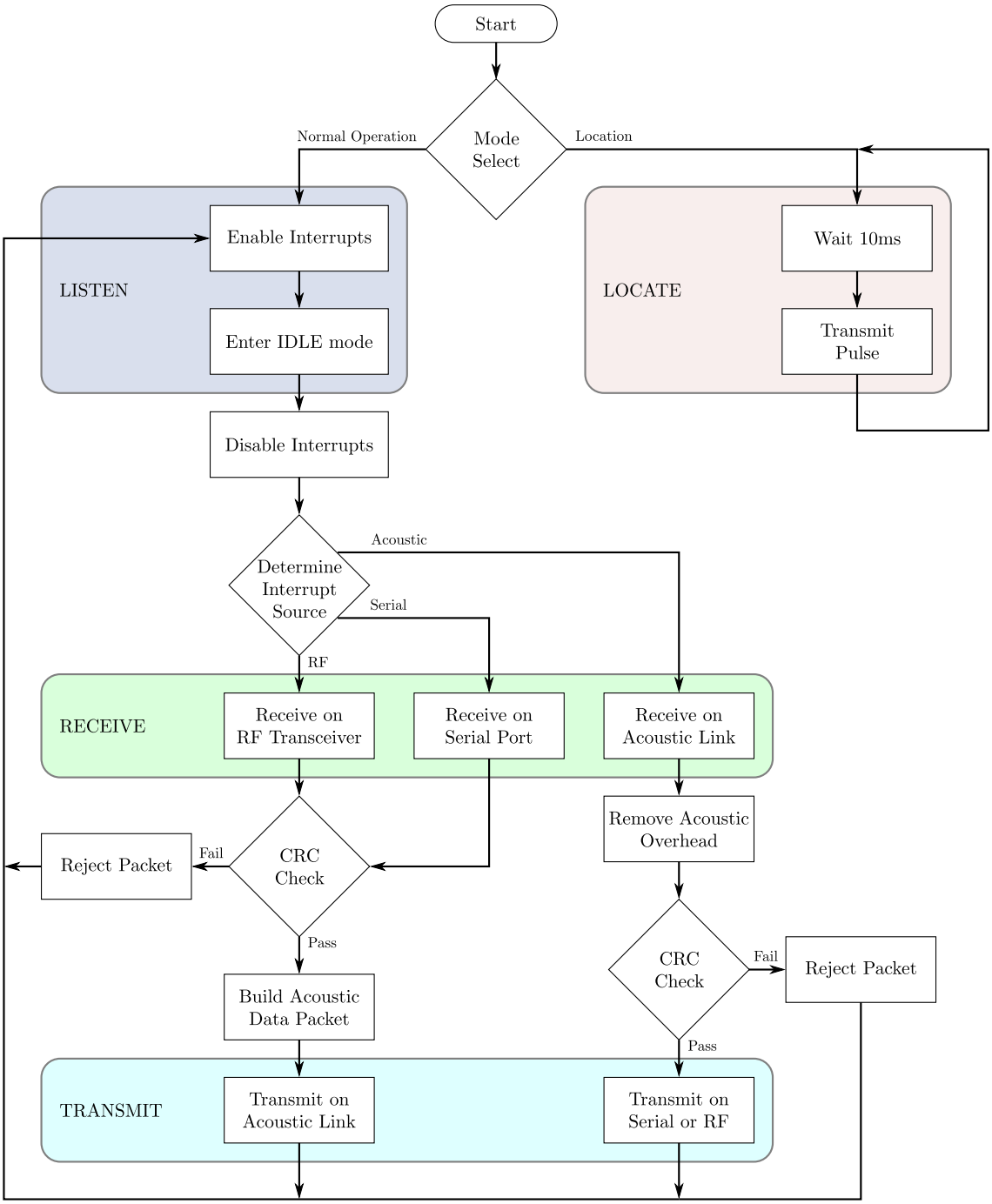

Figure 4.11: Acoustic Gateway main control algorithm for 'transparent' operation.

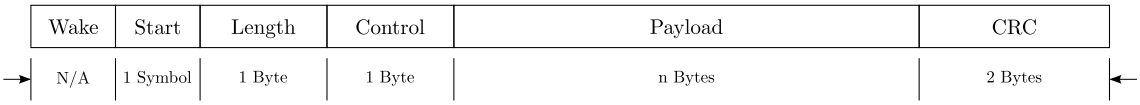

Figure 4.12: Packet structure for an acoustic data transmission.

Table 4.2: Acoustic packet field descriptions.

Field	Description
Wake (N/A)	A single pulse to wake the receiving unit, which will subsequently initialise into a state ready to receive an acoustic packet.
Start (1 Symbol)	A single symbol to indicate the start of a packet.
Length (1 Byte)	Length of the acoustic packet. Used to inform the receiving unit how many bytes to read.
Control (1 Byte)	Currently used to inform the receiving unit how to output a received packet i.e. via RS-232 or RF. Could also be useful for sending special commands for test/setup purposes.
Payload (n Bytes)	Contains the data payload which has been input via RS-232 or RF. For transparent operation, this field also includes the RF header information.
CRC (2 Bytes)	A 16 bit cyclic redundancy check is appended to the packet to minimise the probability of erroneous packets propagating through the gateway.

With the data packet successfully forwarded through the wall, the gateway returns to listening for incoming data.

4.4.3 Acoustic Packet Structure

The gateway uses the packet structure shown in Fig. 4.12, for the transmission of acoustic data. The purposes of the wake, start, length, control, payload and CRC fields are described in Table 4.2.

A CRC is used in conjunction with an automatic repeat request (ARQ) to handle erroneous packets. This is preferred to more complex forward error correction (FEC) techniques because significant coding gain cannot be achieved for the short packet lengths which are typically associated with wireless sensor networks [70].

Table 4.3: DPPM timings.

Bit Pattern	Lower (μs)	Nominal (μs)	Upper (μs)
00	< 37.5	40	< 42.5
01	< 42.5	45	< 47.5
10	< 47.5	50	< 52.5
11	< 52.5	55	< 57.5
Start	< 57.5	60	< 62.5

4.4.4 Physical Layer

After careful consideration of the various burst mode schemes, *differential pulse position modulation with guard interval* was selected for the acoustic gateway, as it is ideal for a low cost, lower power, low complexity implementation. The success of the scheme relies on the use of appropriate parameters for the guard interval, which can be obtained from the channel impulse response. The channel response of the test blocks, shown in Fig. 4.3, represent a worst case scenario for multipath and hence, are ideal for obtaining parameters which should be suitable for any steel wall or similar channel. Materials with slower propagation speeds, such as lead or tin, may experience a longer multipath duration [71].

Small residual multipath arrivals are visible for at least 160μs, hence, allowing for total multipath decay will limit the maximum symbol rate to 6.2kBd. A more practical approach is to determine the length of time that multipath arrivals are significant. On the test blocks, multipath arrivals are 20dB less than the primary pulse after approximately 40μs, at which point, the multipath is similar in amplitude to the background noise level of the pre-amplifier.

The selected symbol mappings for the gateway system are shown in Table 4.3. A start (sync) symbol is used to indicate the beginning of an acoustic transmission and initialises the software state machine upon reception. As this will only be transmitted once per packet, it is intuitive to make the start symbol the longest duration. The shortest symbol is a nominal 40μs, with 5μs chip period, resulting in a guard interval, T_G, of 37.5μs.

It is apparent from (4.6), that the data rate, $\overline{f_b}$, can be maximised with an optimum choice of modulation order, M, for a given chip period, T_c, and guard interval, T_G. This expression is repeated for convenience (4.12).

$$\overline{f_b} = \frac{2\log_2 \mathrm{M}}{(\mathrm{M}+1)\,T_c + 2T_G} \tag{4.12}$$

For $T_c = 5\mu$s and $T_G = 37.5\mu$s, both M=8 (3 bits per symbol) and M=16 (4 bits per symbol) give a mean data rate of 50kbps, but for practical reasons, M=16 (4 bits per symbol) would be preferable to give an integer number of symbols per Byte. The sub-optimal choice of M=4 is used for the gateway demonstrator, purely for simplification during the early stages of development, but as a result, it operates at a reduced mean data rate of 40kbps. The performance surface shown in Fig. 4.13 demonstrates that the optimal modulation order increases as the guard time increases. Results are normalised, such that a value of '1' represents the modulation order with the highest achievable bit rate for a given guard interval. Presenting the surface in this manner is far more informative than a comparison of absolute bit rate, which will obviously scale greatly with increasing guard interval. An ideal implementation would assess the impulse response of the channel upon installation and assign the modulation order accordingly.

Key waveforms of the gateway physical layer are shown in Fig. 4.14. A low cost microcontroller can perform all of the processing associated with the transmission and receiving of acoustic symbols. A brief overview of the selected microprocessor package is given in Section 4.4.4.1.

To transmit, an inbuilt timer module is used to encode data into variable spaced pulses, shown in Fig. 4.14a. Simple digital logic is then used to convert these pulses into the necessary control signals for the class-D amplifier arrangement, described in Section 3.4.1, which then drives the acoustic transducer.

At the receiver side, signal conditioning is performed using the analogue filter and gain circuitry, described in Section 3.4.2, resulting in the output shown in Fig. 4.14b. Envelope detection is achieved using an analogue precision rectifier and low pass filter, producing the output shown in Fig. 4.14c. A threshold is then applied to give a negative edge on each primary acoustic pulse, as shown in Fig. 4.14d. However, it is possible that multipath arrivals may also occasionally exceed this fixed threshold, resulting in additional edges. To remove erroneous edges, a monostable timer triggers on the first acoustic arrival and prevents any further edges for the duration of the guard interval.

4.4.4.1 Microcontroller

The microcontroller used for the gateway demonstrator is the PIC18F4620, an 8-bit, reduced instruction set computing (RISC) device [72]. A key factor leading to the selection of this device is that it is available as part of a PIXIE RF module, which sees it coupled with a CC2420 RF transceiver and antenna in a single compact package [73].

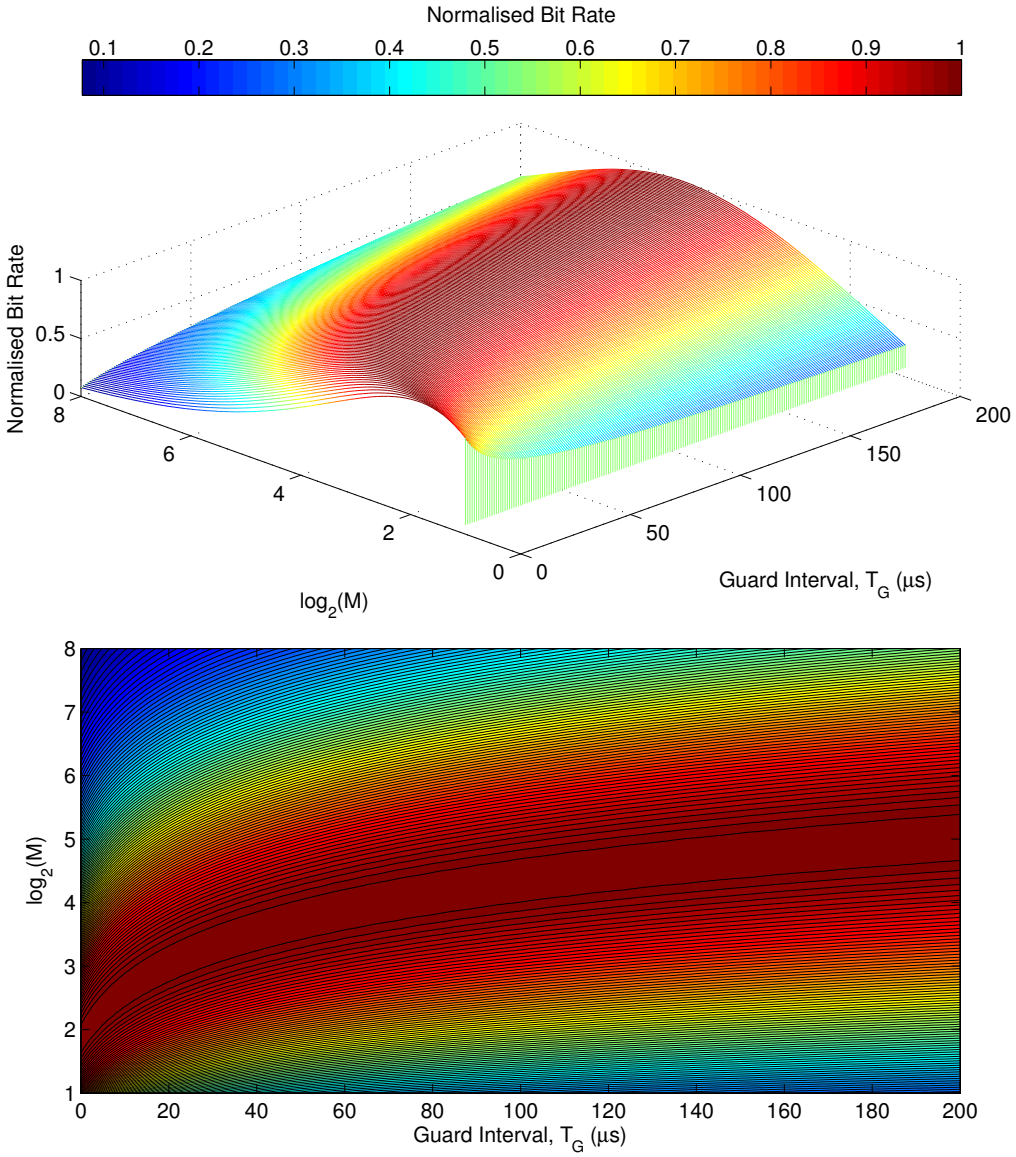

Figure 4.13: Bit rate variation with modulation order and guard time for $T_c = 5\mu$s. Results are normalised to indicate the optimal modulation order, M, for a specific guard time.

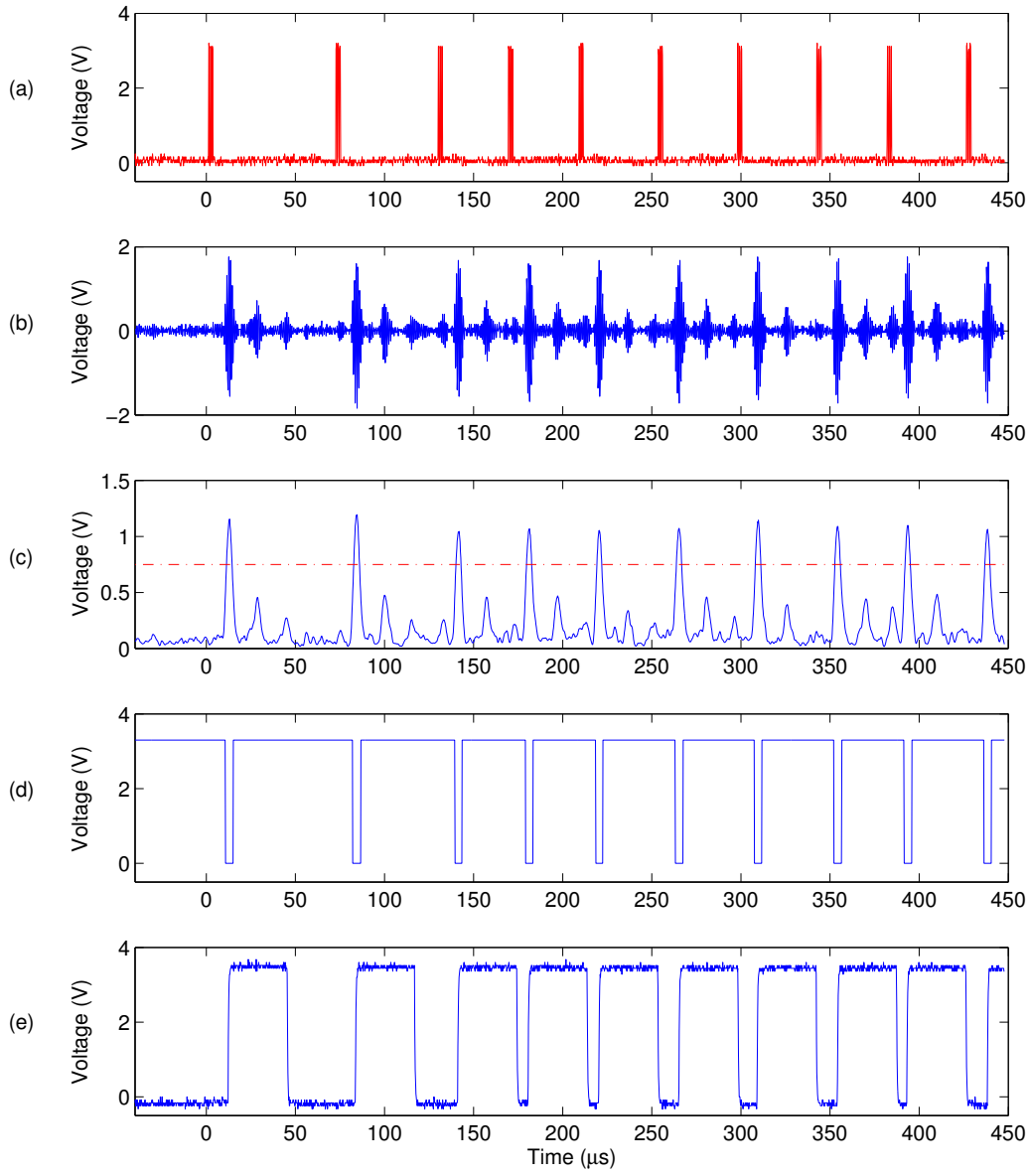

Figure 4.14: Waveforms from the pulse positioning modulation scheme. (a) Transmitter control pulses. (b) Received pulses with multipath. (c) Received signal envelope with threshold level. (d) Threshold output. (e) Gating circuit output (input to microcontroller).

The PIC18F4620 is clocked at 16MHz, resulting in a 4MHz instruction rate, and allows digital output pins to be switched at 1MHz. This clock also sets the resolution of the timer module at 250ns, and is more than adequate for distinguishing the 5μs chip periods of the modulation scheme.

The power managed modes allow the device to draw very little current when waiting for incoming data; idle mode requires of the order of a few μA.

Other features utilised are: the serial peripheral interface (SPI) bus, for communication with the RF transceiver; the universal synchronous asynchronous receiver transmitter (USART) for the serial communications interface; and the input change interrupt for the acoustic receiver.

4.4.4.2 Radio Transceiver

Each gateway unit uses a CC2420 radio transceiver, which is IEEE802.15.4 compliant, the basis for the ZigBee, WirelessHART and MiWi protocols. IEEE802.15.4 is the standard for low-rate personal area networks (LR-WPANs), which offer a low cost, low speed, low power communications solution [74].

The transceiver operates in the unlicensed 2.4GHz frequency band and can offer a maximum throughput of 250kbps, which is sufficient for the gateway application. Output power is 0dBm and can achieve ranges of up to 120m in free space when using the PCB antenna.

When transmitting, the device draws 17.4mA and when receiving, it draws 18.8mA. As shown in Section 4.4.5, this current draw is significant relative to the rest of the unit and must be managed carefully to achieve long battery life.

4.4.5 Gateway Power Consumption

Low power consumption is a key requirement of the gateway if it is to be battery operated for prolonged periods. This is a key requirement for many applications, as the changing of batteries is highly impractical and it is unlikely mains power will be available on both sides.

The system supply current waveform is shown in Fig. 4.15, for both idle and acoustically transmitting states, and has a root mean square (RMS) current draw, I_{RMS}, of 36mA and 158mA respectively. At a typical transmit voltage of 9.6V, this equates to a power consumption of 346mW when idle and 1.52W when transmitting. The current draw when transmitting acoustically can vary depending on the liftoff and wall material, due to the effect on the Tx coil properties.

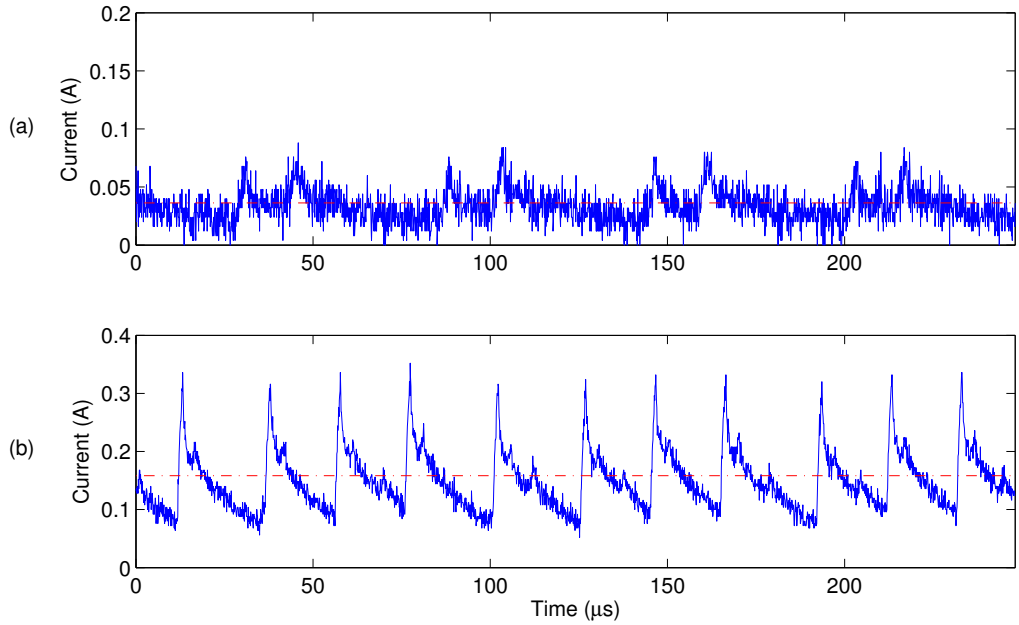

Figure 4.15: Power consumption of gateway demonstrator. (a) Idle, (b) transmitting. The RMS current draw is indicated by the dashed line.

It is important to note that there are several areas of improvement which could significantly reduce this idle consumption, as discussed in Section 4.4.5.2.

It is also worth noting the peak current draw and power consumption, which are 352mA and 3.38W respectively, as this may influence battery chemistry selection.

4.4.5.1 Maximum Total Throughput

It is possible to determine the maximum total throughput of the system, T_p, for a fixed battery capacity, Q_{Ah}, based on the current draw when transmitting, I_{RMS}, and the system bit rate, $\overline{f_b}$ (4.13). The constant, $\kappa = 3600$, is used to convert battery capacity from Ampere-hours to Ampere-seconds.

$$\mathrm{T}_p = \kappa \frac{Q_{\mathrm{Ah}} \overline{f_b}}{I_{\mathrm{RMS}}} \tag{4.13}$$

Assuming the use of Nickel Metal Hydride (NiMH) rechargeable AA cells with $Q_{\mathrm{Ah}} = 2450\mathrm{mAh}$, then $\mathrm{T}_p = 350\mathrm{MB}$; a significant amount of data for sensor network applications.

4.4.5.2 Idle Consumption

In order to achieve as close as possible to the maximum theoretical throughput, it is essential to minimise the energy consumed when idle. The gateway draws 36mA at idle, however, there are very few power saving features implemented in the current design, hence, this figure can be greatly improved upon.

Over half the power consumption is due to the RF transceiver, which draws approximately 20mA. To achieve a battery lifetime of weeks or months, a scheme must be employed which allows the radio transceiver to be powered down and 'sleep' for a large proportion of the operational lifetime. Furthermore, this would allow the acoustic receiver circuitry to be powered down on a low duty cycle. Depending on the acceptable amount of latency for a data packet, the operational duty cycle may be adjusted accordingly.

4.4.6 Wireless Networking

To allow easy integration with other wireless equipment it would be advantageous to operate the acoustic gateways using an established protocol such as ZigBee, which is based on the IEEE802.15.4 standard. If the gateway operates transparently, i.e. simply forwards data packets without modification, then the two end devices can communicate as if they were not separated by a metal barrier. However, due to the latency introduced by the gateway, this approach is not possible. The IEEE802.15.4 standard defines 'macAckWaitDuration', which is the maximum number of symbols to wait for an acknowledgement frame to arrive, following a transmitted data frame. If an acknowledgement is not received within 'macAckWaitDuration' symbols the device shall conclude that the single transmission attempt has failed. The maximum value of 'macAckWaitDuration' translates to a time period of 1.92ms; assuming a maximum length 127 Byte packet is transmitted with the acknowledgement flag bit set, it will take 20.32ms at 50kbps to transmit this data acoustically, ignoring any further processing overheads. Therefore, it is impossible for the end device to acknowledge this packet within the time defined by the standard.

The alternative is to build a custom, beacon enabled, protocol which is tolerant of the delays introduced by acoustic gateways. It would also allow the network to address issues specific to the application. Consider a complex network of gateways and nodes, with multiple transmission routes between any 2 given end nodes. A standard protocol may always select the shortest number of hops as the optimal route, however, it may be advantageous to use a different route if it helps normalise the power consumption of the gateways. The development of such a network protocol is beyond the scope of this work.

4.4.7 Field Trials

Field trials were performed on board a naval vessel at BAE Systems, Barrow-in-Furness, to assess the performance of the demonstrator system. The aim of the test was to evaluate suitability for rapid deployment on walls with different compositions, thicknesses and with various surface coatings and textures.

4.4.7.1 Setup

When a suitable location was identified, the units were placed on the wall and held in place only by the attractive force between the EMATs and ferrous wall. With the unit on one side set to transmit a test signal, the other unit is scanned in both the x and y directions until an acoustic signal is detected. The alignment is then fine tuned to maximise the received signal strength. If the units have the same horizontal orientation then aligning one transducer pair will also align the second transducer pair. Both channels are optimised with the selection of the best possible transmit voltage and coil tuning. Setup time is typically < 10 minutes but depends largely on the accuracy of the initial placement.

To test the integrity of the gateway as a bi-directional communications link, the test setup shown in Fig. 4.16 was used. 'Control Board 1' sends a 100 Byte packet via RF Link 1 to Gateway Unit 1, which relays it acoustically through the wall. The packet is then transmitted via the second RF link, on a different channel, to 'Control Board 2', which then replies with a 100 Byte acknowledgement. Gateway Unit 2 forwards the acknowledgement back through the wall via the second acoustic link and finally, it is transmitted via RF back to 'Control Board 1'. If the acknowledgement is received, the ping is deemed a success. The process is repeated 1000 times to accurately gauge packet loss.

4.4.7.2 Results and Discussion

The first ping tests were performed on slightly textured walls varying in thickness from 35-44mm, with different combinations of primer and paint coatings. The impulse response from wall 3 is shown in Fig. 4.17a. Immediately obvious is the presence of a large electromagnetic path, which is present due to the use of a battery powered oscilloscope with isolated probes and, hence, the electromagnetic signal is not a real feature of the impulse response. Otherwise, the result displays the classic response of a metal wall channel. The primary pulse is an optimal 4V peak to peak and no significant multipath is visible after 30μs; clearly the texture of the wall results in greater scattering of the reflected wave. Due to the favourable channel characteristic, the integrity of the link is very high, with an average of 1/1000 tests

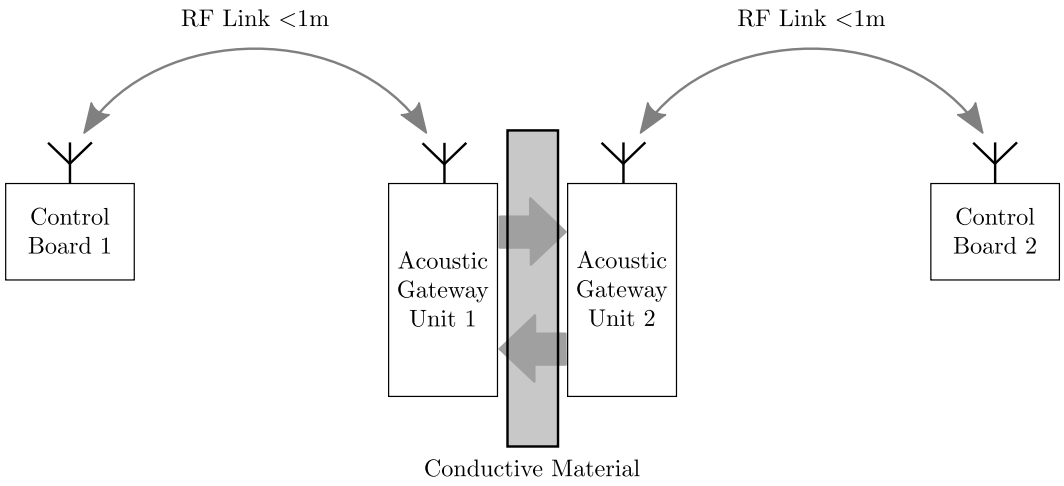

Figure 4.16: Experimental set up to evaluate the integrity of an acoustic communication link post installation.

failed. From these tests, it is clear that variations in surface coating have no bearing on the performance of the gateway, as expected.

Moving to a 72mm wall produced the impulse response shown in Fig. 4.17b. This test utilised the maximum transmit voltage of the available battery packs, 12V, however, the received pulse amplitude of 3V peak-to-peak is still at the lower limit for reliable operation. The gateway transmit circuitry is rated to 15V and could have benefited from the increased transmit power.

Due to the very large round-trip distance, there are no significant multipath arrivals. Testing resulted in 110/1000 failures but this is only due to the limited transmit power; the channel characteristics are very favourable.

The final tests were performed on a 10mm thick, painted steel wall. The channel impulse response from two different positions on wall 5 are shown in Fig. 4.17c and Fig. 4.17d and it is obvious that these results do not conform to the standard impulse response discussed previously. In Fig. 4.17c, the first reflection is larger in amplitude than the primary arrival and both are similar in amplitude to the third arrival. The lack of a clearly defined edge for a timing reference, causes complete failure of all acoustic transmissions. The second position on the same wall yields a contrasting impulse response; the primary arrival is now more clearly defined, yet the multipath is still not consistent with the channel model. A primary arrival peak-to-peak amplitude of 3V is approaching the minimum level required for pulse detection, resulting in moderate packet loss; the system fails 150/1000 tests.

The inconsistent nature of the impulse response obtained from different positions of the same steel plate indicates irregular discontinuities in the micro-structure of

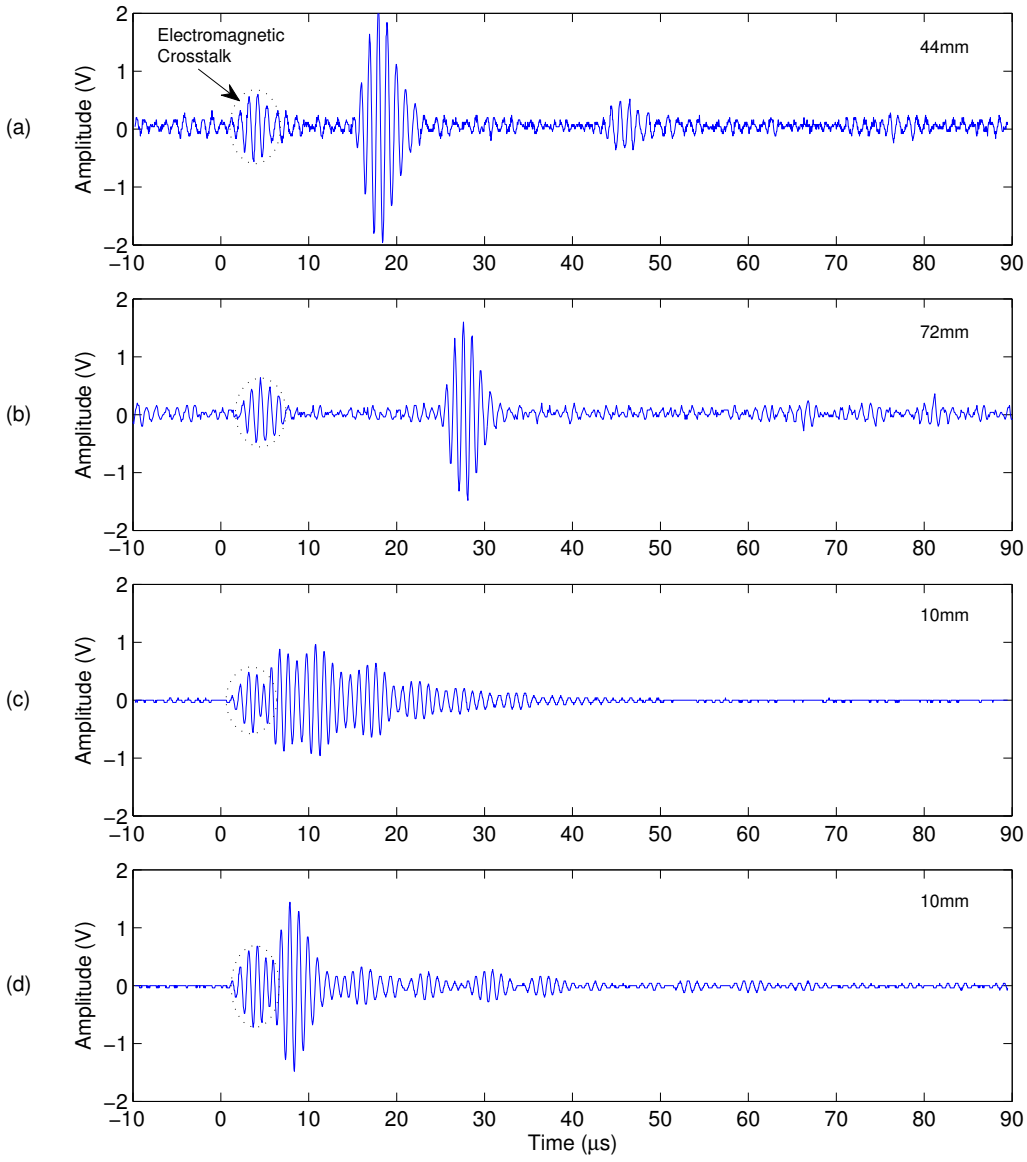

Figure 4.17: Channel impulse response of trials tests (see Table 4.4). (a) 44mm steel, wall 3. (b) 72mm steel, wall 4. (c) 10mm steel, wall 5 position 1. (d) 10mm steel, wall 5 position 2. Plots (c) and (d) were captured with the aid of signal averaging.

Table 4.4: Summary of field trial results.

Test Wall [Position]	Thickness (mm)	Tx Voltage (V)	Surface Coatings	Result (Failures)	Figure
Wall 1	35	9.6	RR	2/1000	
Wall 2	44	9.6	RR	0/1000	
Wall 3	44	9.6	PR	1/1000	4.17a
Wall 4	72	12	PR	110/1000	4.17b
Wall 5 [1]	10	9.6	PP	1000/1000	4.17c
Wall 5 [2]	10	9.6	PP	150/1000	4.17d

Key: R = Primed, P = Painted

the 10mm material. Furthermore, the primary arrival is larger through 44mm of material than through 10mm indicating it is highly attenuating. Without metallurgical analysis of the wall, it is difficult to determine the origin of the discontinuities. However, it is clear that the composition of the metal can prevent effective operation of the gateway's acoustic communications scheme.

4.5 Summary

This chapter has analysed the typical impulse response of a metal wall channel and burst mode transmission has been proposed as a means of overcoming the inherent multipath. Pulse position modulation in particular was identified as an attractive scheme due to the simplicity associated with its implementation. The acoustic gateway demonstrator system was presented, which combines PPM with EMAT technology to produce a cost-effective, rapidly deployable through metal communications system. A complete overview of the system is given, including aspects such as the acoustic protocol, the RF interface and the mean power consumption. Field trial testing demonstrates the system to perform well, except where the channel impulse response does not conform to the standard response.

Chapter 5

Continuous Wave Modulation and Equalisation

In this chapter, a second approach to an acoustic through metal communications system is presented, which aims to provide a solution to applications where the previously presented system is not suitable; high data rate applications and irregular multipath channels.

To achieve higher data rates, the system must use a continuous wave carrier, however, the inherent multipath of the metal wall channel will result in intersymbol interference. The following sections analyse various modulation schemes and equaliser structures with the aim of mitigating the effects of ISI.

The acoustic gateway demonstrator system presented in the previous chapter was designed for a very specific application, whereas this chapter presents more general techniques, which could be utilised in a system designed for either scenario A or B. However, accommodating the asymmetric setup of scenario A imposes unique design constraints.

A typical asymmetric application requires a high data rate link to extract data from the 'inside' i.e. transfer data from *inside to outside*. The typical requirements for data transfer from *outside to inside* are far more modest, consisting of simple commands to be sent to the 'inside' setup. Sealed metal containers are often used to isolate hazardous materials or processes and as a result, the inside is often hostile, involving radiation and/or elevated temperatures. Consequently, it is advantageous to minimise the complexity of the 'inside' electronics due to the environmental conditions, but also due to size and power constraints.

Resilient electronics are still somewhat in their infancy but by minimising the complexity of the 'inside' electronics an equivalent resilient system is one step closer and could be feasible within a few years [75]. For the case of high bit rate through metal communications, this means *minimising the complexity of the transmitter design.*

In the following sections various modulation schemes and receiver structures are introduced and results are presented comparing the performance of a linear equaliser (LE) and decision feedback equaliser (DFE) for a metal wall channel. Finally, the power consumption of equivalent piezoelectric and EMAT systems are compared to evaluate the penalty associated with the low transduction efficiency of EMATs.

5.1 Channel Capacity

The channel capacity defines the tightest upper bound on the amount of information that can be reliably transmitted over a communication channel [76]. The theoretical capacity, C_c, of an additive white Gaussian noise (AWGN) channel can be calculated using the Shannon-Hartley theorem (5.1), where Δf is the bandwidth and SNR is the signal to noise ratio expressed as a linear power ratio.

$$C_c = \Delta f \log_2(1 + \mathrm{SNR}) \tag{5.1}$$

Hence, for any given channel, if the data rate, f_b, is less than the channel capacity, C_c, i.e. $(f_b < C_c)$, then it is theoretically possible to achieve error-free transmission with appropriate coding. However, the work of Shannon serves only to establish the limit and does not provide any insight as to the modulation schemes or coding to achieve this theoretical bound.

5.2 Modulation Schemes

Modulation schemes suitable for burst mode transmission have been introduced previously. The limiting factor affecting the achievable data rate of a simplistic burst mode scheme is the duration of the multipath relative to the duration of a data symbol; for the case of a metal wall channel, this ratio is large. To achieve higher data rates, it is imperative to minimise or remove the guard interval. One option is a conventional single carrier scheme, which will require channel equalisation; the alternative is a more complex, but inherently multipath tolerant, multi-carrier scheme.

5.2.1 Single Carrier

In this section, three linear modulation schemes are considered: amplitude shift keying (ASK); phase shift keying (PSK); and quadrature amplitude modulation

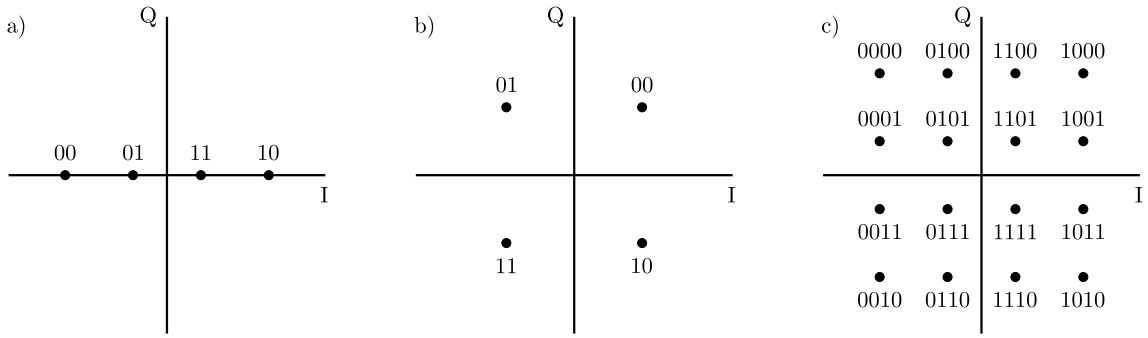

Figure 5.1: Signal space diagrams with Gray coding. (a) 4-ASK, (b) QPSK, and (c) rectangular 16-QAM. I and Q denote the In-phase and Quadrature axes respectively.

(QAM). Each of these schemes utilises a single digitally modulated carrier, occupying the entire channel bandwidth [77].

M-ASK conveys data using M amplitudes, each of which correspond to one of M k-bit symbols, where $k = \log_2 M$. The signal waveform, $s_m(t)$, may be expressed as shown in (5.4), where A_m is the set of M possible amplitudes (5.2), $g(t)$ is the pulse shape and f_c is the centre frequency.

$$A_m = 2m - 1 - M \qquad m = 1, 2, \ldots, M \tag{5.2}$$

$$\begin{aligned} s_m(t) &= \mathrm{Re}\left[A_m g(t) e^{j2\pi f_c t}\right], \qquad m = 1, 2, \ldots, M && (5.3)\\ &= A_m g(t) \cos\left(2\pi f_c t\right) && (5.4) \end{aligned}$$

The signal space diagram for 4-ASK is shown in Fig. 5.1a. The constellation is usually Gray coded to minimise bit errors; an incorrect decision at the receiver due to random noise is most likely to select an adjacent amplitude, hence only a single bit of the k-bit sequence will be erroneous [78].

For the case of M-PSK, data is conveyed using constant amplitude and M possible carrier phases, θ_m, (5.5) resulting in the corresponding signal waveform, $s_m(t)$ (5.7). Consequently, each point of the signal space diagram lies on the unit circle, as shown for the case $M = 4$ in Fig. 5.1b.

$$\theta_m = \frac{2\pi(m-1)}{M} \qquad m = 1, 2, \ldots, M \tag{5.5}$$

$$\begin{aligned} s_m(t) =& \mathrm{Re}\left[e^{j\theta_m} g(t) e^{j2\pi f_c t}\right], \qquad m = 1, 2, \ldots, M && (5.6)\\ =& \cos\left(\theta_m\right) g(t) \cos\left(2\pi f_c t\right) - \sin\left(\theta_m\right) g(t) \sin\left(2\pi f_c t\right) && (5.7) \end{aligned}$$

Table 5.1: Analytical expressions for minimum Euclidean distance, $d_{\min}$, of M-ASK, M-PSK and rectangular M-QAM in terms of the average energy per bit, $\varepsilon_{\text{bavg}}$. Approximate evaluations are given for M=2 to M=16. The expression for M-QAM is only valid for square numbers. Note: the $\sqrt{\varepsilon_{\text{bavg}}}$ term is omitted in columns 3-6.

Scheme	$d_{\min}$	$M=2$	$M=4$	$M=8$	$M=16$
M-ASK	$\sqrt{\frac{12\log_2 M}{M^2-1}\varepsilon_{\text{bavg}}}$	2	1.26	0.76	0.43
M-PSK	$2\sqrt{\log_2 M \sin^2\left(\frac{\pi}{M}\right)\varepsilon_{\text{bavg}}}$	2	2	1.33	0.78
M-QAM	$\sqrt{\frac{6\log_2 M}{M-1}\varepsilon_{\text{bavg}}}$	(2)	2	(1.26)	1.26

M-QAM simultaneously modulates two quadrature carriers, $\cos(2\pi f_c)$ and $\sin(2\pi f_c)$, with k-bit symbols from an input data stream. The resultant signal waveform, $s_m(t)$, can be expressed as shown in (5.9), where A_{mi} and A_{mq} are the amplitudes of the in-phase and quadrature carriers respectively.

$$s_m(t) = \text{Re}\left[(A_{mi} + jA_{mq})\, g(t) e^{j2\pi f_c t}\right], \qquad m = 1, 2, \ldots, M \tag{5.8}$$

$$= A_{mi} g(t)\cos(2\pi f_c t) - A_{mq} g(t)\sin(2\pi f_c t) \tag{5.9}$$

The signal waveform exhibits both amplitude and phase modulation, as shown in Fig. 5.1c, and from (5.3), (5.6) and (5.8), it is clear that the three schemes are related; in fact, ASK and PSK may be considered special cases of QAM. Due to this relation, each of the schemes can be modulated using the same general structure.

The minimum Euclidean distance, $d_{\min}$, describes the minimum straight-line separation of two adjacent points of a signal space diagram. All else being equal, a modulation scheme with a smaller $d_{\min}$ requires higher SNR to achieve an equivalent BER. Table 5.1 gives expressions for $d_{\min}$ in terms of the modulation order, M, and average energy per bit, $\varepsilon_{\text{bavg}}$, for M-ASK, M-PSK and rectangular M-QAM. When the signalling is binary, i.e. $M = 2$, M-ASK and M-PSK are equivalent schemes. Likewise, when the signalling is quaternary, i.e. $M = 4$, M-PSK and rectangular M-QAM are identical schemes. It is also notable that 4-PSK (QPSK) offers improved performance versus 4-ASK. When $M = 8$, 8-PSK is the most attractive scheme, however, it offers very similar performance to rectangular 16-QAM, yet only three quarters of the data rate, and hence, QAM is often the preferred choice for higher order systems.

A practical implementation of QAM requires a linear amplifier for transmission. As discussed previously in Section 3.4.1, a linear amplifier for driving an EMAT is not

ideal due to the inherently low efficiency. As a result, *PSK is more attractive than either ASK or QAM for an EMAT based through metal communications system.*

5.2.2 Multi-Carrier (OFDM)

Orthogonal frequency division multiplexing (OFDM) is an increasingly popular digital multi-carrier modulation method which utilises orthogonal sub-carriers to convey data [79–81]. A multi-carrier modulation scheme divides the available bandwidth, Δf, into N narrow sub-bands, each of which have an equal bandwidth, Δf_{SB}, but can be independently modulated and coded (5.10).

$$\Delta f_{\mathrm{SB}} = \frac{\Delta f}{N} \tag{5.10}$$

If N is sufficiently large and hence, Δf_{SB} is sufficiently small, the channel frequency response can be considered to be flat across each sub-band. As a result, a frequency selective fading channel becomes a series of flat fading channels.

If a single carrier system has a symbol period T, then an equivalent multi-carrier system conveys the same data in a symbol period T_O, which is determined from the number of sub-carriers, N (5.11).

$$T_O = NT \tag{5.11}$$

If N is sufficiently large, then the OFDM symbol period, T_O, is large relative to the channel multipath delay, T_m, and a guard interval, $T_G > T_m$, can be introduced to avoid any intersymbol interference, with minimal overhead. The system overcomes ISI without equalisation using a guard interval, which is analogous to that used in burst mode schemes. The key difference is that the ratio of the guard interval to the symbol length is far more favourable for an OFDM system.

The key components of a multi-carrier communications system are shown in Fig. 5.2. It has been shown previously that the fast Fourier transform (FFT) is an efficient means to modulate and demodulate multi-carrier transmissions [82, 83]. Using this implementation, it is advantageous to transmit a cyclic prefix, i.e. utilise the guard interval to transmit a repeat of the end of the OFDM symbol. The cyclic prefix maintains orthogonality of the signal and simplifies the receiver design [84, 85].

For improved performance with quasi-static multipath fading channels, the M-QAM constellation size used for each sub-band can be assigned according to the SNR. The SNR must be measured at the receiver side and conveyed back to the transmit side. If the SNR of a sub-band is below a threshold, such that it cannot support the

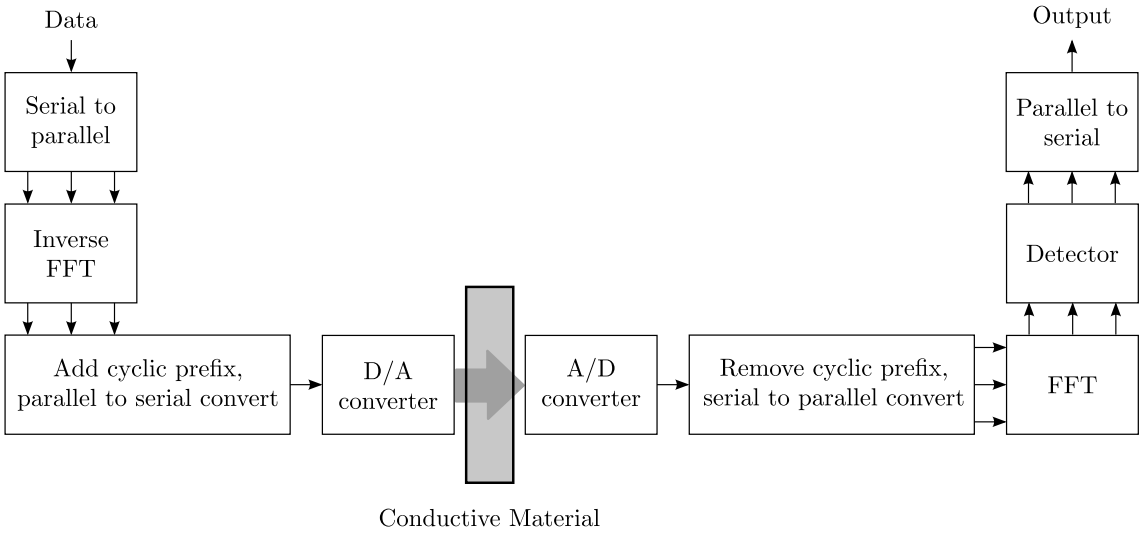

Figure 5.2: A multi-carrier communications system employing the fast Fourier transform (FFT), and its inverse, for demodulation and modulation respectively. Acoustic transmit and receive circuitry is omitted for simplicity.

minimum constellation size, usually $M = 4$, at the desired error probability, then no data will be conveyed on that sub-band.

OFDM is also a powerful technique if used in conjunction with powerful forward error correction codes. This approach allows faded carriers to be corrected and hence, reliable communications can be achieved in severe fading channels. Furthermore, it does not matter which carriers experience fades which also makes the technique attractive for dynamic channels.

The advantages of OFDM for a multipath channel are clear but there are some unique disadvantages associated with its implementation. Firstly, fairly sophisticated electronics are required to form the transmit signal; secondly, the resultant waveform has a high peak-to-average power ratio (PAPR), whereby large peaks occur when the signals within multiple sub-bands add constructively in-phase [83]. This creates the requirement for a very linear amplifier with large dynamic range that adds significant complexity to the transmitter power electronics [86]. Finally, it is essential there is very accurate frequency synchronisation between transmitter and receiver, which means tight specifications on the local oscillators [87].

5.3 Equalisation

A single carrier scheme will always be subject to ISI in a multipath channel. As a result, most communications systems employ some form of channel equalisation

to mitigate the effects of ISI. Only Primerano *et al.* (2007) (2009) [15, 47] have attempted to equalise a metal wall channel as discussed previously in Section 2.4.1.3. The system proposed by Primerano *et al.* employs equalisation at the transmitting side, which can avoid noise enhancement associated with some receiver structures [88] but adds complexity to the transmitter and reduces the system power efficiency.

In the following sections, three approaches are considered which can be implemented at the receiving side: the optimum maximum likelihood receiver and the sub-optimum linear equaliser and decision feedback equaliser.

5.3.1 Maximum Likelihood Receiver

The maximum-likelihood (ML) receiver is an optimum receiver that selects the most probable transmitted signal, given a waveform that it has observed.

For a multipath channel, the computational complexity of the ML receiver grows exponentially with the channel delay spread. Thus, for an M-ary modulation scheme and a channel delay spread spanning L symbols, M^{L+1} new metrics must be calculated for each new symbol [77]. Typically, this makes the ML receiver computationally expensive and unsuitable for real-world embedded systems applications.

5.3.2 Linear Equaliser

The prohibitive computational complexity of the optimal ML receiver necessitated the development of sub-optimal solutions to the channel equalisation problem; one such solution is the linear equaliser (LE). An LE may be realised as a transversal, or finite-duration impulse response (FIR), filter whose computational complexity grows as a linear function of the channel delay spread [89]. The general structure is shown in Fig. 5.3 and consists of: unit delay elements, denoted by z^{-1}; multipliers; and an adder, denoted by Σ.

The nth filter output, $\hat{s}_n$, is an estimate of the information symbol, s_n, and can be calculated as the convolution sum of the filter impulse response, and $L = 2K + 1$ samples of the unequalised input vector. This may be expressed formally, as given in (5.12), where x_n is the nth sample of the unequalised input and w_k is the kth filter coefficient.

Each filter output, $\hat{s}_n$, is quantized to the nearest information symbol, forming the symbol decision, $\tilde{s}_n$; a symbol decision is in error if $\tilde{s}_n \neq s_n$.

$$\hat{s}_n = \sum_{k=-K}^{K} w_k x_{n-k} \tag{5.12}$$

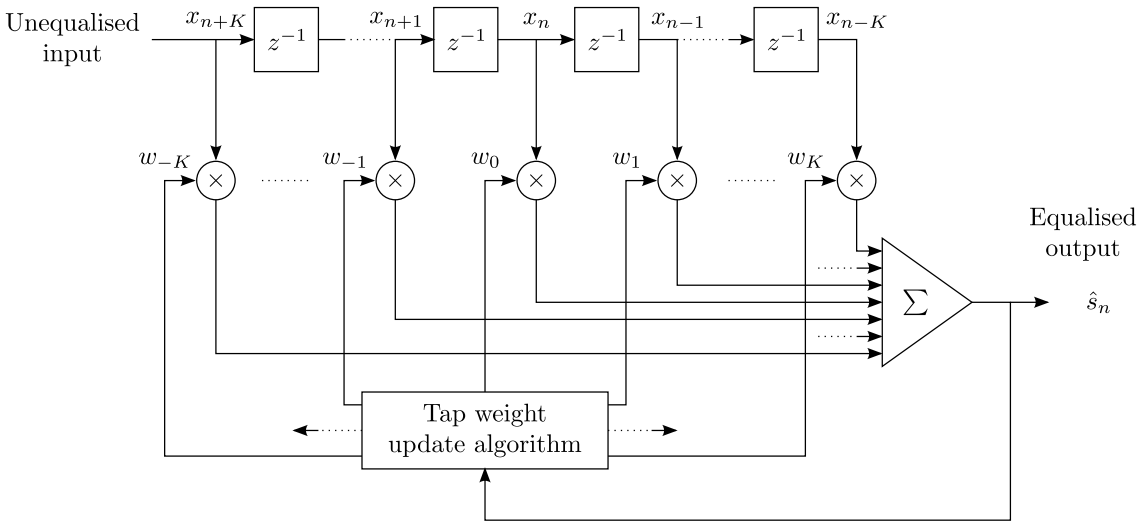

Figure 5.3: A $(2K+1)$th order transversal filter structure.

5.3.2.1 Filter Weights

The performance of the equaliser is dependent on the appropriate selection of the filter tap weights (coefficients). The most popular criterion for optimising the equaliser weights is the mean square error (MSE). For a complex valued equaliser, the performance index for the MSE, J_{MSE}, is given by (5.13), where E denotes the expectation.

$$J_{\text{MSE}} = E\left|s_n - \hat{s}_n\right|^2 \tag{5.13}$$

The Wiener-Hopf equations are a set of $2K+1$ simultaneous equations, which define the optimal filter weights, $\mathbf{w}_{\text{opt}}$, based on the minimal mean square error criterion. The solution may be expressed in matrix form (5.14), where $\mathbf{R}_{\mathbf{xx}}$ is the autocorrelation matrix of the unequalised input, $\mathbf{x}$, and $\mathbf{R}_{\hat{s}\mathbf{x}}$ is the cross-correlation of $\mathbf{x}$ and the desired response $\tilde{s}_n$.

$$\mathbf{w}_{\text{opt}} = \mathbf{R}_{\mathbf{xx}}^{-1}\mathbf{R}_{\tilde{s}\mathbf{x}} \tag{5.14}$$

The matrix form Wiener-Hopf equation is often not used directly due to the computational expense of inverting an $L \times L$ matrix. Furthermore, if a channel has any time variability then the tap weights must be re-evaluated periodically to track the changing conditions, which is highly inefficient. Consequently, there has been great interest in the development of iterative solutions to obtaining the Wiener filter response, as discussed in Section 5.4.

5.3.2.2 Tap Spacing

A symbol rate equaliser has a tap spacing equal to the symbol period, T, i.e. a single tap for each symbol. This spacing will result in the largest time span for a fixed order filter. However, this configuration is very sensitive to the symbol sampling instant. It has been shown previously that a fractionally spaced equaliser (FSE) achieves superior performance with an equal number of taps, as it can compensate for arbitrary timing phase, even though it only encompasses a fraction of the time span [88]. In practice, many systems employ a Nyquist rate, $\frac{T}{2}$-spaced equaliser [90–92].

5.3.2.3 Limitations

A linear equaliser is sufficient for channel equalisation provided the channel does not exhibit deep fades or spectral nulls. If a channel has severe ISI, deep fades can attenuate the signal below the noise floor of the system. Equalising such a channel with a linear equaliser will result in large and unwanted noise enhancement.

5.3.3 Decision Feedback Equaliser

The decision feedback equaliser is an alternative, suboptimal equaliser which will typically achieve superior performance, in comparison to the linear equaliser, in the presence of severe ISI [77, 88]. The DFE structure consists of a feed-forward transversal filter, a feedback transversal filter and a decision device as shown in Fig. 5.4. The nth signal estimate, $\hat{s}_n$, is obtained from (5.15), where w_k is the kth tap coefficient of the filter, x_n is the nth sample of the unequalised input and $\tilde{s}_{n-k}$ is a previous symbol decision.

$$\hat{s}_n = \sum_{k=-K_1}^{0} w_k x_{n-k} - \sum_{k=1}^{K_2} w_k \tilde{s}_{n-k} \tag{5.15}$$

The introduction of feedback to the structure allows the ISI contribution due to previous symbols to be subtracted from the current symbol. Consequently, the DFE is ideally suited to channels which exhibit long delay spreads. The process of feeding back hard decisions makes the DFE a non-linear equaliser.

For the reasons outlined during the discussion of the linear equaliser, it is advantageous to use a fractionally spaced equaliser for the feed-forward filter of a DFE. There is no advantage to be used by employing a feedback filter with less than T-spacing. In order to remove all ISI contributions, the feedback filter should span the complete length of the multipath delay spread.

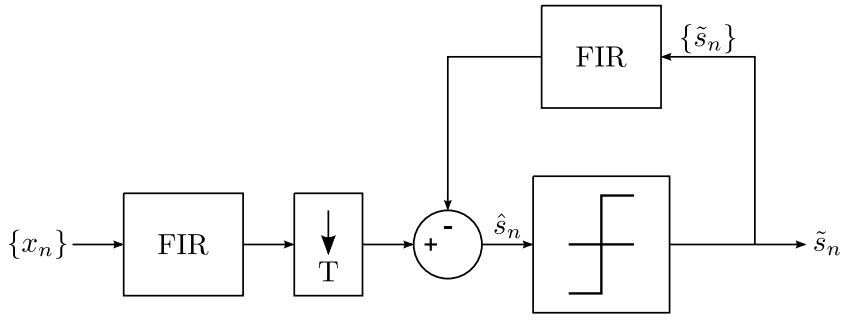

Figure 5.4: A decision feedback equaliser structure.

5.3.3.1 Limitations

An obvious weakness, inherent to the decision feedback equaliser, is error propagation. An incorrect symbol decision will adversely affect K_2 subsequent symbol decisions. When an erroneous symbol decision is subtracted from future symbols, there is an increased likelihood of error, hence, an incorrect decision can trigger a burst of erroneous symbol decisions [93].

5.4 Filter Coefficient Update Algorithms

Successful channel equalisation, using either an LE or DFE, requires the calculation of the appropriate filter tap coefficients. The Wiener filter solution can be used to calculate optimal coefficients provided the statistical characteristics of the input are known. As discussed previously, the computational complexity of the Wiener-Hopf equations make the technique unattractive and furthermore, the coefficients only remain optimal as long as the channel response remains static.

The time variability of a metal wall channel was introduced in Section 4.1.3.2, where it was shown that both temperature and mechanical stress can alter the phase and position of the features within the channel response.

If it is assumed that there is fractional change in propagation speed of 0.025 [63], a symbol period is $T = 2 \times 10^{-6}$s and the multipath duration is $T_m = 160 \times 10^{-6}$s (Section 4.1.4) then it can be shown that the later multipath arrivals of the channel IR will shift by greater than a symbol period! Thus it is obvious that even smaller fractional changes in the propagation speed are sufficient to alter the phase relationship and require a coefficient update.

Due to this potential variation, it is necessary to evaluate the filter coefficients periodically. However, it is unlikely that a significant enough temperature/stress

gradient can occur within the short duration of a single packet transmission to alter the response.

5.4.1 Least Mean Square

The least mean square (LMS) algorithm is a stochastic steepest descent algorithm, which provides an iterative solution to the Wiener-Hopf equations.

An iteration of the LMS algorithm involves three stages: firstly, the output of a linear filter is calculated in response to an input signal; secondly, an error signal is produced by comparing the filter output with the desired response; finally, the filter tap weights are adjusted according to the error signal.

The tap weight adjustment is optimised based on the minimum mean square error criterion, which is a second order function of the filter weights and hence, produces a paraboloid error-performance surface with a unique minimum point [89]. Each set of filter coefficients corresponds to some point on this surface. The method calculates an instantaneous estimate of the gradient vector and subsequently, each tap weight is changed in the direction opposite to its corresponding gradient component [77]. Over several iterations this process should converge toward the minimum of the paraboloid and give a close approximation to the Wiener solution.

The output of the adaptive filter, $\hat{s}_n$, is determined from the input vector $\mathbf{x}_n$ and the current filter weight vector $\mathbf{w}_n$ (5.16). An error signal, e_n, can then be calculated from the difference between the filter output, $\hat{s}_n$, and the desired response, s_n (5.17). A new set of filter coefficients, $\mathbf{w}_{n+1}$, are then calculated according to the tap update equation (5.18), where Δ is a small positive quantity referred to as the step-size parameter.

$$\hat{s}_n = \mathbf{w}_n^H \mathbf{x}_n \tag{5.16}$$

$$e_n = s_n - \hat{s}_n \tag{5.17}$$

$$\mathbf{w}_{n+1} = \mathbf{w}_n + \Delta e_n^* \mathbf{x}_n \tag{5.18}$$

5.4.1.1 Training Mode

To correctly form the error signal, e_n, the receiver requires knowledge of the transmitted signal, which during normal operation it will not have. A common solution is to begin a data packet with a training sequence, which is known to the receiver

Table 5.2: A comparison of the estimated computational cost per iteration for LMS and RLS algorithms, for the case of complex valued data, in terms of the number of real multiplications, real additions and real divisions. [94]

Algorithm	$\times$	$+$	$/$
LMS	$8L+2$	$8L$	0
RLS	$4L^2+16L+1$	$4L^2+12L-1$	1

and allows the filter tap weights to converge to a near optimal solution. Once the filter weights have converged, the system may switch to a decision directed mode of operation where all symbol decisions are assumed to be correct and $\tilde{s}_n$ is used in place of s_n to form e_n (5.19).

$$e_n = \tilde{s}_n - \hat{s}_n \tag{5.19}$$

Provided the system operates with only the occasional error then using $\tilde{s}_n$ to form the error signal will have a negligible effect on overall performance. Usual practice is to use a pseudo-random number sequence (PN code) during the training sequence due to its broad, uniform spectrum [88]. As no data is conveyed during the training sequence, it may be considered 'packet overhead' and hence, it is desirable to minimise the length of the training sequence. The minimum length is largely dependant on the convergence properties of the algorithm.

5.4.1.2 Convergence

The convergence properties of the LMS algorithm are controlled by the step-size parameter, Δ. Selecting the step-size is a trade off; a larger step-size will result in faster initial convergence but greater steady state error, while a smaller step-size will converge slower but the excess MSE will also be reduced.

5.4.2 Recursive Least Squares

The recursive least squares (RLS) algorithm is an alternative to the LMS algorithm, which uses a performance index based on a time average rather than a statistical average [77, 88]. The convergence rate of the RLS algorithm is typically an order of magnitude faster than LMS [89]. This is achieved by using an array of parameters to update each tap coefficient independently, where, in comparison, the LMS algorithm must rely on a single global parameter to control convergence.

The major disadvantage of the RLS algorithm is the increased computational complexity, as outlined in Table 5.2. The classical RLS algorithm requires of the order of L^2 operations, however, more modern lattice implementations have shown the complexity can be reduced with minor impact on performance [95]. Even so, the complexity is still considerably greater than the LMS algorithm.

An increased rate of convergence is advantageous for Scenario A; faster convergence reduces the training sequence length requirement and, consequently, packet overhead is reduced. Transmitting fewer training symbols reduces power consumption at the transmitter but the increased computation increases power consumption at the receiver, and, hence the result is a transfer of power consumption from the *inside* electronics to the *outside* electronics.

The recursive computation for the time update of the filter coefficients, $\mathbf{w}_n(t)$, begins with the computation of the output, $\hat{s}(t)$ (5.20), where $\mathbf{x}_n^t(t)$ is the input vector. For the first iteration, $\mathbf{w}_n(t-1)$ is initialised to all zeros.

$$\hat{s}(t) = \mathbf{x}_n^t(t)\mathbf{w}_n(t-1) \tag{5.20}$$

The error, $e_n(t)$, is calculated as the difference between the desired symbol, $s(t)$, and the symbol estimate, $\hat{s}(t)$ (5.21).

$$e_n(t) = s(t) - \hat{s}(t) \tag{5.21}$$

The Kalman gain vector is calculated from (5.22), where, $\mathbf{P}_n(t-1)$ is the inverse of the correlation matrix and λ_f is a forgetting factor; an exponential weighting factor, which gives less weight to data in the remote past and more weight to recent data.

$$\mathbf{K}_n(t) = \frac{\mathbf{P}_n(t-1)\mathbf{x}_n^t(t)}{\lambda_f + \mathbf{x}_n^t(t)\mathbf{P}_n(t-1)\mathbf{x}_n^*(t)} \tag{5.22}$$

The inverse of the correlation matrix may then be updated from (5.23).

$$\mathbf{P}_n(t) = \lambda_f^{-1}\mathbf{P}_n(t-1) - \lambda_f^{-1}\mathbf{K}_n(t)\mathbf{x}_n^t(t)\mathbf{P}_n(t-1) \tag{5.23}$$

Finally, the filter coefficients are updated according to (5.24). Equations (5.20)-(5.24) constitute the classical RLS update algorithm.

$$\mathbf{w}_n(t) = \mathbf{w}_n(t-1) + \mathbf{K}_n(t)e_n^*(t) \tag{5.24}$$

5.5 Forward Error Correction

Forward error correction (FEC) is an essential component of any modern high speed communications system. Generally speaking, an FEC scheme will introduce some redundancy to a data transmission in such a way that allows errors to be detected and corrected. The coding rate, r, is a measure of the level of redundancy, which may be calculated from (5.25), where k_L is the input symbol block length and n_L is the codeword length ($n_L > k_L$).

$$r = \frac{k_L}{n_L} \qquad (r < 1) \tag{5.25}$$

A well designed code results in a net coding gain, which is the difference in the SNR required between uncoded and coded systems achieving the same probability of error, whilst also taking into account the increased bandwidth requirement due to the code rate [96].

There are many families of codes with varying levels of performance and computational complexity, including linear block codes, cyclic codes, convolutional codes, turbo codes and low-density parity check codes. Turbo codes achieve the greatest net coding gain of all known codes [97, 98], however, the iterative decoding process can be computationally expensive.

Experimental results presented later in this chapter are uncoded, with the understanding that improved performance could be achieved using appropriate coding in a predictable manner. The code should be selected to match the noise characteristics and error statistics of the channel.

5.6 Hardware Implementation

The project sponsors, BAE Systems, put a strong emphasis on hardware demonstration. In light of this, a test bed was constructed to transmit, receive and capture high bit rate acoustic data packets.

5.6.1 Transmitter

An overview of the transmitter construction is shown in Fig. 5.5. The transmitter is simplified by using a 12-state quasi-sine QPSK output. Although 6 states would be sufficient to describe a continuous carrier, the 30° resolution provided by a 12 state approximation are required to resolve the 4 QPSK phases shown in Fig. 5.6.

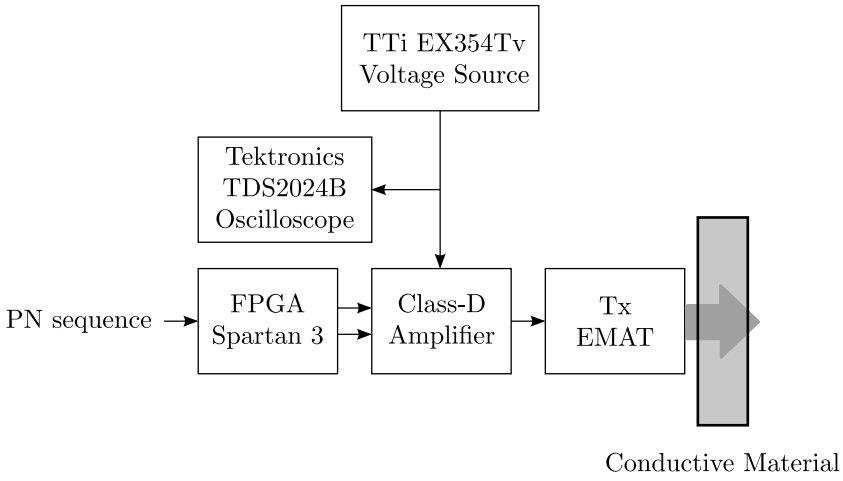

Figure 5.5: QPSK transmitter for acoustic through metal communications. The input current to the amplifier is measured with an oscilloscope.

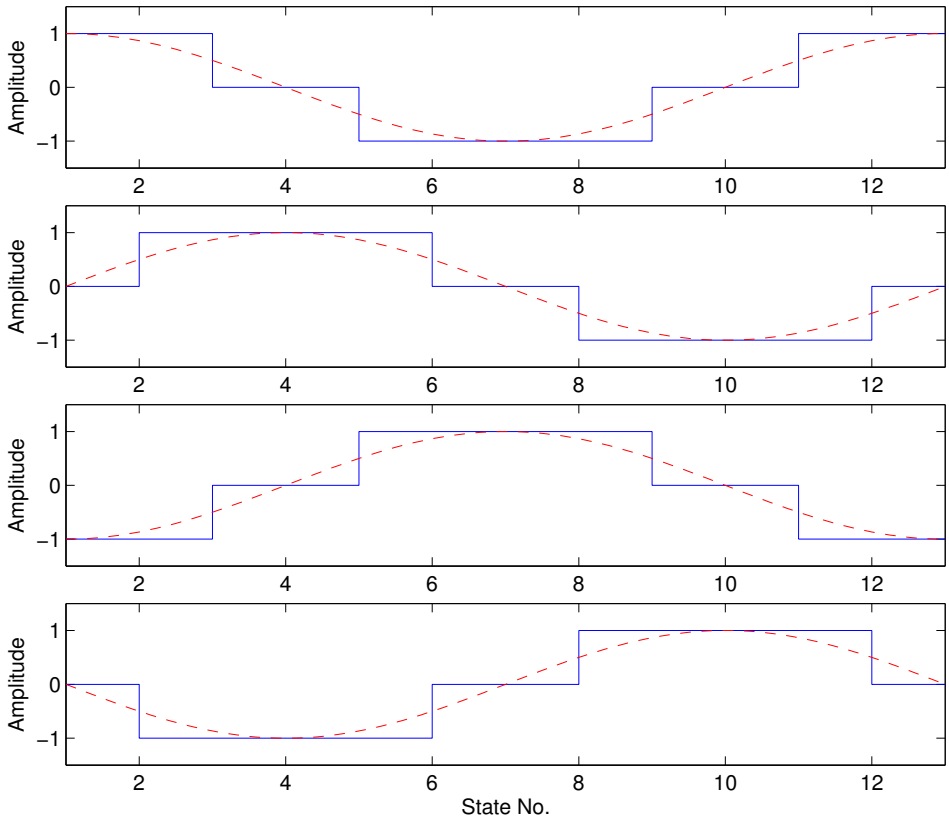

Figure 5.6: QPSK quasi-sine phases. The ideal sinusoidal signal is shown as a dashed line.

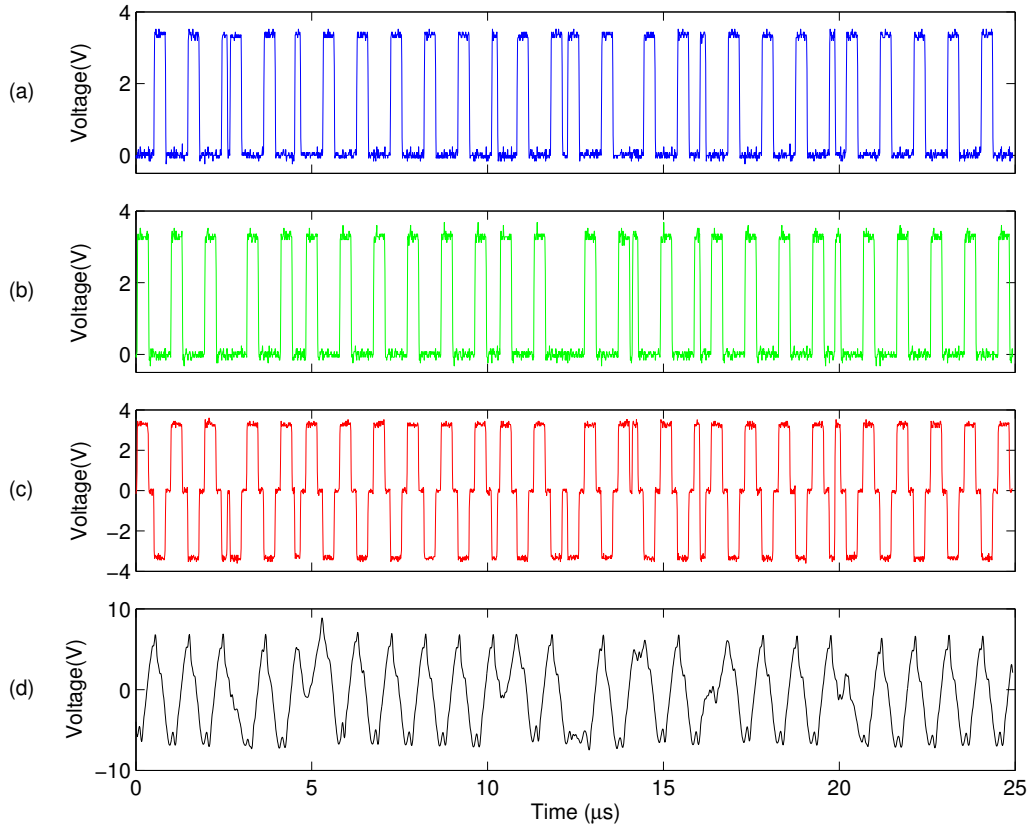

Figure 5.7: Signals for quasi-sine QPSK transmitter. (a) Control signal 1. (b) Control signal 2. (c) Quasi-sine output. (d) Coil voltage, 6V supply, measured as shown in Section 3.4.1 Fig. 3.6.

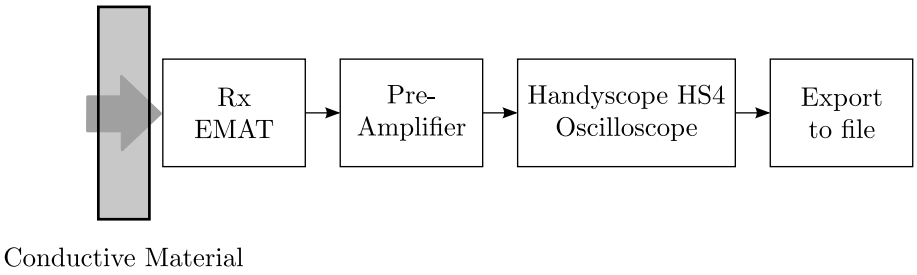

Figure 5.8: QPSK receiver for acoustic through metal communications.

A field programmable gate array (FPGA) is used to generate the 12-state quasi-sine wave, PSK modulated signal, which is output on two signal lines, as shown in Fig. 5.7a and Fig. 5.7b. These control signals switch a Class-D amplifier, which then drives either an EMAT or piezoelectric transducer. The resonant nature of the transducer means the quasi-sine is filtered to a close sine wave approximation as shown in Fig. 5.7d. The minimal complexity of this transmitter implementation is ideal for minimising the 'inside' electronics.

Although an FPGA was selected to generate the control signals, this may be replaced with any low cost microcontroller capable of switching digital I/O at a sufficiently high frequency.

The Spartan 3 demonstration board used in this implementation is clocked at 50MHz, which when divided down produces a 1.04166MHz centre frequency. As seen later, a sample rate conversion is performed prior to processing to ensure an integer number of samples per symbol.

An oscilloscope is used to measure the current draw of the amplifier by observing the voltage drop across a 1Ω resistor.

5.6.2 Receiver

A diagram illustrating the key features of the receiver hardware is shown in Fig. 5.8. An acoustic signal is detected by either an EMAT or piezoelectric transducer and amplified using the pre-amp design described in Section 3.4.2. The transmission is captured using a Handyscope HS4 USB digital oscilloscope at a sample rate, f_s = 5MHz, with 12-bit resolution. Once the transmission has completed, the packet is saved to file in preparation for off-line processing. Packets are limited to relatively short lengths due to the finite memory of the Handyscope.

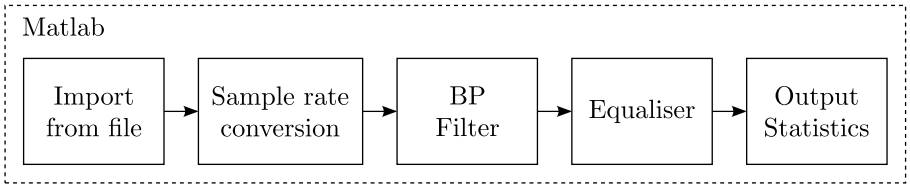

Figure 5.9: Off-line processing algorithm, implemented in Matlab, for demodulating and equalising acoustic through metal communications.

5.6.3 Off-line Processing

Once a packet is captured, it may be imported into Matlab for off-line processing. The general form of the demodulation algorithm is shown in Fig. 5.9, where BP filter denotes a bandpass filter. After a packet is imported, a sample rate conversion is performed to convert to $f_s = 5.2088$MHz (5 samples per cycle) and the packet is then subjected to high order digital filtering. The packet may now be demodulated using a variety of equaliser structures and the performance can be easily compared.

5.7 Experimental Results

In the following sections, equaliser structures are applied to demodulate packets of acoustic through-metal-telemetry, captured using the hardware described in Section 5.6. All transmissions use the parameters outlined in Table 5.3, unless otherwise stated.

The aim of this section is to determine a practical, power efficient receiver structure that translates well to a real-time hardware implementation.

5.7.1 System Channel Capacity

Using the hardware implementation described in Section 5.6, there is a limit on channel capacity imposed by: 1) the bandwidth of the transducers; 2) the background noise level of the receiver pre-amplifier; and 3) the maximum transmit signal power that avoids pre-amplifier saturation. Using the EMAT designs and circuitry described in Sections 3.3 and 3.4, the maximum achievable system SNR can be attained from 5.26, where $V_{\text{noise(RMS)}}$ is the root mean square (RMS) voltage of the background noise level at the receiver and $V_{\text{signal(RMS)}}$ is the RMS of the maximum received signal voltage. The background noise can be evaluated by digitally capturing a large period of data where no transmissions occur and then computing the

Table 5.3: Experimental system parameters.

Test Piece	25.4mm HY80 steel
Modulation	QPSK
Carrier Frequency, f_c	1 MHz
Sampling Frequency, f_s	5 MHz
Cycles per Symbol	2
Baud Rate	500 kHz
Bit Rate	1 Mbps
Training Sequence	500 Symbols (1000bit)
Data Length	3595 Symbols (7190bit)

RMS value of the data set. Assuming the transmitter is not power constrained, the maximum signal voltage at the receiver can be determined from the maximum output swing of the pre-amplifier minus the background noise level of the amplifier.

$$\text{SNR} = \frac{(V_{\text{signal(RMS)}})^2}{(V_{\text{noise(RMS)}})^2} \tag{5.26}$$

Experimental measurement shows the maximum achievable system SNR to be 100 (20dB), with a corresponding bandwidth of 350kHz at up to 1.6mm liftoff, hence, from (5.1), $C_c = 2.33$Mbps.

Referring back to Section 4.4.4 and Section 4.3, it is clear that the theoretical channel capacity greatly exceeds that of the Acoustic Gateway Demonstrator (50kbps) and the upper bound of multi-symbol burst mode techniques (350kbps).

It should be noted that the calculated channel capacity is not an absolute limit for acoustic through metal communications but rather the limit of this specific hardware setup.

5.7.2 No equalisation

As a reference test, a data packet was demodulated without equalisation, using a 2-tap filter to achieve symbol synchronisation. The packet is demodulated with 7dB SNR and 119/7190 bit errors, as shown in Fig. 5.10, which clearly illustrates the need for channel equalisation.

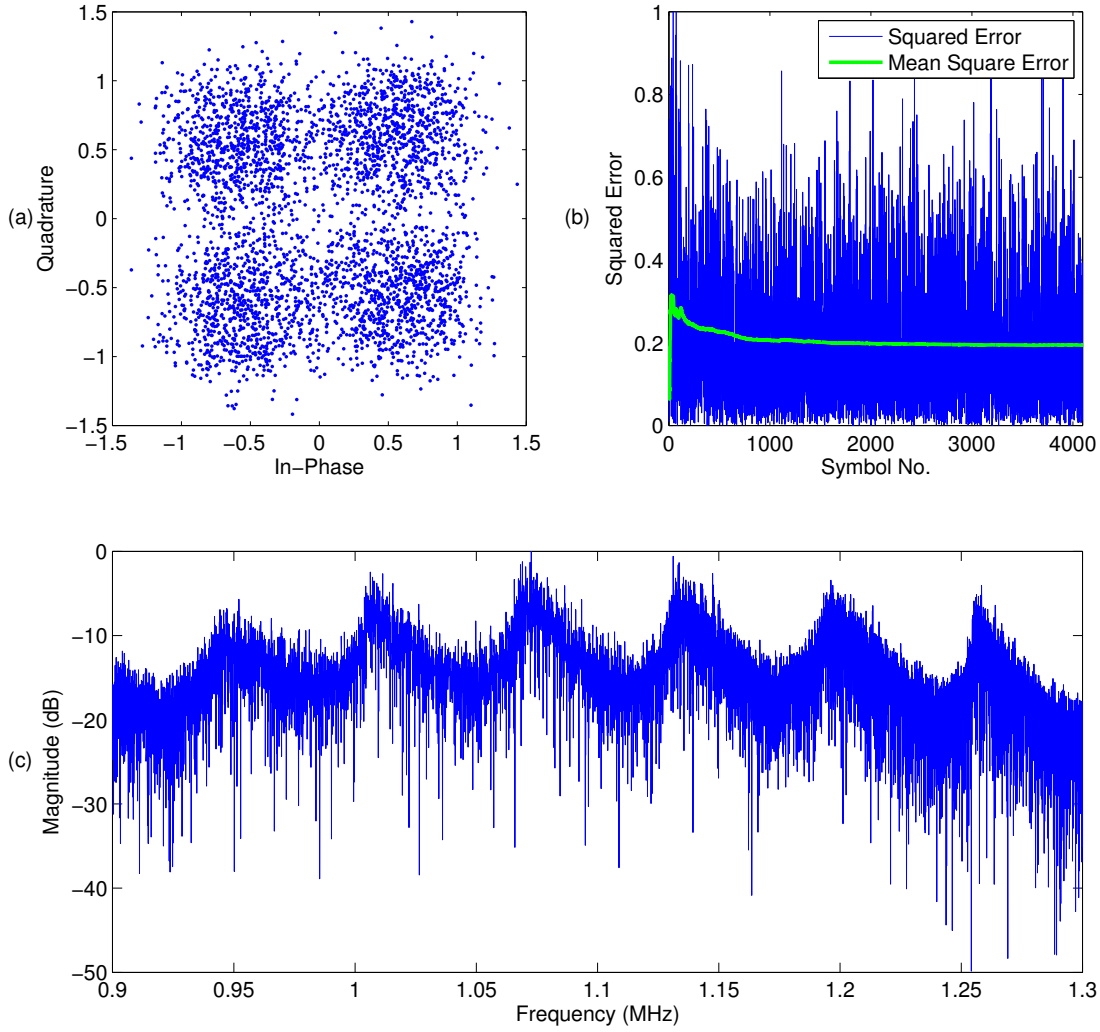

Figure 5.10: Graphical output for 1Mbps through 25.4mm HY80 with EMATs using a 2-tap LE, SNR = 7.2dB, 119/7190 bit errors. (a) I-Q plot. (b) Error plots. (c) Received signal spectrum.

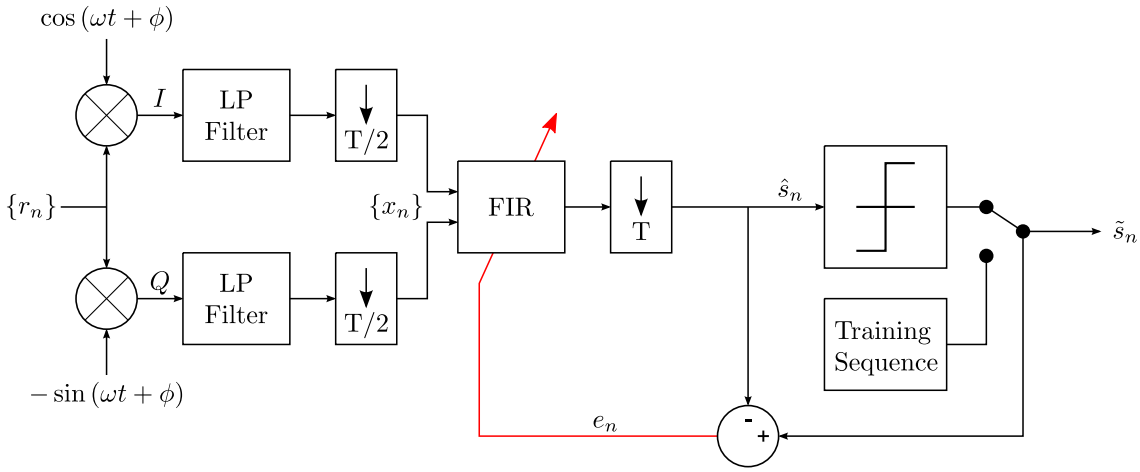

Figure 5.11: A complex baseband linear equaliser.

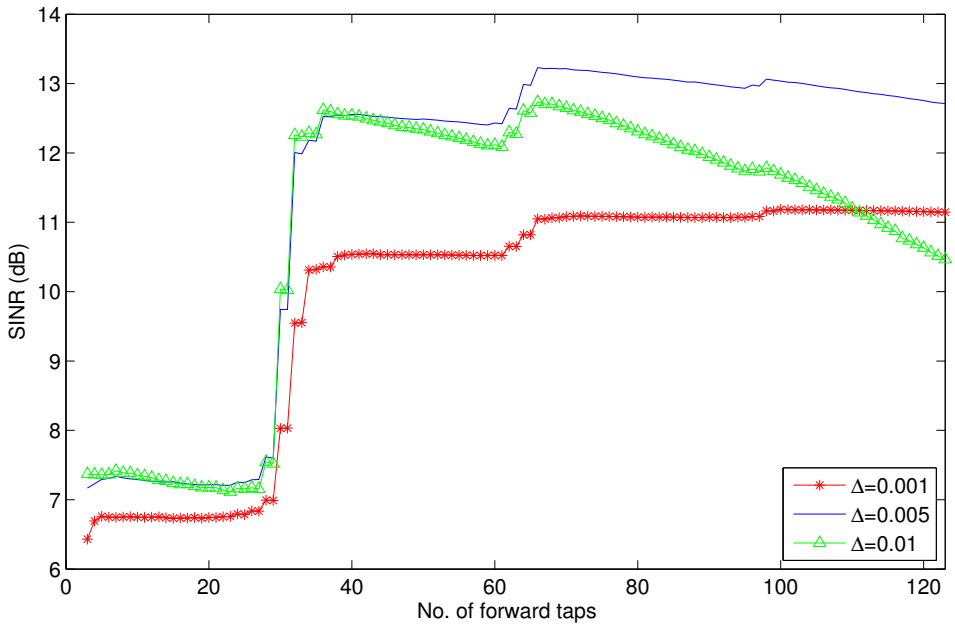

Figure 5.12: SNR variation due to the linear equaliser length and step size.

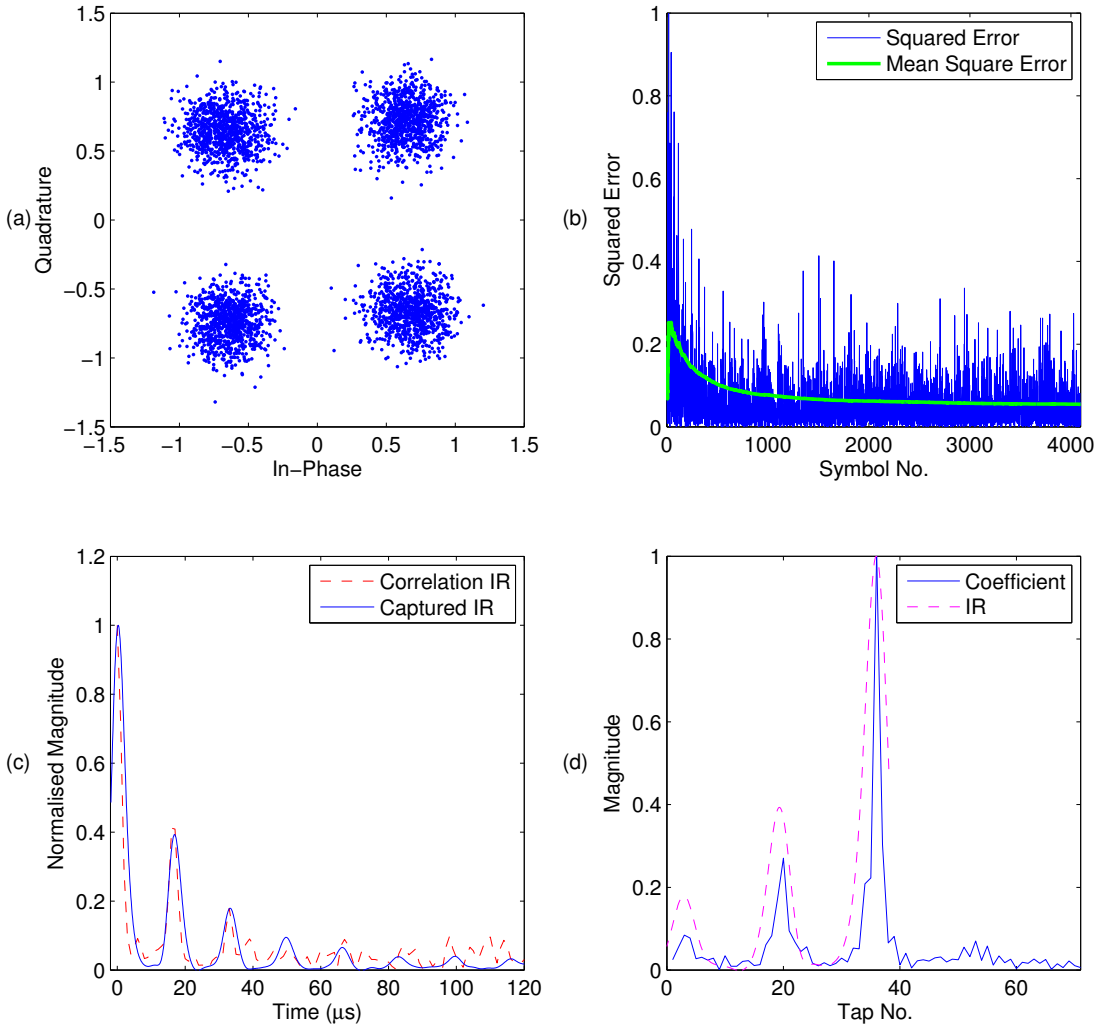

Figure 5.13: Graphical output for 1Mbps through 25.4mm HY80 with EMATs using a 71-tap LE, SNR = 13.2dB, 0/7190 bit errors. (a) I-Q plot. (b) Error plots. (c) Impulse response. (d) Tap coefficients.

5.7.3 Linear Equaliser

The first structure to be tested is a $\frac{T}{2}$-spaced LE using the LMS update algorithm, shown in Fig. 5.11. An LMS-linear equaliser has has only two variables, the filter length, L, and the step size, Δ, both of which have a significant influence on the equaliser performance.

The plot shown in Fig. 5.12 demonstrates the output SNR as a function of filter length and step size. The graphical output of a single result, demonstrating the performance of a 71-tap equaliser on a 25.4mm steel test block, is shown in Fig. 5.13.

With less than 29 taps, the performance of the LE is very poor, achieving approximately 7dB. Due to the $\frac{T}{2}$ spacing, a 29-tap equaliser spans 7 precursor symbols and, consequently, cannot combat the primary, or subsequent, multipath arrivals, which begin after an 8 symbol ($16\mu s$) delay, as shown by the channel impulse response in Fig. 5.13c. When the filter length is increased to 41 taps, the primary multipath arrival is encompassed within the filter span and a $>$ 5dB improvement in SNR results, with the corresponding selection of an appropriate step size.

A 71-tap and 101-tap equaliser encompass upto the second and third multipath arrivals respectively, and result in small positive increases in SNR relative to the immediately preceding values. The decaying nature of the multipath amplitude means that although large gains are achieved by spanning the first and second arrivals, by the third arrival the gain is negated by the increase in noise enhancement.

The best result is achieved using a 71-tap equaliser ($\Delta = 0.005$) as shown in Fig. 5.13.

5.7.4 Decision Feedback Equaliser

The DFE has been shown to give superior performance to the LE when a channel exhibits deep spectral fades [88]. The implemented DFE structure is shown in Fig. 5.14, employing a $\frac{T}{2}$-spaced forward equaliser and symbol spaced feedback filter. Consequently, a DFE has four variables when using the LMS update algorithm, a filter length and step size, for both the forward and feedback filters. The update equations for the forward filter coefficients, $\mathbf{w}^{\mathrm{fw}}$, and feedback filter coefficients, $\mathbf{w}^{\mathrm{bk}}$, are given in (5.27) and (5.28) respectively.

$$\mathbf{w}_{n+1}^{\mathrm{fw}} = \mathbf{w}_{n}^{\mathrm{fw}} + \Delta_1 e_n^* \mathbf{x}_n \tag{5.27}$$

$$\mathbf{w}_{n+1}^{\mathrm{bk}} = \mathbf{w}_{n}^{\mathrm{bk}} - \Delta_2 e_n^* \tilde{\mathbf{s}}_n \tag{5.28}$$

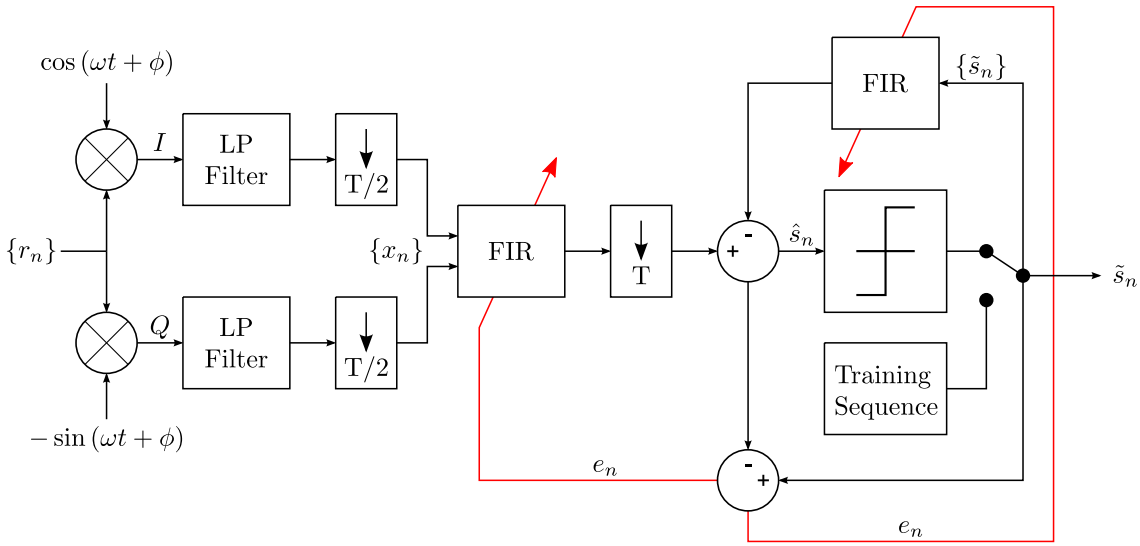

Figure 5.14: A complex baseband decision feedback equaliser.

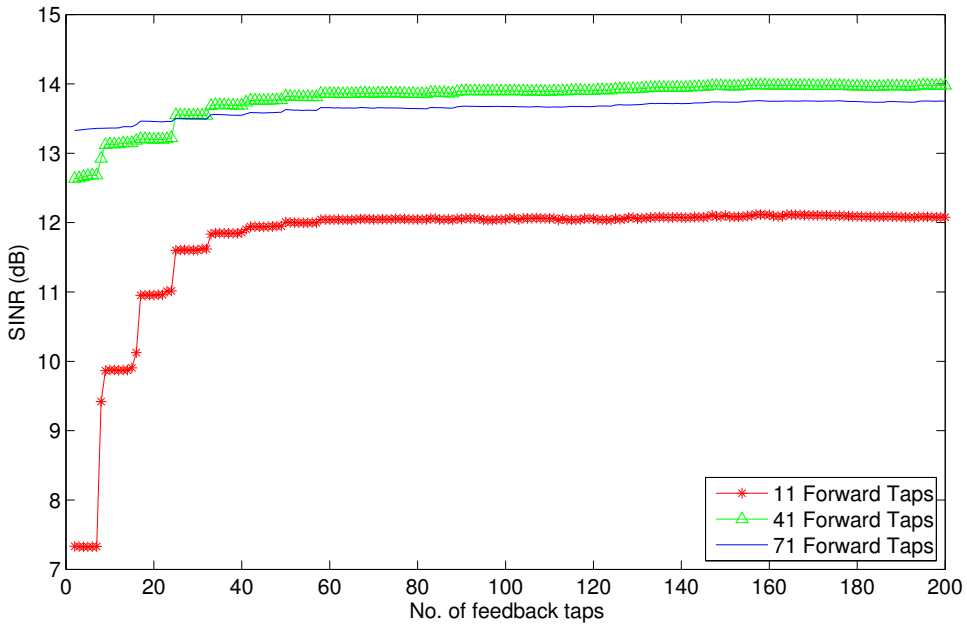

Figure 5.15: SNR variation due to the length of the DFE feedback filter, for three different forward filter lengths.

The performance of the DFE is shown in Fig. 5.15 for varying feedback filter length, with three different forward filter lengths: 11-taps, which spans no multipath arrivals; 41-taps, which spans the first multipath arrival; and 71-taps, which spans the first and second multipath arrivals.

For the case of an 11-tap forward filter, all ISI cancellation must be accomplished by the feedback filter. With fewer than 8 feedback taps, the feedback filter cannot cancel any ISI contributions and subsequently, provides no SNR gain. Increasing the length to 9 taps, the filter can cancel the primary multipath arrival and a 3dB SNR increase results. For every subsequent 8 taps, the filter spans an additional multipath arrival and provides small SNR gains up to a length $\approx$ 60 taps, beyond which, ISI contributions are sufficiently small such that no further gains can be achieved by increasing the filter length. The graphical output of a single packet demodulation, demonstrating the performance of an 11-forward-tap, 60-feedback-tap DFE on a 25.4mm steel test block, is shown in Fig. 5.16.

Comparison with previous results shows that the classical DFE achieves $\approx$ 12dB SNR using a total of 71 taps whereas the LE achieves $\approx$ 1dB better using an equivalent number of taps.

A DFE with 41 forward taps and 60 feedback taps, operating in full decision directed mode, achieves the highest SNR; almost 14dB, as shown in Fig. 5.17. The 41 forward taps only span the primary multipath, yet the feedback taps of the DFE clearly show that the forward filter has achieved partial cancellation of the 2nd and subsequent multipath arrivals.

An LE outperforming a DFE when a channel exhibits the fades shown in Fig. 5.10c is an unexpected result. Likewise, a filter should not be able to partially cancel multipath beyond the span of the filter.

These phenomena are explored with the aid of simulation in Section 5.8, where it is shown that the LE performance is only achievable for the special case of the standard metal wall impulse response, i.e. where the multipath is both decaying and periodic. Hence, a DFE is the preferred structure for a general solution.

5.7.4.1 Static Feedback Taps

Most applications involving through metal communications will have a static channel for the duration of a data packet transmission. Hence, significant power savings can be made by ceasing the coefficient update process post training sequence. Depending on the application, it may be possible to operate with the same fixed feedback coefficients for several packets and only retrain periodically.

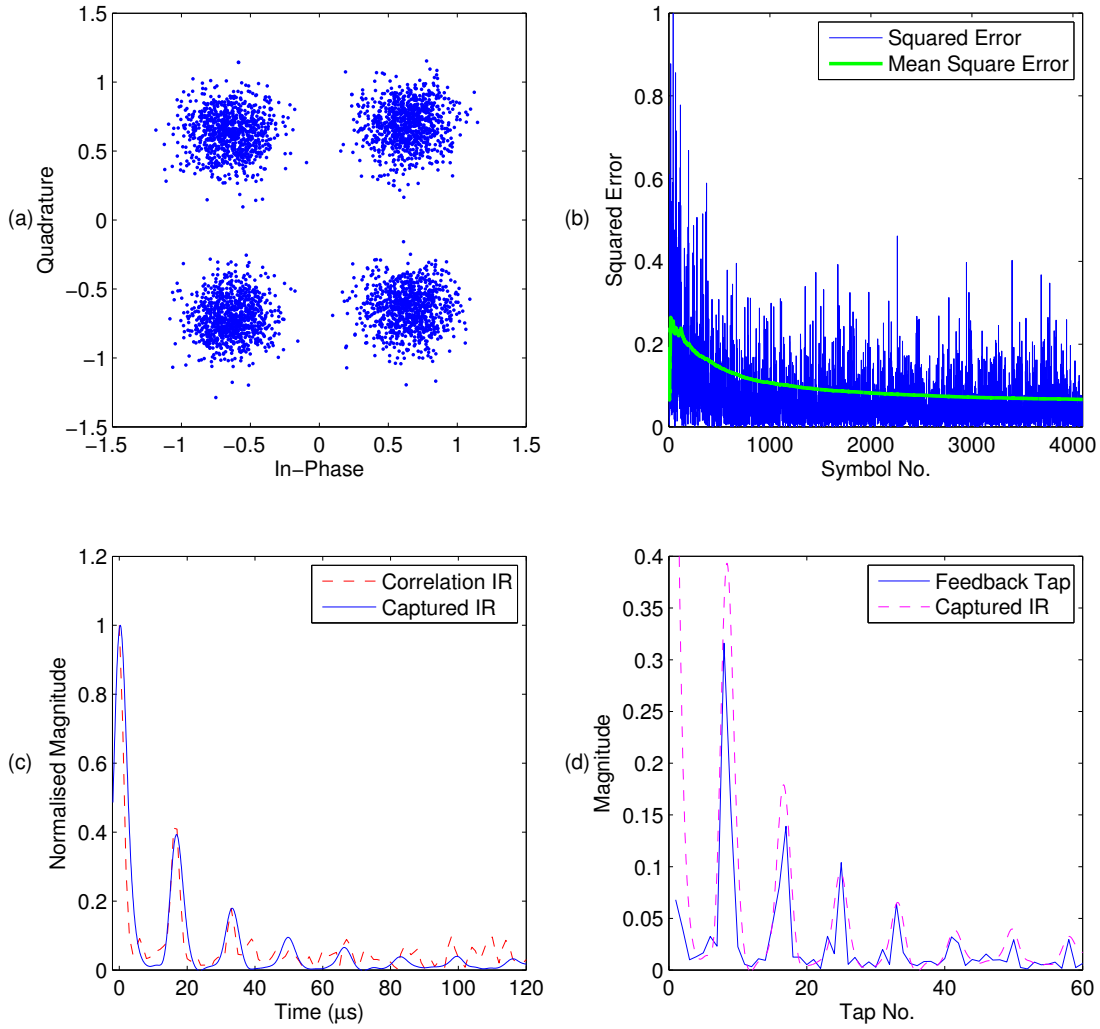

Figure 5.16: Graphical output for 1Mbps through 25.4mm HY80 with EMATs using a DFE with 11 forward taps and 60 feedback taps, SNR = 12.57dB, 0/7190 bit errors. (a) I-Q plot. (b) Error plots. (c) Impulse response. (d) Feedback tap coefficients.

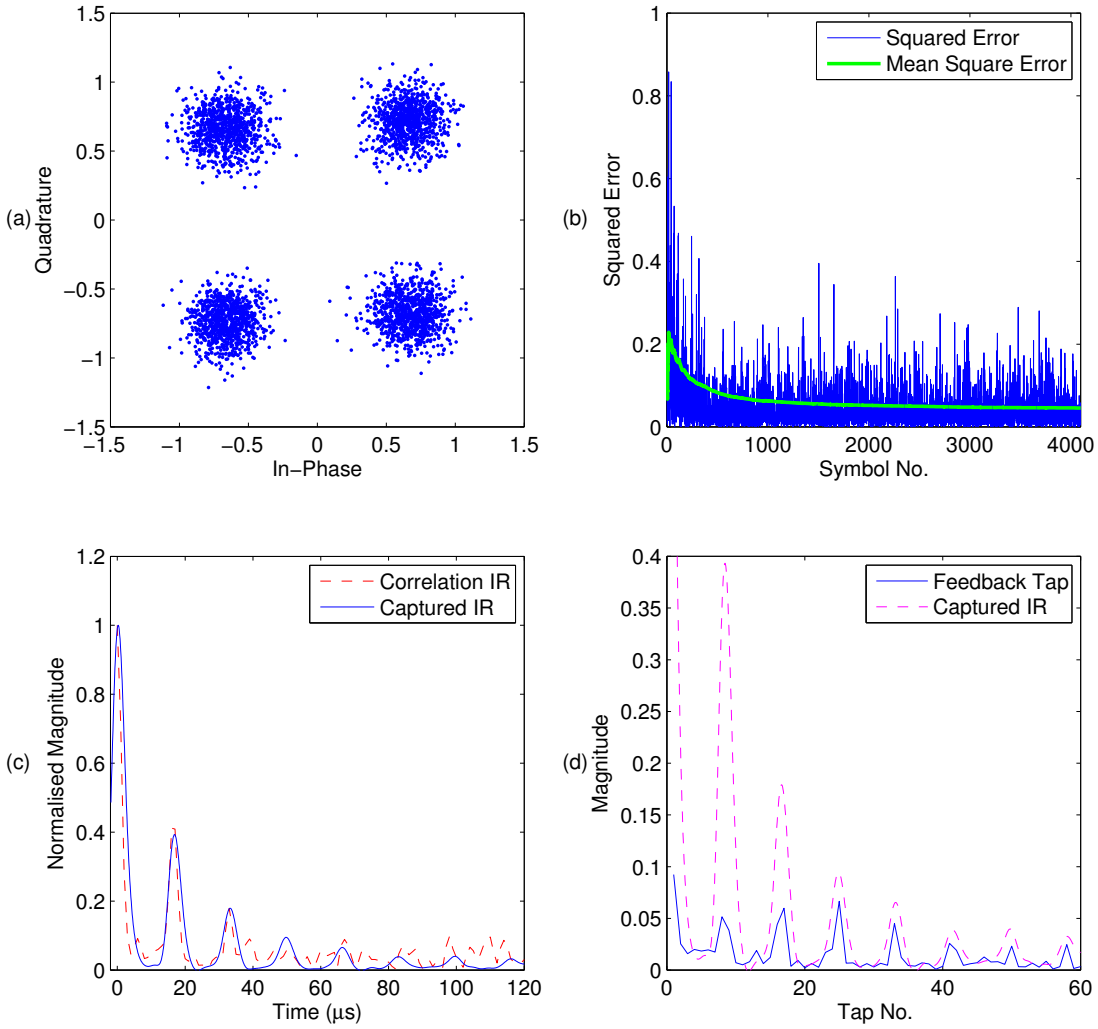

Figure 5.17: Graphical output for 1Mbps through 25.4mm HY80 with EMATs using a DFE with 41 forward taps and 60 feedback taps, SNR = 13.9dB, 0/7190 bit errors. (a) I-Q plot. (b) Error plots. (c) Impulse response. (d) Feedback tap coefficients.

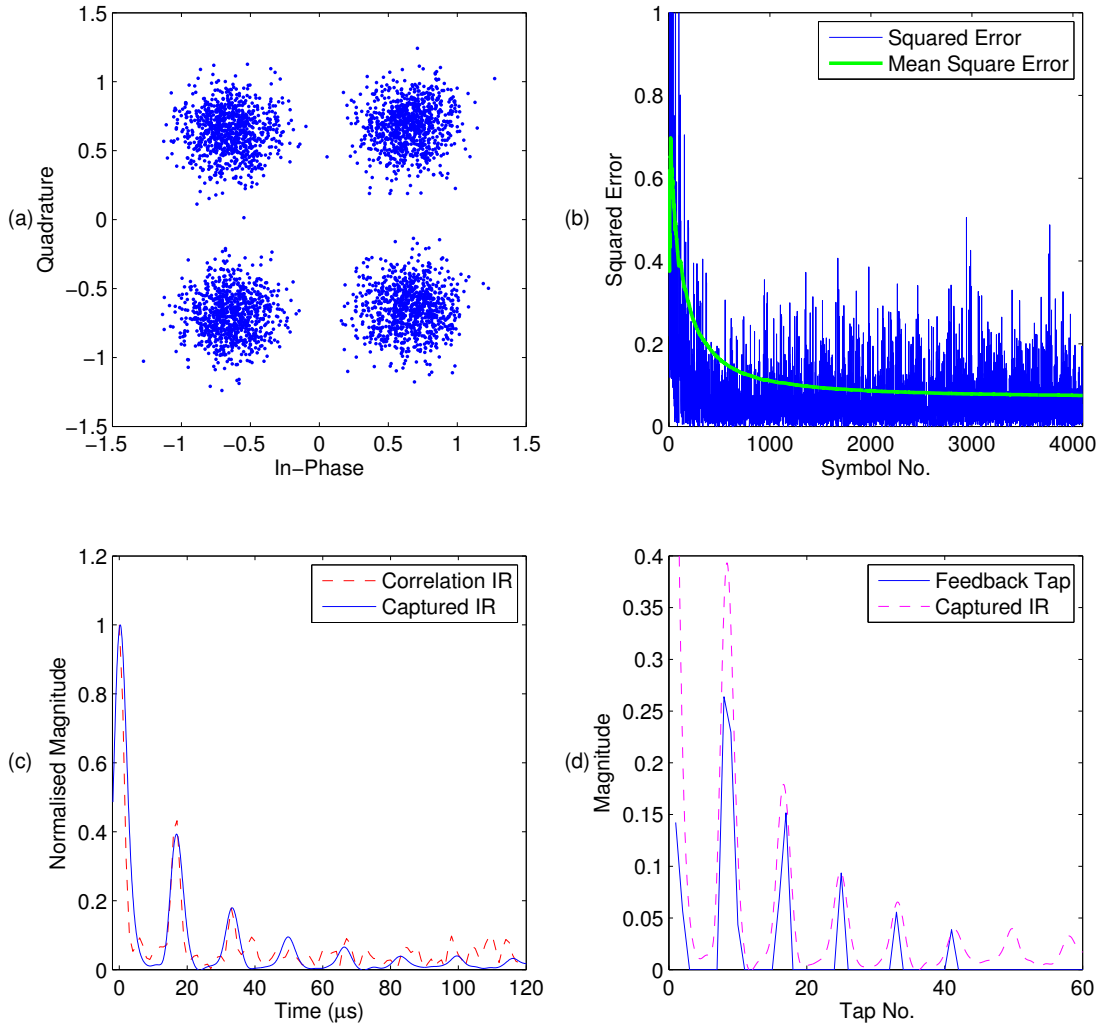

Figure 5.18: Graphical output for 1Mbps through 25.4mm HY80 with EMATs using a DFE with 11 forward taps and 10 static sparse feedback taps, SNR = 12.05dB, 0/7190 bit errors. (a) I-Q plot. (b) Error plots. (c) Impulse response. (d) Feedback tap coefficients.

5.7.4.2 Sparse Equalisation

As discussed in Section 4.1.3, the standard impulse response of a metal wall channel, when using non-contact transducers, has a constant duration regardless of the metal thickness, but the number of multipath arrivals occurring within the impulse response will decrease with an increasing wall thickness. In other words, for thicker metal walls, the impulse response becomes increasingly sparse.

This property can be exploited by sparse equalisation, i.e. once the DFE is trained, all coefficients below a threshold are assumed to be zero and are not evaluated, significantly reducing the number of operations required during demodulation. Consequently, a DFE feedback filter spanning the entire multipath duration can be achieved with a fraction of the taps.

A spot result, demonstrating the performance of a DFE when a combination of static feedback taps and sparse equalisation are used, is shown in Fig. 5.18. Using only 10 static sparse taps in place of a full 60 tap feedback filter for a 25.4mm channel results in a mere 0.5dB SNR drop.

5.7.5 Transducer Power Comparison

It is widely accepted that piezoelectric transducers are far more efficient than EMATs. In this section, a direct comparison is performed between the two transducer types, to determine their power requirements to achieve 1Mbps communications through a 25.4mm steel wall at a bit error rate (BER) of 10^{-2} uncoded using equivalent transmit and receive hardware. This BER represents an acceptable level for modern forward error correction (FEC), such as convolutional or turbo codes. Satisfactory BER performance of 10^{-6} should be achievable after coding at the expense of $10 - 15\%$ overhead [99].

The result for the EMAT system is shown in Fig. 5.19, requiring 269mW to achieve the specified BER of approximately 10^{-2}, with minimal liftoff. The SNR at this power level is 10.4dB, giving a theoretical channel capacity, C_c, of 1.25Mbps from (5.1). After accounting for FEC overheads, the effective throughput of the system would be approximately 900kbps.

To achieve the required BER with piezoelectric transducers requires significantly less power under ideal coupling conditions, only 2mW, as shown in Fig. 5.20. The feedback coefficients take the form of the piezo impulse response, as shown in Fig. 5.20d, although it is not as distinctive as that of the EMAT due to the reduced amplitude of the multipath arrivals.

As a final comparison, a liftoff of 0.8mm was introduced to the EMAT test setup for both the transmitter and receiver. This represents the situation of a wall with a thick

Table 5.4: Transducer power requirement summary.

Transducer	Liftoff (mm)	Power (mW)
Piezoelectric	0	2
EMAT	< 0.2	269
EMAT	0.8	1230

surface coating, a scenario impractical for piezoelectrics. The power requirement for this setup to achieve a 10^{-2} BER is 1.23W, a factor of 5 increase from the minimal liftoff case. A summary of the power consumption results are shown in Table 5.4.

5.8 LE vs DFE Simulation Results

It was shown in Section 5.7.4 that an experimentally captured, through metal acoustic transmission could be demodulated with higher SNR using an LE compared to the DFE. Furthermore, it was shown that an LE was capable of partially cancelling multipath beyond the time span of the filter, provided it encompassed the primary arrival. This behaviour is explored with the aid of Matlab simulation.

The channel impulse response used for the purpose of simulation is a simplified approximation of the impulse response of the 25.4mm steel test block used for experimental testing, as shown in Fig. 5.21. The multipath is both periodic and exponentially decaying in amplitude.

The performance of a 41-tap $\frac{T}{2}$-spaced LE (10 precursor symbol span) and an 11 forward tap, 60 feedback tap DFE (60 precursor symbol span), for this simulated channel, is equal, to within a few fractions of a decibel. However, Fig. 5.22 demonstrates the performance variation for the LE and DFE when the primary multipath is shifted to each symbol position within the 'Shift' region in Fig. 5.21. A positive shift takes the primary arrival beyond the span of the LE and results in a $\approx$ 5dB performance penalty. A negative shift keeps the primary arrival within the span of the LE, however, a $\approx$ 3dB penalty still results.

Clearly, the LE outperforming, or matching, the DFE is a consequence of the special case of channel periodicity. The primary arrival results in fades at intervals of $\frac{1}{T}$, and subsequent arrivals result in fades at intervals of $\frac{1}{2T}$, $\frac{1}{3T}$ etc. Hence, by equalising the primary arrival, the LE also partially equalises fades resulting from subsequent arrivals and consequently a large SNR gain results.

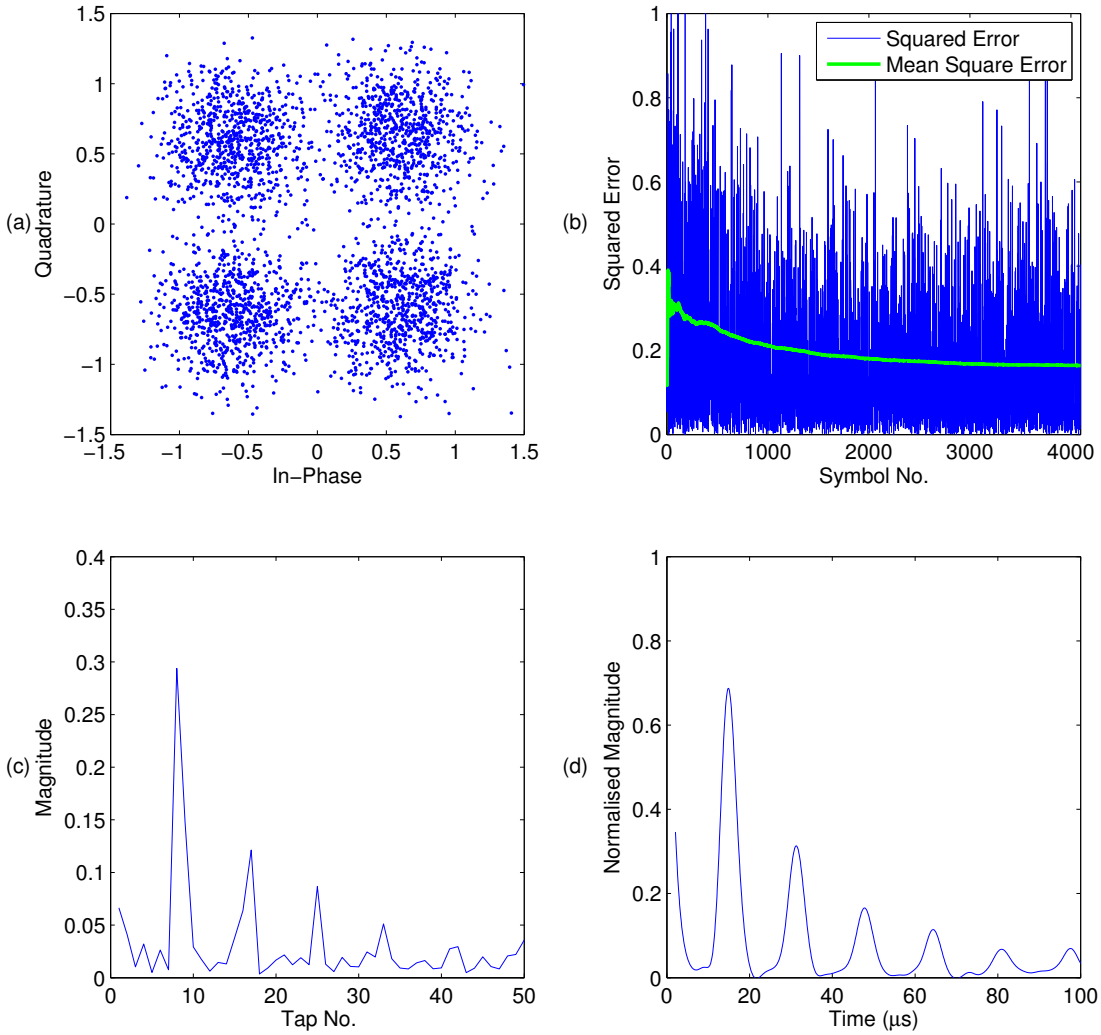

Figure 5.19: Graphical output for 1Mbps through 25.4mm HY80 with EMATs at minimal liftoff, SNR = 8.3dB, 61/6190 bit errors, input power 269mW. (a) I-Q plot. (b) Squared error curve. (c) Feedback coefficients. (d) Impulse response envelope.

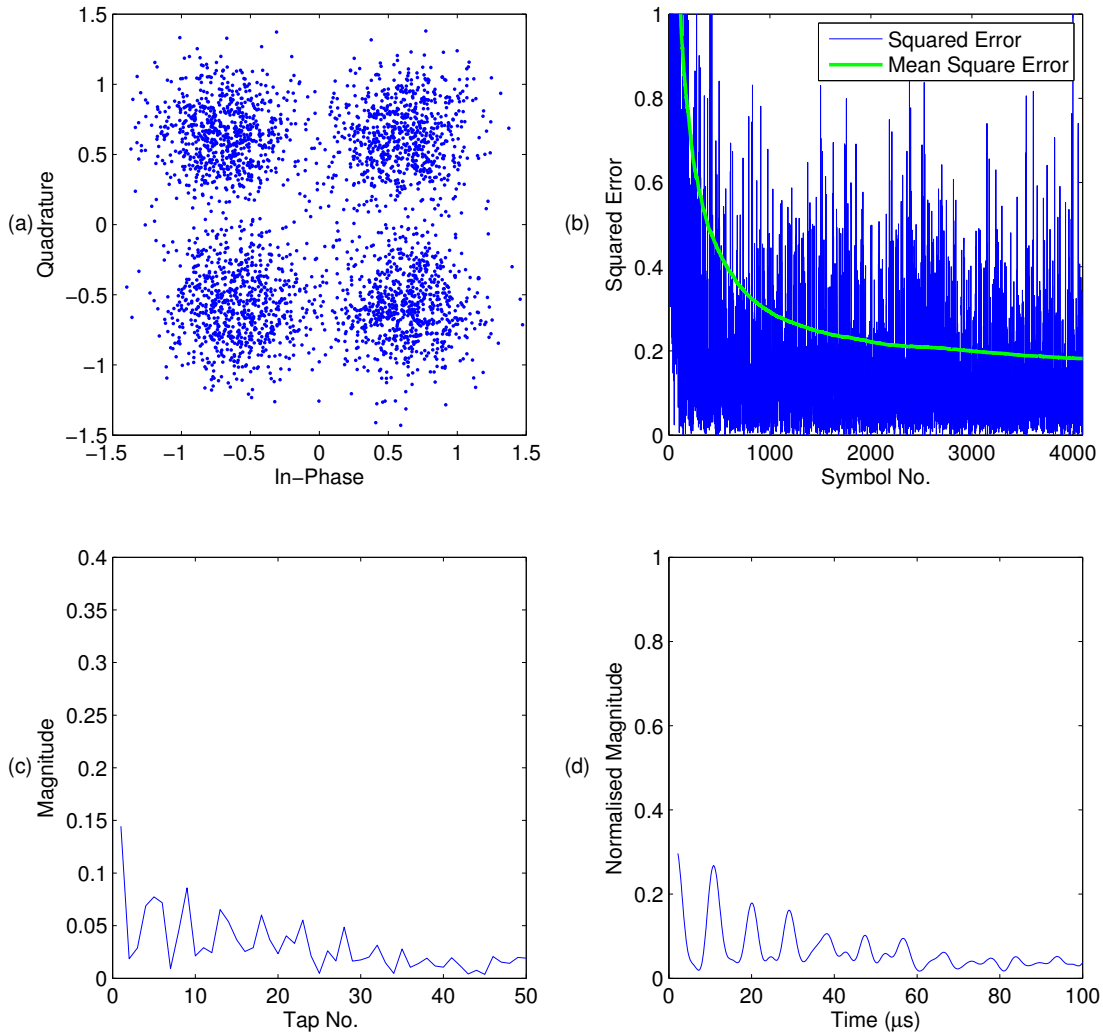

Figure 5.20: Graphical output for 1Mbps through 25.4mm HY80 with well coupled piezoelectric transducers, SNR = 8.3dB, 60/6190 bit errors, input power 2mW. (a) I-Q plot. (b) Squared error curve. (c) Feedback coefficients. (d) Impulse response envelope.

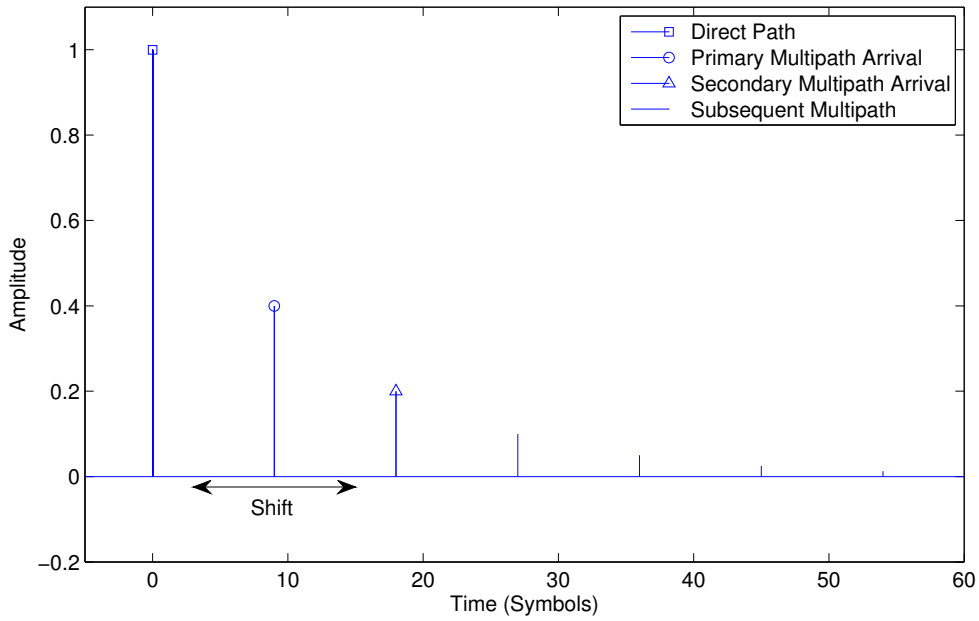

Figure 5.21: Impulse response of a simulated, periodic multipath channel. 'Shift' indicates the range over which the primary multipath arrival is shifted during performance simulations.

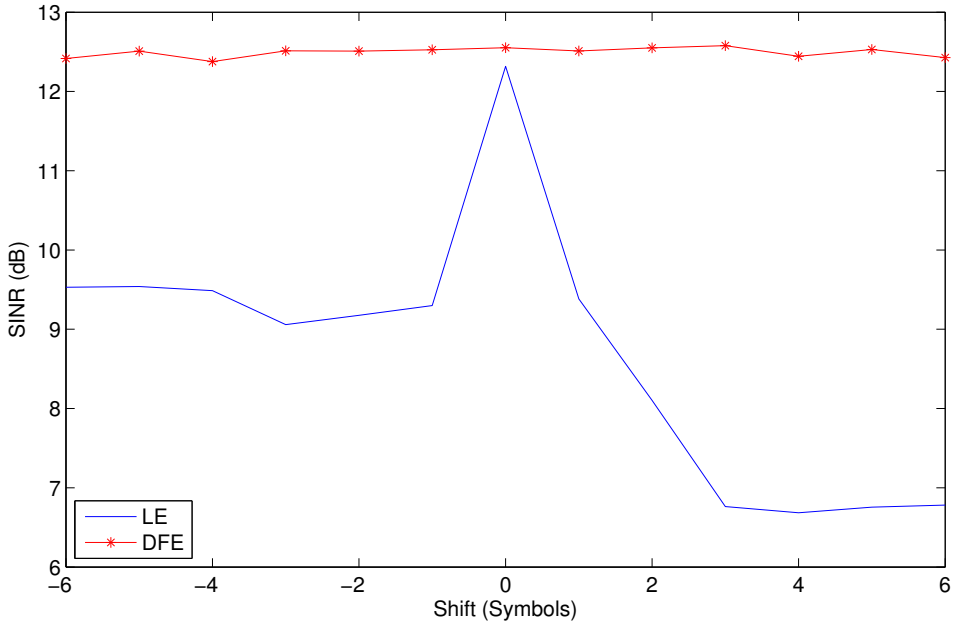

Figure 5.22: Performance comparison of an LE and DFE for a simulated channel with varying primary multipath delay.

5.9 Real-Time Receiver

A key area of further work is the conversion of the 'off-line' Matlab processing algorithm into a hardware receiver. This algorithm can be implemented in real-time using a digital signal processor (DSP), which can perform fast multiply-accumulate operations to efficiently implement FIR filters. For a general solution, a DFE is the preferred receiver structure due to the consistent performance irrespective of channel response.

The complexity and cost of the receiver can be minimised if the quasi-static nature of the channel is exploited, i.e. the filter coefficients are updated periodically, only every few minutes. The processing requirements of the implementation can be reduced as follows:

i. The outside unit requests a training sequence from the inside unit, which is acquired and stored in memory.

ii. A relatively low cost, low power microprocessor processes this training data off-line, i.e not real time, to calculate the optimal DFE coefficients, which may be sparse depending on the channel.

iii. The coefficients are passed to a modest complexity programmable logic device which implements the real time equalisation and demodulation of the incoming data until the next training event.

An elegant solution may also incorporate additional intelligence to exploit the special case of improved LE performance when the channel exhibits periodic multipath. For a thin metal wall, the channel impulse response will not be sparse and hence, a DFE would require a fully populated feedback filter. In contrast, a relatively short LE can achieve similar performance with reduced computation.

5.10 Summary

This chapter has presented alternative modulation schemes which are capable of data rates far exceeding what is achievable with burst mode transmission. Single carrier QPSK is preferred to higher order or multi-carrier schemes because it allows the transmitter electronics to be greatly simplified. Equalisation is required to overcome the multipath induced fading and ISI associated with continuous wave single carrier transmission. The DFE is shown to be adept at mitigating the effects of ISI regardless of the channel impulse response. Hardware experimentation has shown data rates in excess of 1Mbps to be achievable using this technique. The power

consumption of a real time implementation can be minimised by exploiting the quasi-static nature of a metal wall channel and freezing the feedback tap coefficients post training sequence. Further savings can be made for the standard impulse response case by utilising sparse equalisation.

Chapter 6

Power Delivery

Extracting information from a sensor located within a sealed metal container or structure requires power. If the status of the contents is of interest, then it is likely that the content is hazardous or needs to remain isolated from the outside world for other reasons and therefore, opening such a container to periodically change batteries is highly impractical.

If the 'inside' is energy rich, due to heat or radiation, then energy scavenging may be feasible for some applications [100–102]. A more elegant and general solution is through metal power delivery, whereby power is transferred from 'outside' to 'inside' in order to power a sensor and communication device. This sort of asymmetric arrangement has been referred to previously as Scenario A.

In previous chapters, the combination of EMATs and multipath tolerant receiver structures have been shown to provide an effective solution for robust through metal communications. Furthermore, the design process focussed on minimising the complexity of the 'inside' transmitter electronics for this sort of application.

The robustness of an EMAT based system is due to the insensitivity to surface coupling and, to maintain this functionality, *a non-contact means of power delivery is essential*. Unfortunately, the relatively low transduction efficiency of an EMAT means that it is unsuitable for power delivery.

This chapter explores the use of inductive power transfer for through metal power delivery by analytical, finite-element and experimental means, with the aim of determining the achievable transfer efficiency. Consideration is also given to the feasibility of inductive data communications for very low data rate applications.

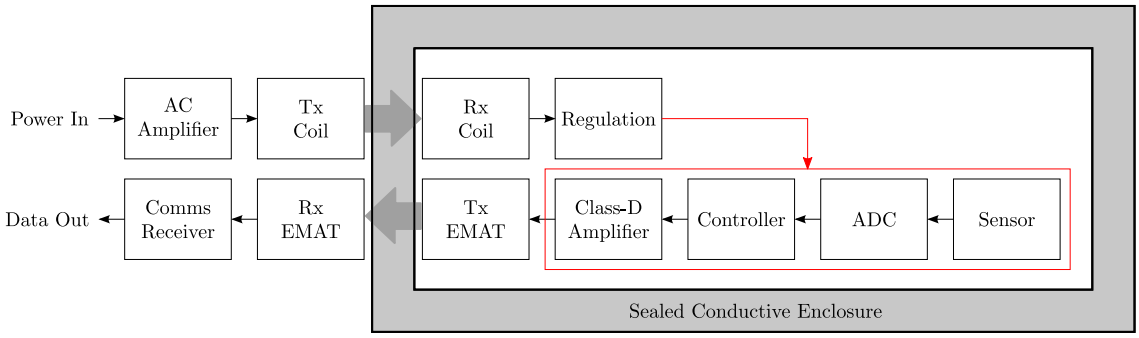

Figure 6.1: A non-contact, through metal communications and power delivery system.

6.1 Inductive Power Transfer

Inductive power transfer (IPT) is an increasingly popular solution for systems where short range, non-contact power delivery is desirable, with applications including powering vehicles [49, 103, 104], charging mobile electronic devices [105–107] and transcutaneously powering medical implants [108, 109].

Typically, each system is designed to optimise a specific metric, such as maximum power delivery, alignment sensitivity or minimal coil dimensions. No previous study has attempted to optimise system parameters for maximum power transfer efficiency through a metal channel. For comparison, it is worth noting that efficiencies of up to 82% have been achieved at distances up to 15mm through air, using an operational frequency of 20kHz [49].

The proposed system is shown in Fig. 6.1, utilising IPT for power delivery and acoustics for data communication. The following subsections will focus on the inductive link, specifically the achievable transfer efficiency. Initial analysis of the problem is performed using an analytical equivalent circuit model.

6.1.1 Analytical Model

An inductive power transfer system can be analysed by means of an equivalent circuit and a mutual inductance model, as shown in Fig. 6.2. The coils are represented by an inductance, L, and series resistance, R, with the subscripts tx and rx used to denote transmitter and receiver components respectively. It is typical to operate an IPT system at a single frequency and hence, it is advantageous to tune the transmit and receive coils to resonance with capacitors C_{tx} and C_{rx} respectively. For simplicity, only a series-series capacitively tuned system is considered, although other topologies are possible. To further simplify analysis, the system is assumed to

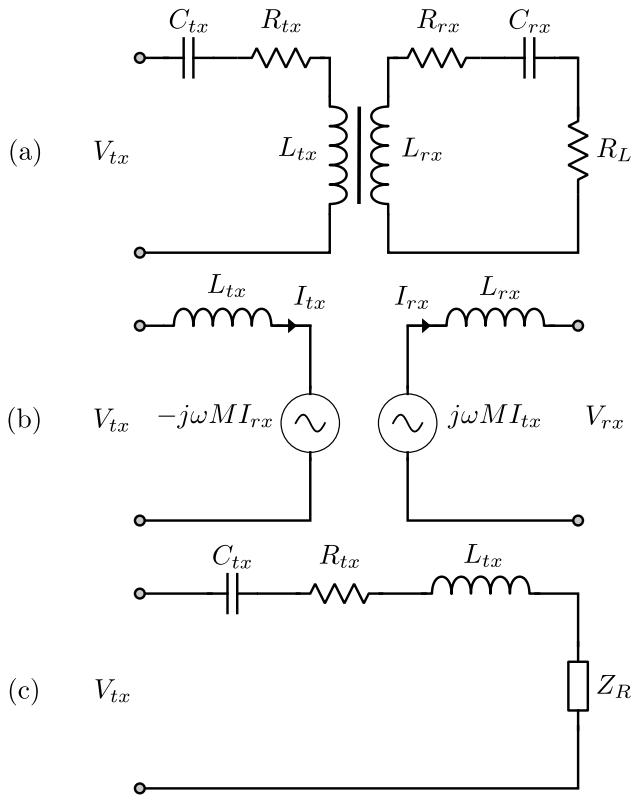

Figure 6.2: IPT models. (a) Equivalent circuit. (b) Mutual inductance model. (c) Reflected load of the receiver as seen by the transmitter.

deliver power to a load resistance, R_L, where in practice this would be some form of power conditioning circuit.

The efficiency of the system, η, is the fraction of the total power in, P_{in}, which is converted to useful output power P_{out}. The overall efficiency can be determined by considering the efficiency of the transmitter, η_{tx}, and receiver, η_{rx} (6.1) [110]. This can also be expressed in terms of a loss factor, λ_l [105].

$$\eta = \frac{P_{\text{out}}}{P_{\text{in}}} = \eta_{tx}\eta_{rx} = \frac{1}{1+\lambda_l} \tag{6.1}$$

To determine the efficiency of the transmitter, it is necessary to reflect the circuit elements of the receiver side to the transmit side using (6.2), where Z_R is the reflected impedance, M is the mutual inductance between the coils, ω is the angular frequency and Z_{rx} is the impedance of the rx circuit [111]. When the receiver is tuned to series resonance (6.3), the reflected impedance, Z_R, becomes purely resistive. The resonant frequency is denoted by ω_s.

$$Z_R = \frac{\omega^2 M^2}{Z_{rx}} \tag{6.2}$$

$$\omega_s = \frac{1}{\sqrt{LC}} \tag{6.3}$$

The efficiency of the transmitter is the fraction of the total input power delivered to Z_R (6.4). Similarly, receiver efficiency is the fraction of receiver input power delivered to R_L (6.5).

$$\eta_{tx} = \frac{Z_R}{Z_R + R_{tx}} = \frac{1}{1 + \frac{R_{tx}(R_L + R_{rx})}{\omega_s^2 M^2}} \tag{6.4}$$

$$\eta_{rx} = \frac{R_L}{R_L + R_{rx}} = \frac{1}{1 + \frac{R_{rx}}{R_L}} \tag{6.5}$$

Manipulating the product of the transmitter and receiver efficiencies gives an expression for the overall system efficiency (6.6) as well as the system loss factor (6.7).

$$\eta = \frac{1}{1 + \frac{R_{tx}(R_L + R_{rx})}{\omega_s^2 M^2} + \frac{R_{rx}}{R_L} + \frac{R_{tx} R_{rx}(R_L + R_{rx})}{R_L \omega_s^2 M^2}} \tag{6.6}$$

$$\lambda_l = \frac{R_{tx}(R_L + R_{rx})}{\omega_s^2 M^2} + \frac{R_{rx}}{R_L} + \frac{R_{tx} R_{rx}(R_L + R_{rx})}{R_L \omega_s^2 M^2} \tag{6.7}$$

From (6.6), it is now apparent that the efficiency of an IPT system is dependent on the load resistance, R_L. To achieve maximum efficiency for a given system, it is therefore necessary to determine the optimal value for R_L, $R_{L_{\text{opt}}}$. This may be achieved by differentiating λ_l with respect to R_L (6.8).

$$R_{L_{\text{opt}}} = R_{rx} \sqrt{\frac{\omega_s^2 M^2}{R_{tx} R_{rx}} + 1} \tag{6.8}$$

Making the substitutions given in (6.9) allows for a more intuitive evaluation of (6.8), where k is the coupling coefficient, and Q_{tx} and Q_{rx} are the quality factors of the transmit and receive coils respectively. The new expression is given in (6.10).

$$M = k\sqrt{L_{tx} L_{rx}}, \qquad Q_{tx} = \frac{\omega_s L_{tx}}{R_{tx}}, \qquad Q_{rx} = \frac{\omega_s L_{rx}}{R_{rx}} \tag{6.9}$$

$$R_{L_{\text{opt}}} = R_{rx} \sqrt{k^2 Q_{tx} Q_{rx} + 1} \tag{6.10}$$

A further approximation can be made, due to the unique properties of a metal wall channel. The shielding effect of a metal wall will severely reduce the coupling

coefficient and the proximity effect will limit the quality factor of the coils and consequently, the product $k^2Q_{tx}Qrx$ will be small.

$$\lim_{k^2Q_{tx}Q_{rx}\to 0} R_{rx}\sqrt{k^2Q_{tx}Q_{rx}+1} = R_{rx}$$
$$\therefore R_{L_{\text{opt}}} = R_{rx} \tag{6.11}$$

Hence, matching the load resistance, R_L, to the receive coil resistance, R_{rx}, represents a very good approximation to the optimal value for a loosely coupled (low k) IPT system for through metal applications (6.11). Using this approximation, the efficiency of the system then simplifies to (6.12).

$$\eta = \frac{1}{2+\frac{4R_{tx}R_{rx}}{\omega_s^2M^2}} = \frac{1}{2+\frac{4}{k^2Q_{tx}Q_{rx}}} \tag{6.12}$$

From (6.12), it can be seen that maximum efficiency is achieved by maximising the product $k^2Q_{tx}Q_{rx}$, which is a function of frequency. Clearly the operational frequency will have a large influence on system performance. However, due to the aforementioned fundamental limitations, $k^2Q_{tx}Q_{rx}$ will always be small and hence, a through metal IPT system will never achieve high efficiencies. Despite this, IPT can still be a useful tool for through metal applications. The power requirement of the 'inside' electronics should be relatively low such that IPT can still be practical even if losses are high.

6.1.2 Experimental Results

Analysis using an analytical model provides a basic understanding of an IPT system. However, the analysis does not provide much insight into the achievable efficiency or optimal operating frequency for a real world problem. This is because the interaction between the coil's magnetic field and the wall is complex and hence, k and Q cannot be obtained from a simple analytical expression. The aim of this section is to analyse an IPT system through practical experimentation.

As stated previously, a key potential application requiring through metal power delivery is the monitoring of hazardous materials, which are often stored in stainless steel flasks [112, 113]. In light of this, a 20mm-thick, 130mm⌀ stainless steel disc was selected as an appropriate material sample for experimentation purposes.

6.1.2.1 Efficiency Estimation From Measured Parameters

An experiment was performed with two 150-turn loop coils (115mm⌀) either side of the aforementioned stainless steel disc. From this arrangement, it is possible to obtain the parameters k, Q_{tx} and Q_{rx} and, hence, power transfer efficiency through a 20mm thick stainless steel wall can be estimated from (6.12).

To calculate k, the mutual inductance of the coils must be known. The mutual inductance, M, for a given system, is the constant of proportionality relating the induced open circuit voltage across the pickup coil, V_{open}, to the rate of change of current in the driving coil. For a sinusoidal driving current, the mutual inductance may be obtained from (6.13), where I is the current amplitude and f is the frequency. RMS amplitudes are used for all measurements where applicable.

$$M = \frac{V_{\text{open}}}{2\pi f I} \tag{6.13}$$

To obtain M experimentally, the transmit coil was driven at a fixed frequency from an Agilent 33220A arbitrary waveform generator while the current was measured with a Fluke 179 true RMS multimeter. The open circuit voltage was measured across the terminals of the receive coil using a Tektronix TDS2024B oscilloscope.

The coil self inductances, L_1 and L_2 were obtained using an Agilent E4980A precision LCR meter. The coupling coefficient, k, may then be obtained from (6.14).

$$k = \frac{M}{\sqrt{L_1 L_2}} \tag{6.14}$$

The coil Q factors, Q_{tx} and Q_{rx}, can be measured directly from the precision LCR meter. By repeating these measurements across a range of frequencies, the 'system efficiency frequency response' can be approximated. The resultant curve is shown in Fig. 6.3 with the corresponding legend entry, 'Analytical approximation from measured coil properties'.

6.1.2.2 Direct Experimental Efficiency Measurement

The power transfer efficiency of an IPT system can also be directly evaluated by measuring the input power and the power delivered to the load resistance, R_L, using the setup shown in Fig. 6.4. The input current, I_{in}, is measured using a true RMS multimeter and the input voltage, V_{in}, is measured using an oscilloscope and converted to a RMS value. The input power may be evaluated from (6.15) because the system operates at resonance and hence, the phase shift between voltage and current is zero. As the load resistance is known, then the output power, P_{out}, may be evaluated by measuring the voltage across R_L using (6.16).

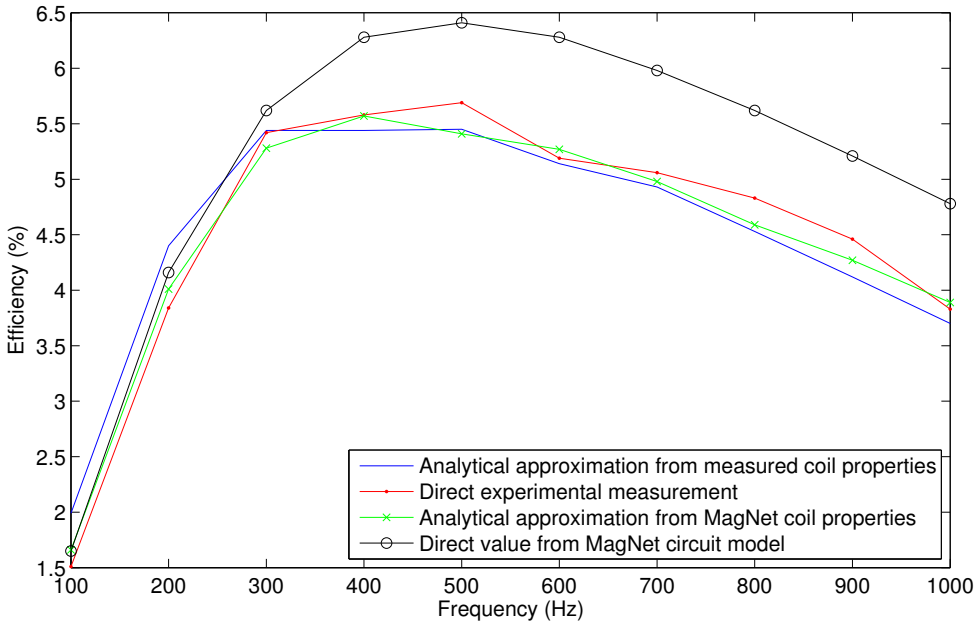

Figure 6.3: Comparison of predicted system efficiency, obtained from coil parameters, and measured efficiency from both experiment and simulation.

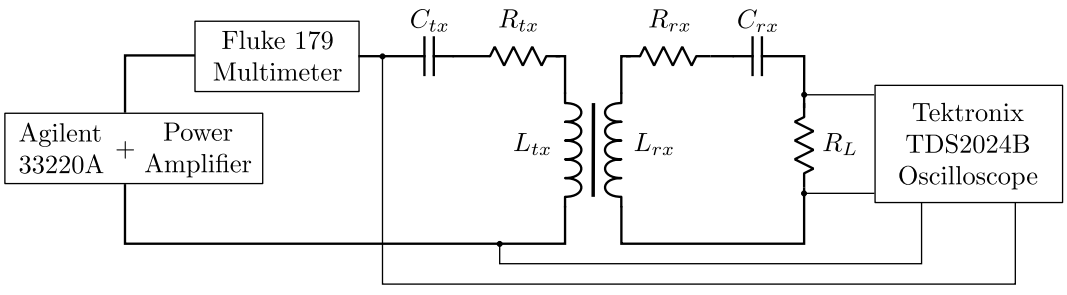

Figure 6.4: Experimental setup for measuring the efficiency of an IPT system directly.

$$P_{\text{in}} = V_{\text{in}} I_{\text{in}} \tag{6.15}$$

$$P_{\text{out}} = \frac{(V_{\text{out}})^2}{R_L} \tag{6.16}$$

As previously, a measurement may be taken at a range of frequencies to determine the optimal operating frequency. At each frequency, it is essential that the coils are retuned to resonance and that the load resistance is matched to the receive coil resistance. This ensures that the result is a true frequency response and not distorted due to using a non-optimal load. The curve produced from this set of measurements is shown in Fig. 6.3 with the corresponding legend entry, 'Direct experimental measurement'.

The response exhibits small amplitude fluctuations, which are not present in the analytical approximation, and may be explained from two non-idealities in the experiment. Firstly, the large shift in inductance across the frequency range means the capacitor type used for tuning cannot be kept constant. Consequently, the equivalent series resistance of the tuning capacitor is not constant and this introduces a small variable loss to the circuit. Secondly, it is assumed that both sides operate at resonance, whereas in practice, the system operates with a power factor ≥ 0.99. The small phase shift should have minimal influence on the obtained performance figures.

The frequency response curves obtained analytically and from direct measurement are in good agreement, as shown in Fig. 6.3, validating the analytical model.

Experimental results indicate that an efficiency exceeding 5% is achievable with an operating frequency of 500Hz, however, the calculated efficiency is not a perfectly accurate representation of a sealed container due to the finite boundaries of the plate sample.

6.1.3 Finite Element Modelling

Ideally, a large metallic container would be available for direct experimentation. However, this is simply not practical and a far more attractive alternative is finite element (FE) computer modelling. Infolytica's MagNet simulation software package is ideal for solving 2D or 3D low frequency electromagnetic problems and as such, is a very popular choice for electrical machine and transformer design [114–117].

Table 6.1: FE simulation parameters.

Wall		Coil	
Material	Stainless steel	Material	Copper
Thickness	20mm	Conductivity	5.86×10^7 Sm^{-1}
Conductivity, σ	1.3×10^6 Sm^{-1}	Outer Diameter	115mm
Permeability, μ_r	1.1	Inner diameter	80mm
Diameter	130mm	Liftoff	0.1mm
Airbox		**Mesh**	
Material	Air	Wall slice	1mm
Diameter	600mm	Max coil element	3mm
Depth	400mm	Max airbox element	10mm
Boundary	Flux tangential		

6.1.3.1 Experimental Comparison

A logical first step in the modelling process is to compare the simulation output to the experimental results obtained previously. Hence, an FE model was produced which was as close as possible match to the experimental setup, as shown in Fig. 6.5a. Due to symmetry, only a quarter section of the problem need be modelled, which significantly reduces memory requirements. The geometry can be easily replicated but the material properties, i.e. the conductivity and permeability of the stainless steel sample, are only estimates. The simulation parameters are shown in Table 6.1.

The modelled coils may be included as elements in a SPICE circuit and upon completion of the simulation, the software returns all of the circuit currents and voltages. Hence, it is possible to replicate both the analytical approximation and direct evaluation experiments.

FE Analytical Approximation

It is advantageous to compute the analytical approximation because it gives a better insight into the mechanisms which are affecting system efficiency, namely the effect of frequency on the coupling coefficient and coil Q factors. By comparing these properties it can then be seen if the FE model is truly representative of the experimental setup.

The process for obtaining these parameters is similar to that of the experimental setup. Mutual inductance is obtained by performing a simulation run with the

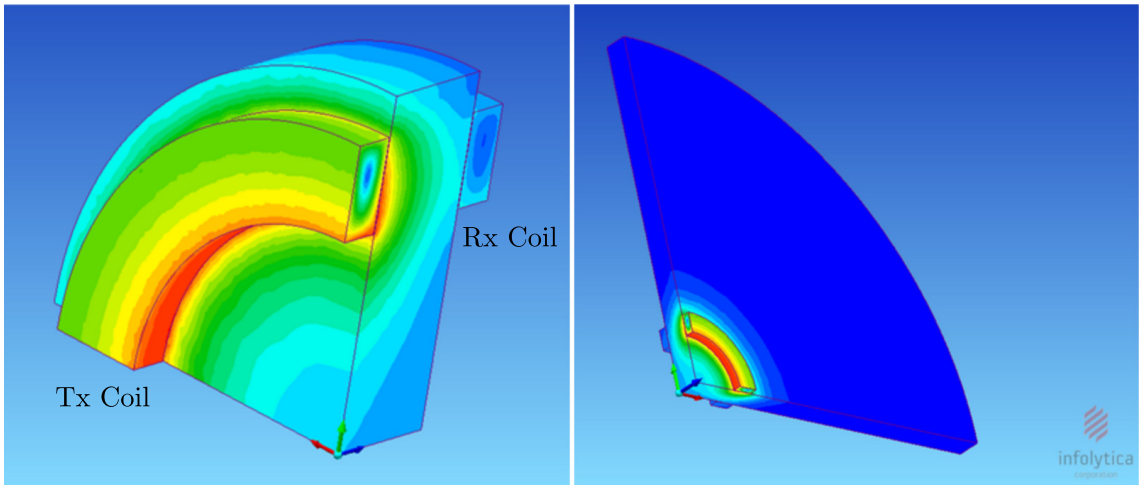

Figure 6.5: MagNet simulation models. (a) A small 20mm thick stainless steel plate. (b) A 20mm thick infinite stainless steel wall. The airbox and model boundaries are hidden for clarity. Colour indicates the RMS of the magnetic flux density at 400Hz.

receive coil open circuit and evaluating (6.13). The simulation calculates the flux linkage, $N\Phi$, and hence, the coil inductance may be calculated from (6.17). The coupling coefficient may then be calculated using (6.14).

$$L = \frac{N\Phi}{I} \tag{6.17}$$

The coil Q factors are not output directly and hence, must be calculated from (6.18).

$$Q = \frac{\omega L}{R} \tag{6.18}$$

The measured coupling coefficient and simulation result are compared in Fig. 6.6 for a range of frequencies. Likewise, the coil Q factors are compared in Fig. 6.7 and both the trend and absolute values show good agreement. The efficiency curve calculated using these values is shown in Fig. 6.3 with the corresponding legend entry 'Analytical approximation from MagNet coil properties'.

FE Direct Evaluation

The direct efficiency experiment can be simulated by including the coils as elements in the circuit shown in Fig. 6.2a. A preliminary simulation run is required at each test frequency to determine the coil inductance and resistance so that the appropriate series capacitance and load resistance can be included in the circuit. The coil resistance and inductance may be obtained from the real and imaginary parts of

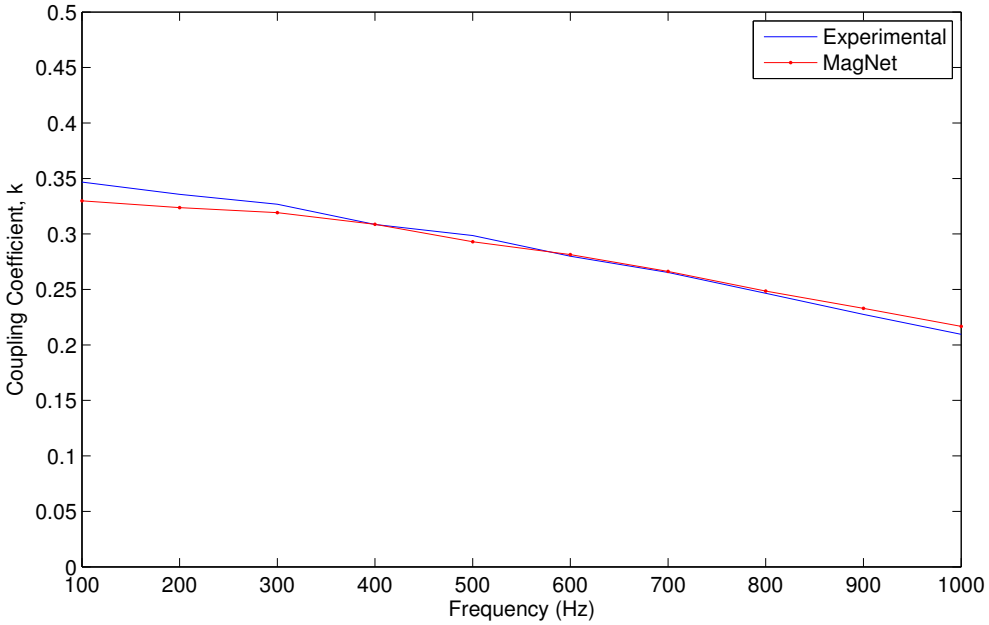

Figure 6.6: Comparison of the coupling coefficient, k, obtained from experimental measurement and from MagNet simulation.

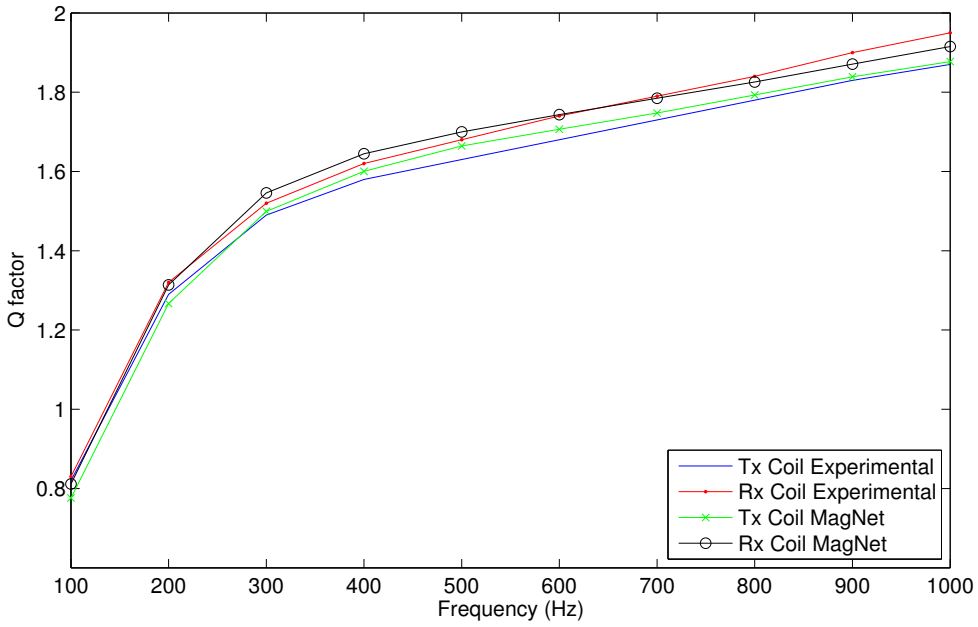

Figure 6.7: Comparison of the coil Q factors obtained from experimental measurement and from MagNet simulation.

the coil impedance respectively. The obtained result is shown in Fig. 6.3 with the corresponding legend entry, 'Direct value from MagNet circuit model'.

6.1.3.2 Experimental Comparison Discussion

The four traces shown in Fig. 6.3 all show good agreement, indicating that the model is an accurate representation of the problem. The direct value from the MagNet circuit model predicts slightly higher efficiencies but the trend remains consistent.

Comparison of the system coupling coefficient and coil Q factors with the experimental measurements shows that the simulation is accurately modelling the interaction between the coils and the metal wall, as shown in Fig. 6.6 and Fig. 6.7. These plots also demonstrate the origin of the optimum operating frequency for a through metal IPT system.

The coupling coefficient decreases with increasing frequency and is very approximately linear across the frequency range of interest. In contrast, across the same frequency range, the coil Q factors increase in a non-linear fashion. The increase is rapid at lower frequencies before levelling off at higher frequencies. Hence, at lower frequencies, the increase in $Q_{tx}Q_{rx}$ is greater than the reduction in k^2 and efficiency increases. At higher frequencies, the opposite is true and consequently, the response experiences a maximum at the turning point.

The coupling coefficient decreases with frequency due to the reduction in skin depth of the wall, while the proximity effect is the major factor limiting the Q factor of the coils. As the frequency increases, the magnetic field of adjacent conductors, i.e. the individual turns of the coil, constrain the current distribution to a smaller cross sectional area, increasing resistance. Eddy currents induced in the wall also contribute to this effect and further increase the coil resistance. Consequently, the optimal operating frequency for an IPT system will always be relatively low.

6.1.3.3 FE Simulated Infinite Wall

Satisfied with the accuracy of the model, the metal plate was increased in size to 600mm diameter to simulate a sealed enclosure, as shown in Fig. 6.5b. The RMS magnitude of the magnetic flux density, indicated by the colour in Fig. 6.5b, shows that all interaction between the coils is due to flux penetrating the wall and hence, the wall is deemed to be sufficiently large.

This model was used to predict the power transfer efficiency through a 20mm thick stainless steel walled enclosure, for a range of frequencies and permeabilities, to produce the performance surface shown in Fig. 6.8.

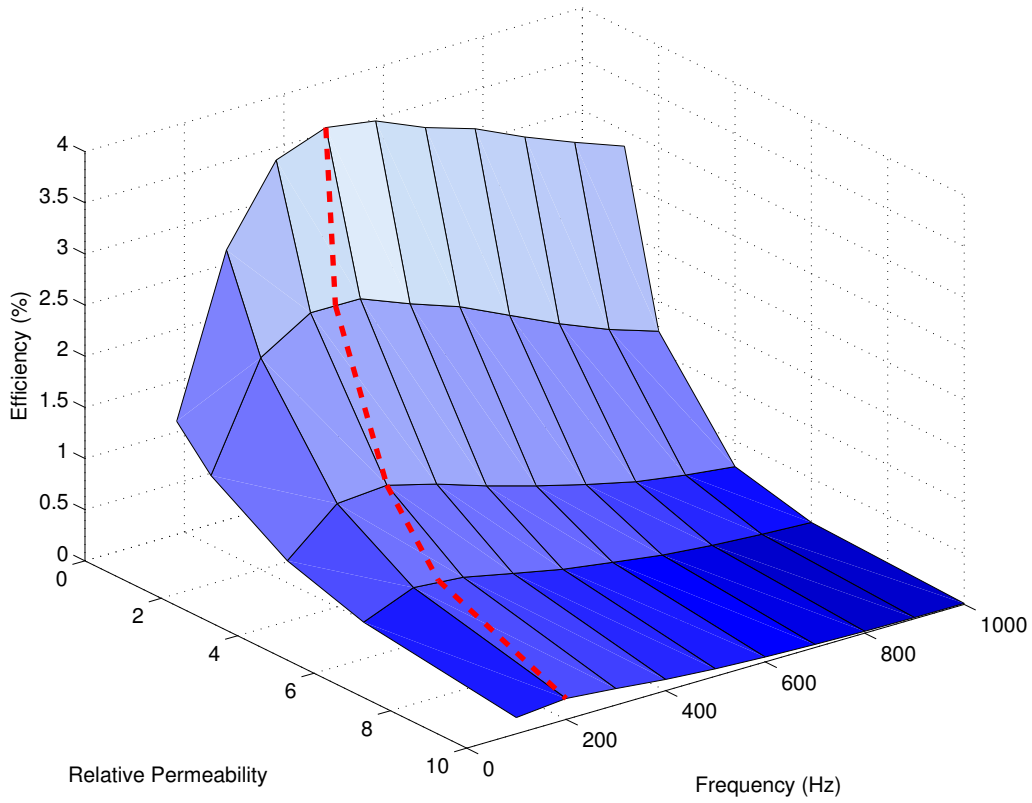

Figure 6.8: Simulated system efficiency variation with permeability and frequency. The shifting optimal operating frequency is indicated by the dashed line.

This surface demonstrates a maximum efficiency of 3.9% at 400Hz for austenitic stainless steel with $\mu_r = 1.1$ and $\sigma = 1.3 \times 10^6\ \mathrm{Sm}^{-1}$. The efficiency degrades as a function of permeability; when $\mu_r = 10$, the maximum achievable efficiency is 0.2% at 200Hz. It is notable that the optimal operating frequency decreases as the losses increase.

The coupling coefficient is shown in Fig. 6.9 as a function of permeability and frequency and clearly demonstrates the reliance of system performance on the material properties. Comparing the coupling coefficient obtained from the original experimentation and that of the simulated complete enclosure shows that experimentation using small plate sample gives a reasonable approximation of the obtainable efficiency.

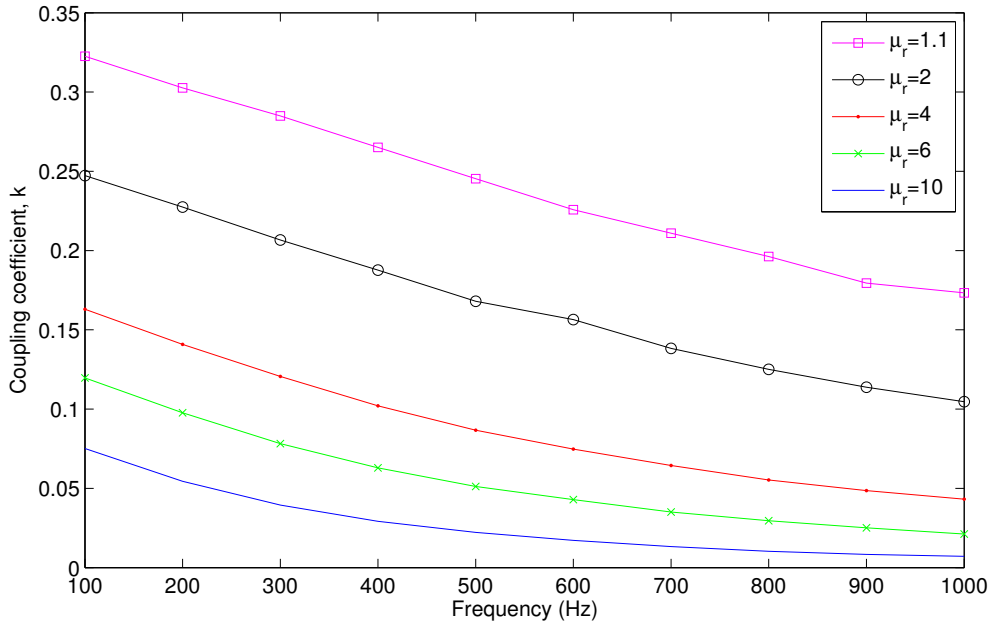

Figure 6.9: Variation of k with permeability and frequency from MagNet simulation of a stainless steel enclosure.

6.1.4 Inductive Data Communications

While analysed previously as a pure power transfer system, inductive, low bit rate communications are also feasible for sensor applications. When data requirements are sufficiently low, a high bandwidth acoustic link becomes surplus to requirements as sufficient data can be modulated onto the magnetic field.

Two modes are possible: 1, Sequential operation, whereby power is supplied for a finite duration, to charge some internal circuitry, which then replies with a burst of data; 2, Load modulation, whereby power is supplied continually and an internal load is switched between high and low impedance to convey data.

A sequential system can deliver a considerably higher data rate but also requires more sophisticated internal electronics for power regulation, storage and data transmission. From Fig. 6.8 it can be seen that a system set up for optimal power transfer at 400Hz on 20mm thick stainless steel plate ($\mu_r = 1.1$ and $\sigma = 1.3 \times 10^6\,\mathrm{Sm}^{-1}$) has a system bandwidth approximately 250Hz. The achievable data rate will ultimately depend on the SNR, which is a function of the input power, but due to the inherent bandwidth limitation this will never exceed a few kbps.

Reflected load modulation provides a simpler solution and allows for a continuous low bit rate data stream. The impedance of the receive coil can be reflected to the transmit side as shown previously in Section 6.1.1 to give the equivalent circuit

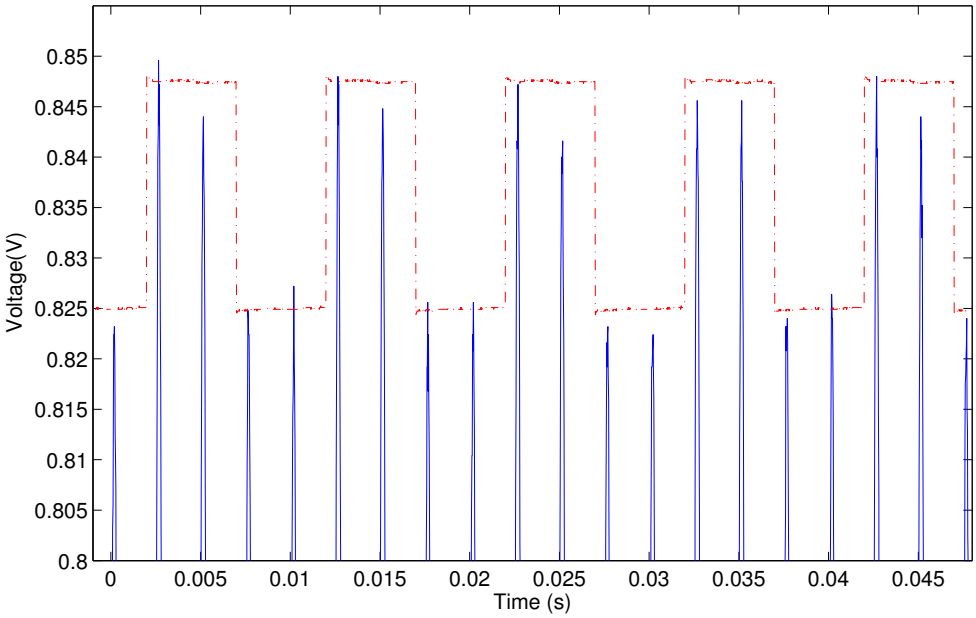

Figure 6.10: Transmit coil voltage envelope resulting from an internal load switched at 100Hz.

shown in Fig. 6.2c. Therefore, if the impedance of the receive circuit is changed, this causes a detectable change in the voltage dropped across the transmit coil. Initial experimentation indicates data rates in excess of 100bps are achievable with this technique. Fig. 6.10 shows the amplitude modulation seen at the external transmit coil as a result of load modulation at the internal receive coil. This result was obtained using the 20mm test plate and a signal generator switching the load impedance between open and short circuit at 100Hz by means of a simple transistor circuit.

6.1.5 IPT Discussion

The analysis, experimentation and simulation in the previous sections have shown that $\approx 4\%$ power transfer efficiency is achievable through a 20mm stainless steel enclosure with relative permeability, $\mu_r = 1.1$, and conductivity, $\sigma = 1.3 \times 10^6\,\mathrm{Sm}^{-1}$. Although the efficiency is relatively low, the power requirement is sufficiently modest such that $\approx$ 7W of power would be required to extract data from the enclosure at a rate of 1Mbps using the EMAT based system described in Section 5.7.5, which is certainly feasible. Furthermore, this would assume a continuous data stream and in many monitoring applications periodic readings will suffice, which would significantly lower the mean power delivery requirement.

It was shown that when the relative permeability is increased, such that $\mu_r = 10$, the peak achievable efficiency is 0.2%, which starts to make IPT impractical. However, it is not possible to make generalisations regarding a particular material, as to what is and is not practical, based purely on the electrical and magnetic properties, as the thickness is also a key parameter. If the wall were significantly thinner, such that a higher permeability wall represented an equivalent number of skin depths as the simulated plate, then a broadly similar efficiency should be achievable. The efficiency will only be broadly similar because the separation distance of the coils will also directly affect efficiency [118].

It should be noted that materials such as highly permeable steels, e.g. HY80, would not be suitable for IPT at any practical thickness, due to the extremely small skin depth.

The work in this chapter has focussed on a specific case, due to the limited availability of test samples for experimental comparison, but the simulation techniques presented should be suitable for modelling any through metal scenario, provided the properties can be estimated.

Tests and simulation have all been performed using low power levels and efficiencies quoted as a fixed value. However, at greater power levels or lower efficiencies, the system will generate a significant amount of heating in the wall and in the coils. Consequently, the electrical properties of the system will change depending on the power being delivered and this will subsequently affect system efficiency. Heating effects will most likely determine the upper limit on power delivery for the system. If high power levels are required then this is certainly an area for further research.

This study has attempted no optimisation of the coils themselves and it may be possible to improve performance with a refined coil design. Firstly, Litz wire may help increase the Q factors of the coils by minimising proximity effect losses. Secondly, the ratio of the coil separation and coil diameter should be selected such that the diameter is much greater than the separation distance [118]. The size of the coils used for the system in this chapter were limited by the stainless steel plate but the ratio was still favourable. Finally, the coil should be designed with an impedance, such that the required tuning capacitor type has minimal ESR which will help minimise losses.

Overall, these sections have shown that IPT could potentially have niche applications for through metal power transfer where a non-contact system is required and power requirements are modest. Furthermore, the system has the potential to support low bit rate inductive data communications.

6.2 Piezoelectric Power Delivery Comparison

The previous sections of this chapter have shown IPT to be a viable mechanism for through metal power transfer. This section provides a comparison with piezoelectric transducers, which are the only other reported method in literature. The schemes are highly contrasting and the main advantages and disadvantages are discussed in the following subsections.

6.2.1 Wall Material and Thickness

The key benefit of acoustic power transfer with piezoelectric transducers is that the system is not sensitive to the skin depth of the material, making piezoelectrics suitable for use with a much wider range of materials. The applicability of IPT, i.e. where efficiencies of at least a few percent can be achieved, is likely to be limited to low conductivity, low permeability metals such as stainless steel, titanium and lead for any wall thickness greater than a few millimetres. For thicknesses below a few millimetres more conductive materials, such as aluminium should be feasible. Materials such as steel, which have an even smaller skin depth due to the orders of magnitude increase in μ_r, are likely to be only suitable for acoustic methods. This is unfortunate as, due to its corrosive nature, steel is very likely to be coated, which impedes piezoelectric coupling and would have been an ideal candidate for a non-contact system.

It is difficult to provide a direct efficiency comparison between the the two mechanisms as the material and wall thickness used in published work tends to vary from author to author depending on the intended application. However, under ideal conditions a piezoelectric system should give superior performance.

6.2.2 Transducer Dimensions

The IPT system used for analysis uses loop coils which are 115mm in diameter, which is considerably larger than the average diameter of a piezoelectric transducer, which are typically around 25.4mm diameter for through metal applications. If the wall footprint of the system is restricted then IPT is likely to be unsuitable. It is shown by Chen *et al.* [118] that to improve the efficiency of a loosely coupled IPT system, the coil diameter should be much larger than coil separation.

6.2.3 Channel Variation and High Temperature Operation

Power delivery with piezoelectric transducers is an acoustic technique and hence, suffers from multipath propagation and fading. A constant, continuous wave is

transmitted to the 'inner' transducer, which will reverberate, resulting in a standing wave within the channel. The power delivered to the receiver is dependent on the superposition of the primary arrival and multipath, which may be constructive or destructive. Selection of the operating frequency is therefore paramount to the performance of the system as this will determine the constructive or destructive nature of the multipath.

As demonstrated by Shoudy *et al.* [35], a small variation in the operating frequency can have a dramatic effect on system efficiency. In their experiment on a 57mm test block, it is shown that a system based around 1MHz transducers exhibits a maximum at 1.087MHz and a 10 fold efficiency reduction at 1.021MHz. For a static channel this problem is moot as the optimal frequency can be selected upon installation. However, it is possible to have some degree of time variability in a metal wall channel as discussed in Section 4.1.3.2. If the channel response is altered by environmental conditions, such that the system operates in a deep fade or null, then efficiency will suffer.

An IPT system should be largely insensitive to variations in the channel and should give consistent performance, hence, it is the preferred technique for any scenario with channel variability.

Rather than channel fluctuations, oil and gas, nuclear and chemical process applications may all involve consistently high operating temperatures. The operational temperature of a piezoelectric transducer is limited by the Curie temperature, which is the point at which the material loses its piezoelectric properties. The Curie temperature varies for different piezoelectric materials with a typical range being $210°C - 365°C$ [119]. To ensure long term reliability, it is recommended to operate a piezoelectric transducer significantly below the limit of the Curie temperature.

In contrast, an IPT system does not have a fixed upper bound on operating temperature. Increased temperature will, however, affect the conductivity of the coils and this will reduce efficiency.

6.2.4 Coupling

The performance of any technique requiring direct contact will always have a strong reliance on the quality of the bond between transducer and metal. Eliminating this coupling dependence has been a key theme throughout this work and was the initial motivation for the development of non-contact alternative transducers; the unreliability of acoustic coupling was best shown by Sherrit *et al.* [32], as discussed in Section 2.4.1.1.

The experimentation and simulation performed in this work used an IPT setup with minimal coil liftoff. However, a larger distance should be possible, which would account for any surface coating, but this will obviously have a negative impact on efficiency.

Although not within the confines of the original problem definition, it is worth mentioning that IPT is uniquely applicable to problems involving a sandwich of materials, including air gaps, i.e. situations where it is impossible for an acoustic wave to propagate from 'outside' to 'inside'. Again, further investigation would be required to ascertain the achievable performance for such a scenario.

6.3 Summary

This chapter has analysed inductive power transfer for through metal applications using analytical modelling, experimentation and finite element simulation. It has been shown that IPT has potential applications when the properties of the wall are favourable i.e. the skin depth is large or the wall is thin. The wall and coil properties determine the optimal operating frequency of the system which corresponds to the maximum of the product $k^2 Q_{tx} Q_{rx}$, where k is the coupling coefficient and Q_{tx} and Q_{rx} are the coil Q factors. Where applicable, IPT offers several advantages over previous piezoelectric systems, including non-contact and potentially high temperature operation.

Chapter 7

Conclusion

This chapter draws together the key results and conclusions of the previous chapters and is split into two main sections, the first covering through metal communications and the second covering through metal power delivery. Both of these sections provide an in-depth discussion of the key findings of this work and also provide suggestions for improvement and further development.

7.1 Through Metal Communications

Upon commencement of this work in 2007, through metal communications had received very little academic interest. At this time, industrial and military applications were demanding increasingly invasive sensor systems, which became problematic when a metal structure prevented standard radio communications. Consequently, interest grew and it has since become apparent that several other research groups had been investigating the problem almost in parallel with this study. The consensus across the studies is that acoustic techniques, or more specifically ultrasonics, represent the most attractive mechanism for through metal communications due to the favourable SNR and high bandwidth. The unanimous approach of other research groups is to use coaxially aligned piezoelectric transducers to transmit and receive acoustic telemetry. The main challenges associated with an acoustic system for a metal wall channel are multipath induced fading and ISI. It is mainly the techniques used to overcome these transmission impairments which have been the focus of competing works.

7.1.1 Transduction

It may be argued that the most important component of an acoustic through metal communications system is the transducer because reliable ultrasonic transduction is

essential to the operation of the system. All other published works use piezoelectric contact transducers as the basis of their system, which have excellent efficiency under ideal laboratory conditions. However, their performance is heavily reliant on coupling, i.e. the quality of the bond between the transducer and the metal surface, which, for real world applications, leads to costly and time consuming installation, unpredictable performance and concerns over long term reliability. In fact, this bond represents an unacceptable point of failure for industrial and military applications, especially for situations where the metalwork may experience high levels of stress. Hence, the logical starting point of this work was to investigate various ultrasonic transduction mechanisms with the aim of removing any reliance on coupling.

The non-contact, electromagnetic acoustic transducer (EMAT) was proposed as a novel alternative approach. A prototype system was produced based on the radially polarised shear wave EMAT configuration, which generates acoustic waves in non-ferrous and ferrous materials using principally the Lorentz force and magnetostriction mechanisms respectively. This system represents the first EMAT based communications system reported in literature.

An EMAT approach offers several significant practical advantages over an equivalent piezoelectric system. The following points describe the unique advantages with respect to the previous state-of-the-art.

i. *No requirement for good acoustic coupling* – Sound is induced directly into the metal and consequently, results are highly repeatable. A critical failure point is removed which should greatly improve long term reliability.

ii. *Operation is possible with* $> 10mm$ *transducer-wall separation (liftoff)* – Any material with very low conductivity and permeability, such as air, water, paint, plastics, enamel, wood etc, may be placed between the transducer and the metal with a predictable effect on performance. This allows for operation on metals with thick surface coatings which would inhibit piezoelectric coupling.

iii. *Fixing mechanism* – The powerful permanent magnet provides a fixing mechanism to ferrous walls and a fixing/self-aligning mechanism for thin non-ferrous walls.

iv. *Rapid deployment* – There is no requirement for prior surface preparation or couplants/adhesives with lengthy cure times and hence, a system can be installed in minutes.

v. *Temporary fit* – Installations are possible with no permanent alteration to the wall or its coatings.

vi. *Higher operating temperatures* – EMATs can operate at temperatures which far exceed that of piezoelectric transducers and/or appropriate coupling materials.

vii. *Highly localised vibration* - Shear waves cannot propagate in non-viscous fluids such as air and water and hence, the acoustic wave is confined to a localised area of the metal, preventing external detection. This is especially important for military applications.

The primary disadvantage of EMATs is the low transduction efficiency relative to a well coupled piezoelectric transducer, however, the efficiency is not prohibitively low and through metal communications have been successfully demonstrated. The other disadvantage is that EMATs exacerbate the channel as discussed in the next section.

Despite these drawbacks, EMATs represent a significant advancement toward robust through metal communications for many industrial applications.

7.1.2 Pulse Position Modulation

The acoustic modulation schemes presented in this thesis are designed to be independent of the transduction mechanism; although EMATs have attractive properties for a versatile system, there will still be applications where piezoelectrics can be utilised, hence, it should be noted that all proposed communications techniques are applicable to both transducer types.

The impulse response for the two transducer types are contrasting due to their contact and non-contact natures. Under ideal coupling conditions a piezoelectric receiver converts a significant portion of acoustic energy to electrical energy, reducing the amplitude of successive reverberations. The non-contact EMAT receiver has a negligible effect on the propagating wave and hence, if no scattering occurs due to the metal surface texture, the multipath will decay purely as a function of distance. Consequently, the multipath is more severe for an EMAT based system.

It is possible to determine the worst case multipath duration for a given material if the speed of propagation and attenuation are known. Hence, burst mode transmission is guaranteed to overcome ISI with the selection of an appropriate guard interval. A pulse position modulation scheme is presented, which is shown to be capable of data rates up to 50kbps for a worst case steel wall channel.

Pulse position modulation is very attractive for moderate data rate systems due to a number of factors:

i. *Simple to implement* – The scheme requires only timers to modulate and demodulate data packets, consequently, PCBs can be miniaturised and component costs can be kept to a minimum.

ii. *Power efficient* – At lower data rates the scheme is far more power efficient than continuous wave modulation due to the low transmit duty cycle.

iii. *Low power receiver* – No complex signal processing or other computation is required at the receiver, minimising power requirements.

The project sponsors placed a strong emphasis on hardware demonstration and hence, EMATs and pulse position modulation were combined in the design of the rapidly deployable acoustic gateway demonstrator system. The low cost, low power hardware and moderate data throughput makes the units ideal for routing the data of large, low data rate sensor networks on board naval vessels. Previous approaches to through metal communications either provide insufficient throughput or are prohibitively complex/expensive for such an application. Field testing on board such a vessel demonstrated reliable ultrasonic generation on a variety of surfaces and transmission through up to 72mm of steel. These practical results represent the first reported data transmissions through a surface coated metal channel. Communications performance only became unsatisfactory when the composition of the material inhibited ultrasonic propagation and distorted the channel impulse response. For this sort of channel, a more complex modulation scheme is required.

7.1.3 High Bit Rate Communication and Equalisation

The data rates achievable with burst mode transmission are ultimately limited by the presence of a guard interval. Higher data rates are possible using a continuous wave carrier, however, channel equalisation is required to mitigate the effects of ISI, which increases the system complexity. It is important to appreciate that many through metal communications applications will be asymmetric, whereby data is transmitted from inside a sealed enclosure to the outside. Consequently, it is advantageous to minimise the complexity, size and power requirements of the remote 'transmit' side and place any additional complexity at the receiver.

There have been some attempts to mitigate ISI by exploiting the channel geometry and also by using piezoelectric transducers with high quality coupling, but this sort of arrangement is difficult to achieve in real world applications. Primerano *et al.* proposed using pulse amplitude modulation (PAM) and a pre-distortion filter to pre-equalise the channel by transmitting an echo-cancelling pulse with each symbol. In this thesis, a combination of QPSK modulation and the decision feedback equaliser (DFE) is shown to offer several advantages over the pre-distortion filter approach:

i. *Power efficiency* – Transmitting a cancelling pulse is inherently less power efficient than signal processing at the receiver.

ii. *Training and tracking* – Pre-equalisation requires training information generated at the receiver to be conveyed back to the transmitter in order to initially train or update the parameters for echo cancellation. This means a secondary low data rate mode is required to convey information ISI free. A DFE can be periodically retrained without this added complexity.

iii. *Transmitter complexity* – A pre-distortion filter significantly increases the complexity of the transmitter, which is undesirable for asymmetric applications. Conversely, a QPSK modulator can be constructed using an H-bridge and a simple digital I/O device. For hostile environments, a resilient electronics solution may be required and hence, a simple transmitter design is essential.

iv. *Independent of the channel response* – The pre-distortion filter makes several assumptions regarding the channel response and consequently, performance will be poor if the response is irregular. The DFE can be trained to equalise any multipath channel with no *a priori* knowledge of the channel.

Experimentation with this high bit rate setup demonstrates it is possible to achieve data rates in excess of 1Mbps with very low bit error rates (BER), which compares favourably to the theoretical channel capacity.

The linear equaliser (LE) is an alternative structure which can achieve very good performance for a metal wall channel exhibiting the standard impulse response, i.e. multipath periodicity and exponential multipath decay. However, the DFE is still preferred as a general solution.

Previous works often comment that the efficiency of an EMAT is considerably lower than a piezoelectric transducer but no attempt has been made to quantify the relative efficiencies. This thesis presents the first empirical data comparing an equivalent piezoelectric and EMAT based through metal data communication system. Under perfect coupling conditions it is demonstrated that EMATs require 130× the input power to achieve the same communications performance. Introducing a liftoff of 0.8mm to the transmitting and receiving EMATs required a further 5× increase in input power. The absolute power input of 1.23W for 1Mbps through 25.4mm of steel with 0.8mm transducer liftoff still represents an acceptable level for a practical system given its unique non-contact capability.

7.1.4 Future Work

The work presented in this thesis offers some significant advancements over previous/competing systems for through metal communications but there are still a number of interesting areas for further research. Some of the author's ideas are briefly outlined in this section.

The requirement for two EMAT pairs for bi-directional communications doubles the size of the wall footprint. It is worth investigating if the coils can be combined by electronically switching turns in or out for transmit and receive operations. This would help minimise the device dimensions for space constrained applications.

Some niche applications may allow good coupling on one side but not the other and for such a situation, an EMAT/piezoelectric hybrid system could offer advantages. Due to the different wave modes, the two transducers are not currently compatible and hence, alternative configurations need exploring.

The next stage of development for the continuous wave transmission system is to produce a real-time system and package it in a similar manner to the acoustic gateway demonstrator system. Efficient power management would be a key area of interest due to both the increased power requirement of the receiver and the contrasting power budget of the inside and outside electronics for an asymmetric application. Designing a ruggedised version for hostile environments is also of interest.

The simplistic EMAT transmitter power amplifier posed limitations on the available modulation schemes. Although not trivial, the design of a minimal complexity linear power amplifier would allow modulation schemes such as QAM or OFDM to be implemented and compared to phase modulation schemes.

Although not directly related to through metal communications, a wireless protocol designed specifically to integrate with acoustic gateways could be an interesting area of study. The novel aspects would mainly involve coping with the gateway latency and attempting to normalise power consumption of the gateways with intelligent packet routing.

7.2 Through Metal Power Delivery

The history of through metal power delivery is similar to that of communications, whereby there were very few published works prior to the start of this study. Once again, the transduction mechanism received little attention as all works used piezoelectric transducers. Although piezoelectrics are well understood, the drawbacks that make piezoelectrics unsuitable for many practical communications problems

are just as applicable to power delivery and hence, a non-contact solution is highly desirable. Unfortunately, the low efficiency of an EMAT makes it unsuitable for this purpose.

In this thesis, a novel inductive power transfer system is shown to be a viable solution for through metal power delivery, which offers several advantages over piezoelectric based systems:

i. *No need for good acoustic coupling* – Inductive techniques are non-contact and hence, can operate without direct contact to the metal wall surface.

ii. *No multipath propagation* – Acoustic systems suffer from power transfer null frequencies due to multipath induced fading. If there is any time variability in the channel then the system must track the optimal operating frequency. Inductive systems do not suffer from multipath propagation and hence, have no need for this added complexity.

iii. *Low frequency* – Inductive systems operate at low frequencies and therefore, can be operated simultaneously with high frequency acoustic communications without interference.

iv. *High temperature operation* – A loop coil can operate at temperatures far exceeding the curie point of a piezoelectric crystal.

The key disadvantage of an inductive approach is that the technique is highly sensitive to the electrical and magnetic properties of the metal wall. The key aims of this study were to analyse the key parameters of a through metal inductive power system and to determine the achievable power transfer efficiency for a practical metal wall channel. This sort of analysis has not previously been reported in literature.

Analytical modelling shows a series-series tuned through metal IPT system can be described using an equivalent circuit model. A good approximation of the optimal load resistance is to match it to the resistance of the receive coil and the system efficiency may then be determined from the product of the coupling coefficient and coil Q factors. The metal wall channel will reduce the coupling coefficient and the proximity effect will reduce the coil Q factors and consequently, the efficiency will always be relatively low.

Practical experimentation was used to obtain performance figures for a 20mm-thick stainless steel wall using two 115mm diameter loop coils. The coil Q factors and the material skin depth are a function of frequency and therefore, so is system efficiency. The coil Q factors increase as a function of frequency whereas the coupling coefficient always decreases with frequency due to skin effect, hence, the product experiences a maximum, which determines the optimal operating point.

The small dimensions of the test piece available for experimentation meant the setup was not truly representative of a sealed metal enclosure. Consequently, finite element modelling was employed for further analysis. Simulation of a sealed enclosure demonstrates that approximately 4% transfer efficiency is achievable through 20mm-thick low permeability stainless steel. Increasing the permeability is shown to lower both the maximum achievable efficiency and the optimal operating frequency. With a relative permeability of 10, the efficiency of the system reduces to 0.2%, highlighting the limited range of materials for which the technique will be suitable. Nevertheless, this study has shown that IPT offers an alternative to piezoelectric transducers for low permeability materials such as stainless steel, lead, titanium and aluminium, which are commonplace in the nuclear and oil and gas industries. Beyond this, the key contributions of this section of work are the demonstration of the frequency dependence of a through metal IPT system and the production of an accurate finite element model which can be used to predict system performance for any scenario.

7.2.1 Future work

The work presented on IPT differs from that on acoustic communications in the sense that it analyses the feasibility of the approach, whereas sound propagation through metal was already well understood. Consequently, far more development is required to produce an IPT system suitable for practical applications. This short section presents the author's thoughts for further development.

An obvious area for further investigation is the coil design, which will directly influence efficiency. A particular area of interest is to determine the smallest coil dimensions which can be used without a dramatic reduction in the quoted efficiency figures. This is an important step toward miniaturising the design.

Once the coil designs are established, the next logical step would be to develop the power regulation, conditioning and storage circuitry and produce a demonstrable prototype. This could then be integrated with EMAT based acoustic communications to produce a non-contact power delivery and communications system for niche applications.

Further modelling of the problem would be useful to ascertain a range of materials and thicknesses that can achieve a fixed transfer efficiency threshold, e.g. 5%, so it is easy determine if a scenario is applicable for IPT. Modelling could also be useful for analysing thermal effects and determining the upper bound for power transfer.

Finally, it would be interesting to investigate situations where IPT is uniquely applicable, i.e. scenarios where acoustic power transfer is not possible such as multi-layer walls that include air filled cavities.

References

[1] P. Lorrain, D. R. Corson, and F. Lorrain, *Electromagnetic fields and waves : including electric circuits*, 3rd ed. New York, N.Y.: Freeman, 1988. [Cited on pp. 7, 10, 12].

[2] J. B. Marion and M. A. Heald, *Classical electromagnetic radiation*, 2nd ed. New York ; London: Academic Press, 1980. [Cited on p. 8].

[3] S. V. Marshall and G. G. Skitek, *Electromagnetic concepts and applications*, 3rd ed. Prentice Hall, 1990. [Cited on p. 8].

[4] F. C. Moon, *Magneto-solid mechanics.* New York ; Chichester: Wiley, 1984. [Cited on pp. 11, 12, 35].

[5] S. Mitchell and J. Welsh, "The influence of complex permeability on the broadband frequency response of a power transformer," *Power Delivery, IEEE Transactions on*, vol. 25, no. 2, pp. 803–813, Apr. 2010. [Cited on p. 12].

[6] J. Heyman, "NDE in aerospace-requirements for science, sensors and sense," *Ultrasonics, Ferroelectrics and Frequency Control, IEEE Transactions on*, vol. 36, no. 6, pp. 581–586, Nov. 1989. [Cited on p. 13].

[7] L. Goglio and M. Rossetto, "Ultrasonic testing of adhesive bonds of thin metal sheets," *NDT & E International*, vol. 32, no. 6, pp. 323–331, 1999. [Cited on p. 13].

[8] R. Ditchburn, S. Burke, and C. Scala, "NDT of welds: state of the art," *NDT & E International*, vol. 29, no. 2, pp. 111–117, 1996. [Cited on p. 13].

[9] T. Kundu, *Advanced ultrasonic methods for material and structure inspection.* London ; Newport Beach, CA: ISTE, 2006. [Cited on p. 14].

[10] R.L. and Smith, "The effect of grain size distribution on the frequency dependence of the ultrasonic attenuation in polycrystalline materials," *Ultrasonics*, vol. 20, no. 5, pp. 211 – 214, 1982. [Cited on p. 15].

[11] P. Palanichamy, M. Vasudevan, T. Jayakumar, S. Venugopal, and B. Raj, "Ultrasonic velocity measurements for characterizing the annealing behaviour of cold worked austenitic stainless steel," *NDT & E International*, vol. 33, no. 4, pp. 253–259, 2000. [Cited on p. 15].

[12] J. A. Kleppe, *Engineering applications of acoustics*. Artech House, 1989. [Cited on p. 16].

[13] J. D. Turner and A. J. Pretlove, *Acoustics for engineers*. Macmillan Education, 1991. [Cited on p. 16].

[14] M. Stojanovic, "Recent advances in high-speed underwater acoustic communications," *Oceanic Engineering, IEEE Journal of*, vol. 21, no. 2, pp. 125–136, Apr. 1996. [Cited on p. 16].

[15] R. Primerano, K. Wanuga, J. Dorn, M. Kam, and K. Dandekar, "Echo-cancellation for ultrasonic data transmission through a metal channel," in *Information Sciences and Systems, 2007. CISS '07. 41st Annual Conference on*, March 2007, pp. 841–845. [Cited on pp. 17, 27, 54, 85].

[16] W.-H. Sheen and G. Stuber, "MLSE equalization and decoding for multipath-fading channels," *Communications, IEEE Transactions on*, vol. 39, no. 10, pp. 1455–1464, Oct. 1991. [Cited on p. 18].

[17] A. Safari and E. K. Akdoğan, *Piezoelectric and acoustic materials for transducer applications*. New York ; London: Springer, 2008. [Cited on p. 19].

[18] R. Halmshaw, *Non-destructive testing*, 2nd ed. Edward Arnold, 1991. [Cited on p. 20].

[19] S. J. Davies, C. Edwards, G. S. Taylor, and S. B. Palmer, "Laser-generated ultrasound: its properties, mechanisms and multifarious applications," *Journal of Physics D: Applied Physics*, vol. 26, no. 3, p. 329, 1993. [Cited on p. 20].

[20] B. Dutton, S. Boonsang, and R. Dewhurst, "A new magnetic configuration for a small in-plane electromagnetic acoustic transducer applied to laser-ultrasound measurements: Modelling and validation," *Sensors and Actuators A: Physical*, vol. 125, no. 2, pp. 249–259, 2006. [Cited on p. 22].

[21] E. Fraizier, M.-H. Nadal, and R. Oltra, "Noncontact determination of the elastic moduli of β-Sn up and through the melting point," *Journal of Applied Physics*, vol. 93, no. 1, pp. 649–654, Jan. 2003. [Cited on p. 22].

[22] I. Baillie, P. Griffith, X. Jian, and S. Dixon, "Implementing an ultrasonic inspection system to find surface and internal defects in hot, moving steel using EMATs," vol. 49, no. 2, Feb. 2007, pp. 87–92. [Cited on p. 22].

[23] P. R. Murray and R. J. Dewhurst, "Application of a laser/EMAT system for using shear and LS mode converted waves," *Ultrasonics*, vol. 40, no. 1-8, pp. 771–776, 2002. [Cited on p. 22].

[24] H. Ogi, M. Hirao, and T. Honda, "Ultrasonic attenuation and grain-size evaluation using electromagnetic acoustic resonance," *The Journal of the Acoustical Society of America*, vol. 98, no. 1, pp. 458–464, 1995. [Cited on p. 22].

[25] M. da Cunha and J. Jordan, "Improved longitudinal EMAT transducer for elastic constant extraction," in *Frequency Control Symposium and Exposition, 2005. Proceedings of the 2005 IEEE International*, Aug. 2005, pp. 426–432. [Cited on p. 22].

[26] P. Wilcox, M. Lowe, and P. Cawley, "Omnidirectional guided wave inspection of large metallic plate structures using an EMAT array," *Ultrasonics, Ferroelectrics and Frequency Control, IEEE Transactions on*, vol. 52, no. 4, pp. 653–665, Apr. 2005. [Cited on p. 22].

[27] X. Jian, S. Dixon, I. Baillie, R. S. Edwards, J. Morrison, and Y. Fan, "Shear wave generation using a spiral electromagnetic acoustic transducer," *Applied Physics Letters*, vol. 89, no. 24, Dec. 2006. [Cited on p. 22].

[28] M. Hirao and H. Ogi, *EMATs for Science and Industry.* Kluwer Academic, Boston, 2003. [Cited on pp. 22, 32, 33, 34, 36, 37, 38, 39, 40, 41].

[29] H. Ogi, M. Hirao, and T. Ohtani, "Flaw detection by line-focusing electromagnetic acoustic transducers," vol. 1, Oct. 1997, pp. 653–656. [Cited on p. 23].

[30] Y. Hu, X. Zhang, J. Yang, and Q. Jiang, "Transmission of electric energy through an elastic wall," vol. 1, 2001, pp. 567–570. [Cited on p. 24].

[31] ——, "Transmitting electric energy through a metal wall by acoustic waves using piezoelectric transducers," *Ultrasonics, Ferroelectrics and Frequency Control, IEEE Transactions on*, vol. 50, no. 7, pp. 773–781, July 2003. [Cited on pp. 24, 26].

[32] S. Sherrit, B. Doty, M. Badescu, X. Bao, Y. Bar-Cohen, J. Aldrich, and Z. Chang, "Studies of acoustic-electric feed-throughs for power transmission through structures." 2006. [Cited on pp. 24, 131].

[33] X. Bao, B. J. Doty, S. Sherrit, M. Badescu, Y. Bar-Cohen, J. Aldrich, and Z. Chang, "Wireless piezoelectric acoustic-electric power feedthru," vol. 6529, no. 1. SPIE, 2007, p. 652940. [Cited on p. 24].

[34] S. Sherrit, X. Bao, M. Badescu, J. Aldrich, Y. Bar-Cohen, W. Biederman, and Z. Chang, "1kW power transmission using wireless acoustic-electric feedthrough (WAEF)," vol. 323, 2008. [Cited on p. 25].

[35] D. Shoudy, G. Saulnier, H. Scarton, P. Das, S. Roa-Prada, J. Ashdown, and A. Gavens, "P3f-5 an ultrasonic through-wall communication system with power harvesting," in *Ultrasonics Symposium, 2007. IEEE*, Oct. 2007, pp. 1848–1853. [Cited on pp. 25, 26, 131].

[36] H. Hu, Y. Hu, C. Chen, and J. Wang, "A system of two piezoelectric transducers and a storage circuit for wireless energy transmission through a thin metal wall," *Ultrasonics, Ferroelectrics and Frequency Control, IEEE Transactions on*, vol. 55, no. 10, pp. 2312–2319, Oct. 2008. [Cited on p. 25].

[37] Z. Yang, S. Guo, and J. Yang, "Transmitting electric energy through a closed elastic wall by acoustic waves and piezoelectric transducers," *Ultrasonics, Ferroelectrics and Frequency Control, IEEE Transactions on*, vol. 55, no. 6, pp. 1380–1386, June 2008. [Cited on p. 25].

[38] Z. Yang, J. Yang, and Y. Hu, "Energy trapping in power transmission through an elastic plate by finite piezoelectric transducers," *Ultrasonics, Ferroelectrics and Frequency Control, IEEE Transactions on*, vol. 55, no. 11, pp. 2493–2501, Nov. 2008. [Cited on p. 25].

[39] ——, "Nonlinear behavior of electric power transmission through an elastic wall by acoustic waves and piezoelectric transducers," *Ultrasonics, Ferroelectrics and Frequency Control, IEEE Transactions on*, vol. 55, no. 11, pp. 2527–2531, Nov. 2008. [Cited on p. 25].

[40] S. Moss, P. McMahon, M. Konak, C. Phoumsavanh, N. Rajic, S. Galea, and I. Powlesland, "Modelling and experimental validation of an acoustic electric feedthrough," *DSTO Research Report 0338*, 2008. [Cited on p. 26].

[41] S. Moss, M. Konak, C. Phoumsavanh, K. Tsoi, and I. Powlesland, "Acoustic electric feedthrough demonstrator Mk-I," *DSTO Technical Report 2296*, 2009. [Cited on p. 26].

[42] S. Moss, C. Phoumsavanh, M. Konak, K. Tsoi, N. Rajic, S. Galea, I. Powlesland, and P. McMahon, "Design of the acoustic electric feedthrough demonstrator Mk-II," *Materials Forum*, vol. 33, pp. 187–200, 2009. [Cited on p. 26].

[43] S. Moss, S. J., M. Konak, and I. Powlesland, "Footprint reduction for the acoustic electric feedthrough technique," *DSTO Technical Report 2395*, 2010. [Cited on p. 26].

[44] T. Murphy, "Ultrasonic digital communication system for a steel wall multipath channel: Methods and results," *M.S. Thesis, Rensselaer Polytechnic Institute, Troy, NY*, 2005. [Cited on p. 26].

[45] G. J. Saulnier, H. A. Scarton, A. J. Gavens, D. A. Shoudy, T. L. Murphy, M. Wetzel, S. Bard, S. Roa-Prada, and P. Das, "Through-wall communication of low-rate digital data using ultrasound," in *Ultrasonics Symposium, 2006. IEEE*, Oct. 2006, pp. 1385–1389. [Cited on p. 26].

[46] M. Kluge, T. Becker, J. Schalk, and T. Otterpohl, "Remote acoustic powering and data transmission for sensors inside of conductive envelopes," in *Sensors, 2008 IEEE*, Oct. 2008, pp. 41–44. [Cited on p. 26].

[47] R. Primerano, M. Kam, and K. Dandekar, "High bit rate ultrasonic communication through metal channels," in *Information Sciences and Systems, 2009. CISS 2009. 43rd Annual Conference on*, March 2009, pp. 902–906. [Cited on pp. 27, 85].

[48] J. Bagshaw and L. Kent, "Patent (wo/2008/075092) data transfer," Nov. 2007. [Cited on p. 28].

[49] J. Sallan, J. Villa, A. Llombart, and J. Sanz, "Optimal design of ICPT systems applied to electric vehicle battery charge," *Industrial Electronics, IEEE Transactions on*, vol. 56, no. 6, pp. 2140–2149, June 2009. [Cited on pp. 28, 115].

[50] C. Jaskolski, E. Berkenpas, and G. Wilhelm, "Patent (wo/2008/039676) magnetic communication through metal barriers," Nov. 2007. [Cited on p. 29].

[51] X. Jian, S. Dixon, K. Quirk, and K. Grattan, "Electromagnetic acoustic transducers for in- and out-of plane ultrasonic wave detection," *Sensors and Actuators A: Physical*, vol. 148, no. 1, pp. 51–56, 2008. [Cited on p. 32].

[52] K. S. Ho, T. H. Gan, D. R. Billson, and D. A. Hutchins, "Application of pulse compression signal processing techniques to electromagnetic acoustic transducers for noncontact thickness measurements and imaging," *Review of Scientific Instruments*, vol. 76, no. 5, May 2005. [Cited on p. 32].

[53] H. Ogi, "Field dependence of coupling efficiency between electromagnetic field and ultrasonic bulk waves," *Journal of Applied Physics*, vol. 82, no. 8, pp. 3940–3949, Oct. 1997. [Cited on pp. 32, 33].

[54] R. Thompson, "A model for the electromagnetic generation of ultrasonic guided waves in ferromagnetic metal polycrystals," *Sonics and Ultrasonics, IEEE Transactions on*, vol. 25, no. 1, pp. 7–15, Jan. 1978. [Cited on pp. 32, 33].

[55] K. Kawashima, "Theory and numerical calculation of the acoustic field produced in metal by an electromagnetic ultrasonic transducer," *The Journal of the Acoustical Society of America*, vol. 60, no. 5, pp. 1089–1099, 1976. [Cited on p. 32].

[56] R. Ribichini, F. Cegla, P. Nagy, and P. Cawley, "Quantitative modeling of the transduction of electromagnetic acoustic transducers operating on ferromagnetic media," *Ultrasonics, Ferroelectrics and Frequency Control, IEEE Transactions on*, vol. 57, no. 12, pp. 2808–2817, December 2010. [Cited on pp. 36, 38].

[57] J. M. D. Coey, "Permanent magnetism," *Solid State Communications*, vol. 102, no. 2-3, pp. 101–105, 1997. [Cited on p. 42].

[58] J. Liu and M. Walmer, "Thermal stability and performance data for smco 2:17 high-temperature magnets on ppm focusing structures," *Electron Devices, IEEE Transactions on*, vol. 52, no. 5, pp. 899 – 902, may 2005. [Cited on p. 42].

[59] M. Theodoridis and S. Mollov, "Robust MOSFET driver for RF, class-D inverters," *Industrial Electronics, IEEE Transactions on*, vol. 55, no. 2, pp. 731–740, Feb. 2008. [Cited on p. 45].

[60] X. Jian, S. Dixon, R. Edwards, and J. Morrison, "Coupling mechanism of an EMAT," *Ultrasonics*, vol. 44, no. Supplement 1, pp. e653–e656, 2006, proceedings of Ultrasonics International (UI'05) and World Congress on Ultrasonics (WCU). [Cited on p. 48].

[61] D. T. Blackstock, *Fundamentals of physical acoustics*. New York: Wiley, 2000. [Cited on p. 54].

[62] D. O. E. Thompson and D. E. E. Chimenti, *Review of progress in quantitative nondestructive evaluation vol 16*. Plenum Press, 1997, Iowa State University. Center for NDE. [Cited on p. 56].

[63] K. Nowacki and W. Kasprzyk, "The sound velocity in an alloy steel at high-temperature conditions," *International Journal of Thermophysics*, vol. 31, no. 1, pp. 103–112, 2010. [Cited on pp. 57, 88].

[64] E. Drescher-Krasicka and J. R. Willis, "Mapping stress with ultrasound," *Nature*, vol. 384, no. 6604, pp. 52–55, 1996, 10.1038/384052a0. [Cited on p. 57].

[65] M. Landa and J. Plesek, "Contrast enhancement of ultrasonic imaging of internal stresses in materials," *Ultrasonics*, vol. 40, no. 1-8, pp. 531–535, 2002. [Cited on p. 57].

[66] G. Howe, O. Hinton, A. Adams, and A. Holt, "Acoustic burst transmission of high rate data through shallow underwater channels," *Electronics Letters*, vol. 28, no. 5, pp. 449–451, 1992. [Cited on p. 57].

[67] B. Sharif, O. Hinton, and A. Adams, "M-ary PSK burst mode transmission in multipath channels," *Electronics Letters*, vol. 31, no. 16, pp. 1326–1328, Aug. 1995. [Cited on p. 57].

[68] K. Nikolaidis and M. Sibley, "Investigation of an optical multiple PPM link over a highly dispersive optical channel," *Optoelectronics, IET*, vol. 1, no. 3, pp. 113–119, Jun. 2007. [Cited on p. 59].

[69] D.-S. Shiu and J. Kahn, "Differential pulse-position modulation for power-efficient optical communication," *Communications, IEEE Transactions on*, vol. 47, no. 8, pp. 1201–1210, Aug. 1999. [Cited on pp. 59, 60].

[70] D.-S. Yoo, W. Stark, K.-P. Yar, and S.-J. Oh, "Coding and modulation for short packet transmission," *Vehicular Technology, IEEE Transactions on*, vol. 59, no. 4, pp. 2104–2109, May 2010. [Cited on p. 67].

[71] "Ultrasonic transducers technical notes," Olympus, 2006. [Cited on p. 68].

[72] "Pic18f2525/2620/4525/4620 data sheet," Microchip Technology Inc., 2004. [Cited on p. 69].

[73] "Pixie DS481-17 data sheet," FlexiPanel Ltd, 2008. [Cited on p. 69].

[74] "IEEE Std 802.15.4-2006, IEEE recommended practice for information technology-telecommunications and information exchange between systems-local and metropolitan area networks-specific requirements-part 15.4: Wireless medium access control (MAC) and physical layer (PHY) specifications for low-rate wireless personal area networks (WPANs)," 2006. [Cited on p. 72].

[75] S. Singh and J. Cooper, "Bipolar integrated circuits in 4H-SiC," *Electron Devices, IEEE Transactions on*, vol. 58, no. 4, pp. 1084–1090, April 2011. [Cited on p. 79].

[76] C. Shannon, "Communication in the presence of noise," *Proceedings of the IEEE*, vol. 86, no. 2, pp. 447–457, Feb. 1998. [Cited on p. 80].

[77] J. G. Proakis, *Digital communications*, 5th ed. New York: McGraw-Hill Higher Education ; London : McGraw-Hill [distributor], 2008. [Cited on pp. 81, 85, 87, 89, 90].

[78] K. Zeger and A. Gersho, "Pseudo-gray coding," *Communications, IEEE Transactions on*, vol. 38, no. 12, pp. 2147–2158, Dec. 1990. [Cited on p. 81].

[79] T. Pollet, M. Van Bladel, and M. Moeneclaey, "BER sensitivity of OFDM systems to carrier frequency offset and Wiener phase noise," *Communications, IEEE Transactions on*, vol. 43, no. 234, pp. 191–193, Feb. 1995. [Cited on p. 83].

[80] T. Schmidl and D. Cox, "Robust frequency and timing synchronization for OFDM," *Communications, IEEE Transactions on*, vol. 45, no. 12, pp. 1613–1621, Dec. 1997. [Cited on p. 83].

[81] X. Li and J. Cimini, L.J., "Effects of clipping and filtering on the performance of OFDM," *Communications Letters, IEEE*, vol. 2, no. 5, pp. 131–133, May 1998. [Cited on p. 83].

[82] J. Armstrong, "Analysis of new and existing methods of reducing intercarrier interference due to carrier frequency offset in OFDM," *Communications, IEEE Transactions on*, vol. 47, no. 3, pp. 365–369, Mar. 1999. [Cited on p. 83].

[83] X. Cai and G. Giannakis, "Bounding performance and suppressing intercarrier interference in wireless mobile OFDM," *Communications, IEEE Transactions on*, vol. 51, no. 12, pp. 2047–2056, Dec. 2003. [Cited on pp. 83, 84].

[84] J. van de Beek, M. Sandell, and P. Borjesson, "ML estimation of time and frequency offset in OFDM systems," *Signal Processing, IEEE Transactions on*, vol. 45, no. 7, pp. 1800–1805, July 1997. [Cited on p. 83].

[85] N. Al-Dhahir, "Single-carrier frequency-domain equalization for space-time block-coded transmissions over frequency-selective fading channels," *Communications Letters, IEEE*, vol. 5, no. 7, pp. 304–306, July 2001. [Cited on p. 83].

[86] D. Falconer, S. Ariyavisitakul, A. Benyamin-Seeyar, and B. Eidson, "Frequency domain equalization for single-carrier broadband wireless systems," *Communications Magazine, IEEE*, vol. 40, no. 4, pp. 58–66, Apr. 2002. [Cited on p. 84].

[87] M. Luise and R. Reggiannini, "Carrier frequency acquisition and tracking for OFDM systems," *Communications, IEEE Transactions on*, vol. 44, no. 11, pp. 1590–1598, Nov. 1996. [Cited on p. 84].

[88] S. Qureshi, "Adaptive equalization," *Proceedings of the IEEE*, vol. 73, no. 9, pp. 1349–1387, Sept. 1985. [Cited on pp. 85, 87, 90, 101].

[89] S. S. Haykin, *Adaptive filter theory*, 4th ed. Upper Saddle River, N.J.: Prentice-Hall ; [Great Britain] : Pearson Education International, 2002. [Cited on pp. 85, 89, 90].

[90] M. Stojanovic, J. Catipovic, and J. Proakis, "Phase-coherent digital communications for underwater acoustic channels," *Oceanic Engineering, IEEE Journal of*, vol. 19, no. 1, pp. 100–111, Jan 1994. [Cited on p. 87].

[91] J. Proakis, "Adaptive equalization techniques for acoustic telemetry channels," *Oceanic Engineering, IEEE Journal of*, vol. 16, no. 1, pp. 21–31, Jan. 1991. [Cited on p. 87].

[92] K. Pahlavan, S. Howard, and T. Sexton, "Decision feedback equalization of the indoor radio channel," *Communications, IEEE Transactions on*, vol. 41, no. 1, pp. 164–170, Jan. 1993. [Cited on p. 87].

[93] M. Reuter, J. Allen, J. Zeidler, and R. North, "Mitigating error propagation effects in a decision feedback equalizer," *Communications, IEEE Transactions on*, vol. 49, no. 11, pp. 2028–2041, Nov. 2001. [Cited on p. 88].

[94] A. H. Sayed, *Fundamentals of adaptive filtering*. [Great Britain]: IEEE Press, 2003. [Cited on p. 90].

[95] Y. Zakharov, G. White, and J. Liu, "Low-complexity rls algorithms using dichotomous coordinate descent iterations," *Signal Processing, IEEE Transactions on*, vol. 56, no. 7, pp. 3150–3161, July 2008. [Cited on p. 91].

[96] V. Bhargava and M. Avni, "Net coding gain of some rate 1/2 block codes," *Communications, Radar and Signal Processing, IEE Proceedings F*, vol. 130, no. 4, pp. 325–330, June 1983. [Cited on p. 92].

[97] M. Tuchler and A. Singer, "Turbo equalization: An overview," *Information Theory, IEEE Transactions on*, vol. 57, no. 2, pp. 920–952, Feb. 2011. [Cited on p. 92].

[98] T. Mizuochi, "Recent progress in forward error correction and its interplay with transmission impairments," *Selected Topics in Quantum Electronics, IEEE Journal of*, vol. 12, no. 4, pp. 544–554, July-Aug. 2006. [Cited on p. 92].

[99] T. K. Moon, *Error Correction Coding : Mathematical Methods and Algorithms*. John Wiley & Sons Inc, 2005. [Cited on p. 107].

[100] D. de Villiers, S. Kaplan, and R. Wilkinson, "Energy harvesting for a condition monitoring mote," in *Industrial Electronics, 2008. IECON 2008. 34th Annual Conference of IEEE*, Nov. 2008, pp. 2161–2166. [Cited on p. 114].

[101] Z. Fan, R. Gao, and D. Kazmer, "Self-energized acoustic wireless sensor for pressure-temperature measurement in injection molding cavity," in *Sensors, 2009 IEEE*, Oct. 2009, pp. 65–68. [Cited on p. 114].

[102] J. P. Thomas, M. A. Qidwai, and J. C. Kellogg, "Energy scavenging for small-scale unmanned systems," *Journal of Power Sources*, vol. 159, no. 2, pp. 1494–1509, 2006. [Cited on p. 114].

[103] M. Kissin, J. Boys, and G. Covic, "Interphase mutual inductance in polyphase inductive power transfer systems," *Industrial Electronics, IEEE Transactions on*, vol. 56, no. 7, pp. 2393–2400, July 2009. [Cited on p. 115].

[104] N. Keeling, G. Covic, and J. Boys, "A unity-power-factor IPT pickup for high-power applications," *Industrial Electronics, IEEE Transactions on*, vol. 57, no. 2, pp. 744–751, Feb. 2010. [Cited on p. 115].

[105] E. Waffenschmidt and T. Staring, "Limitation of inductive power transfer for consumer applications," in *Power Electronics and Applications, 2009. EPE '09. 13th European Conference on*, Sept. 2009, pp. 1–10. [Cited on pp. 115, 116].

[106] J. Casanova, Z. N. Low, and J. Lin, "A loosely coupled planar wireless power system for multiple receivers," *Industrial Electronics, IEEE Transactions on*, vol. 56, no. 8, pp. 3060–3068, Aug. 2009. [Cited on p. 115].

[107] Z. N. Low, R. Chinga, R. Tseng, and J. Lin, "Design and test of a high-power high-efficiency loosely coupled planar wireless power transfer system," *Industrial Electronics, IEEE Transactions on*, vol. 56, no. 5, pp. 1801–1812, May 2009. [Cited on p. 115].

[108] U.-M. Jow and M. Ghovanloo, "Design and optimization of printed spiral coils for efficient transcutaneous inductive power transmission," *Biomedical Circuits and Systems, IEEE Transactions on*, vol. 1, no. 3, pp. 193–202, Sept. 2007. [Cited on p. 115].

[109] G. Kendir, W. Liu, G. Wang, M. Sivaprakasam, R. Bashirullah, M. Humayun, and J. Weiland, "An optimal design methodology for inductive power link with class-E amplifier," *Circuits and Systems I: Regular Papers, IEEE Transactions on*, vol. 52, no. 5, pp. 857–866, May 2005. [Cited on p. 115].

[110] X. Liu, W. Ng, C. Lee, and S. Hui, "Optimal operation of contactless transformers with resonance in secondary circuits," in *Applied Power Electronics Conference and Exposition, 2008. APEC 2008. Twenty-Third Annual IEEE*, Feb. 2008, pp. 645–650. [Cited on p. 116].

[111] C.-S. Wang, G. Covic, and O. Stielau, "Power transfer capability and bifurcation phenomena of loosely coupled inductive power transfer systems," *Industrial Electronics, IEEE Transactions on*, vol. 51, no. 1, pp. 148–157, Feb. 2004. [Cited on p. 116].

[112] J. ichi Tani, M. Mayuzumi, and N. Hara, "Stress corrosion cracking of stainless-steel canister for concrete cask storage of spent fuel," *Journal of Nuclear Materials*, vol. 379, no. 1-3, pp. 42–47, 2008. [Cited on p. 118].

[113] A. Kosaki, "Evaluation method of corrosion lifetime of conventional stainless steel canister under oceanic air environment," *Nuclear Engineering and Design*, vol. 238, no. 5, pp. 1233–1240, 2008. [Cited on p. 118].

[114] S. T. Lundmark and E. Hamdi, "Designs of claw-pole motors for industrial applications," in *Power Electronics, Machines and Drives, 2006. The 3rd IET International Conference on*, Mar. 2006, pp. 111–115. [Cited on p. 121].

[115] B. Cranganu-Cretu, A. Kertesz, and J. Smajic, "Coupled electromagnetic-thermal effects of stray flux: Software solution for industrial applications," *Industrial Electronics, IEEE Transactions on*, vol. 57, no. 1, pp. 14–21, Jan. 2010. [Cited on p. 121].

[116] C. Breton, J. Bartolome, J. Benito, G. Tassinario, I. Flotats, C. Lu, and B. Chalmers, "Influence of machine symmetry on reduction of cogging torque in permanent-magnet brushless motors," *Magnetics, IEEE Transactions on*, vol. 36, no. 5, pp. 3819–3823, Sep 2000. [Cited on p. 121].

[117] D. Torregrossa, A. Khoobroo, B. Fahimi, F. Peyraut, and A. Miraoui, "Prediction of acoustic noise and torque pulsation in PM synchronous machines with rotor static eccentricity and partial demagnetization using field reconstruction method," *Industrial Electronics, IEEE Transactions on*, vol. PP, no. 99, p. 1, 2011. [Cited on p. 121].

[118] C.-J. Chen, T.-H. Chu, C.-L. Lin, and Z.-C. Jou, "A study of loosely coupled coils for wireless power transfer," *Circuits and Systems II: Express Briefs, IEEE Transactions on*, vol. 57, no. 7, pp. 536–540, July 2010. [Cited on pp. 129, 130].

[119] J. G. Webster, *The measurement, instrumentation and sensors handbook*. CRC Press, 1999. [Cited on p. 131].